ABSTRACT

ENERGY DEPENDENCE AND SPECTROSCOPY
IN THE
$^{16}O(p,d)^{15}O$ AND $^{15}N(p,d)^{14}N$ REACTIONS

By James Lewis Snelgrove

A systematic study of the extraction of spectroscopic factors for the (p,d) reaction on light nuclei and the difficulties encountered in obtaining reasonable DWBA fits to the shapes of the angular distributions has been made. Deuteron spectra and angular distributions were obtained for the $^{16}O(p,d)^{15}O$ reaction over an angular range of 10° to 165° in the center-of-mass frame for 25.52, 31.82, 38.63, and 45.34 MeV incident protons using the variable energy proton beam of the Michigan State University sector focused cyclotron. Partial angular distributions were obtained for other proton energies between 21 and 36 MeV. The elastic scattering of protons from ^{16}O was measured over the same energy range and used to obtain proton optical model parameters. Deuteron optical model parameters for the $^{16}O(d,d)^{16}O$ reaction were obtained from the literature for use in the DWBA exit channel calculations.

DWBA calculations were performed using the Oak Ridge code JULIE, and spectroscopic factors were extracted for the 0.0 MeV, $1/2^-$ and 6.18 MeV, $3/2^-$ levels of ^{15}O. Unadjusted optical model parameters were used with a 3 F cutoff to obtain some agreement between the shapes of the experimental and theoretical angular distributions. The absolute values of the extracted spectroscopic factors were found to depend strongly on the value of the neutron bound state well radius used in the DWBA calculations. The best absolute values of the spectroscopic factors were obtained when the neutron bound state well radius was set equal to the proton real well radius, whereas relative spectroscopic factors were found to depend much less strongly on this parameter. The energy dependence of the differential cross section was reproduced by the DWBA calculations for deuterons in the exit channel having a center-of-mass energy greater than 22 MeV. The variable energy feature of the MSU cyclotron was used in a scheme to eliminate part of the Q-dependence from the relative spectroscopic factors. The lack of any improvement indicates that the problems with the DWBA calculations are probably not in the deuteron channel. At least 30% of the $1p_{3/2}$ strength appears to be missing from the 6.18 MeV, $3/2^-$ level, with approximately 12% of the missing strength appearing in the 9.60 MeV and

10.46 MeV levels. Small 2s-1d admixtures and a possible $1g_{7/2}$ admixture were observed in the ground state of ^{16}O.

Energy spectra and angular distributions were obtained over an angular range of 10° to 145° in the center-of-mass frame for the $^{15}N(p,p)^{15}N$ and $^{15}N(p,d)^{14}N$ reactions at 39.84 MeV. Using the method determined by the $^{16}O(p,d)^{15}O$ work, spectroscopic factors were extracted for the levels in ^{14}N populated by $\ell_n=1$ pickup. These values were found to be in excellent agreement with intermediate coupling predictions. The 2^+, T=1 levels of ^{14}N at 9.17 and 10.43 MeV were found to be strongly mixed. The 13.72 MeV level of ^{14}N was unambiguously assigned $J^\pi=1^+$, T=1 on the basis of comparison with theoretical predictions, and a width of 210 ± 30 keV has been determined for this level. Angular distributions for all the ^{14}N levels populated in the $^{15}N(p,d)^{14}N$ reaction are shown.

ENERGY DEPENDENCE AND SPECTROSCOPY IN THE $^{16}O(p,d)^{15}O$ AND $^{15}N(p,d)^{14}N$ REACTIONS

By

James Lewis Snelgrove

A THESIS

Submitted to
Michigan State University
in partial fulfillment of the requirements
for the degree of

DOCTOR OF PHILOSOPHY

Department of Physics

1968

ACKNOWLEDGMENTS

My deepest appreciation goes to Dr. Edwin Kashy for the advice and counsel he has given me throughout my graduate study and particularly during the preparation of this thesis.

The assistance of Dr. Barry Preedom and Miss Thelma Arnette in the use of the optical model and DWBA codes was invaluable. I also acknowledge many helpful discussions with other members of the professional staff of the Michigan State University Cyclotron Laboratory.

I am grateful to Phillip Plauger and Craig Barrows for their assistance in data acquisition and to Bryan Horning for his help in analyzing the data.

To the members of the Cyclotron Laboratory technical staff go my thanks for their assistance in building and maintaining apparatus used in the experiments for this thesis and for their help in running the cyclotron itself.

I also acknowledge the financial support of the experimental program provided by the National Science Foundation and the personal financial support provided by a three-year National Aeronautics and Space Administration Traineeship and a one-year National Science Foundation Graduate Fellowship.

TABLE OF CONTENTS

LIST OF TABLES

LIST OF FIGURES

CHAPTER I

INTRODUCTION

For a number of years the (p,d) reaction has proven to be a popular and valuable tool in nuclear spectroscopy. The selective way in which the (p,d) reaction populates the levels of the residual nucleus provides information about these levels and about the ground state of the target nucleus, which can be compared to the predictions of various models used to describe certain properties of the nuclei. The direct reaction picture provides a correlation between the shape of the deuteron angular distribution and the angular momentum transferred to the picked-up neutron. This enables one to make parity (and sometimes, spin) assignments for the levels of the residual nucleus. The most widely used theory of direct reactions is the distorted-wave Born approximation (DWBA), and from comparisons of experimental and theoretical angular distributions one can also determine the overlap of the target wavefunction with the wavefunctions of the states in the residual nucleus. The overlap for a given state is related to the spectroscopic factor, an

experimental quantity extracted from comparison of the data to theoretical calculations. The meaningfulness of the spectroscopic factors, however, depends on the degree to which the DWBA calculation represents the actual reaction mechanism. The distorted waves in a DWBA calculation are assumed to be those which describe the elastic scattering of the proton and deuteron by the appropriate nuclear states, and are calculated from optical model potentials. In studies of (p,d) reactions on nuclei in the 1p and 2s-1d shells, difficulty has been encountered in obtaining reasonable agreement of the experimental and theoretical angular distribution shapes when optical potentials which best describe the elastic scattering are used in a standard DWBA calculation (no integration cutoffs, etc.). The theoretical shapes have been improved by somewhat artificial means (e.g., adjusting potentials or using cutoffs), but then one must question the accuracy of the spectroscopic factors extracted on the basis of such calculations.

The present work was undertaken first to study the extraction of (p,d) spectroscopic factors for light nuclei, then to apply this knowledge to the analysis of data from the $^{15}N(p,d)^{14}N$ reaction, which had not been previously studied. The target nucleus for the study of spectroscopic factors, ^{16}O, was chosen for several reasons. It is a

nominally "closed-shell" nucleus on which numerous theoretical studies have been done. One feels confident, then, in making certain predictions about the values of the spectroscopic factors which should be obtained. These predictions could be used as a guide in evaluating the results of a given DWBA calculation. Since, as will be shown, the $^{16}O(p,d)^{15}O$ peak cross sections show a strong energy dependence, it was possible to test the DWBA calculations over a wide ($\sim$20MeV) energy range. During the course of the study considerable spectroscopic information was obtained on the levels of ^{15}O and is presented in some detail. Similar studies have been made for the $^{40}Ca(d,p)^{41}Ca$ reaction (Le 64) and for the $^{16}O(d,^3He)^{15}O$ and $^{40}Ca(d,^3He)^{39}K$ reactions (Hi 67).

Although the ^{14}N levels have previously been studied extensively by means of other reactions, the selective nature of the (p,d) reaction made it possible to obtain much new spectroscopic information about this nucleus. The extracted spectroscopic factors are compared to those predicted by the 1p shell intermediate coupling calculations of Cohen and Kurath (Co 67), which had previously proven valid for lighter 1p shell nuclei (Ku 67).

CHAPTER II

NUCLEAR THEORY

II.A. Distorted-Wave Born Approximation

A direct reaction is defined as a reaction in which only one degree of freedom is excited in the target nucleus (Au 63). The (p,d) reaction is considered to be direct if the proton picks up a neutron from the ground state of the target nucleus in a simple one-step process. The most distinctive characteristic of the direct reaction process is a strong forward peaking of the angular distribution and its subsequent oscillation with increasing angle. Earliest attempts to describe the direct reaction (Bu 51) used the plane wave Born approximation, but recently the distorted-wave Born approximation (DWBA) has been used exclusively. Extensive discussions of the DWBA theory have been presented by Tobocman (To 61) and Satchler (Sa 64). The most salient features of the DWBA theory and the approximations employed in it are discussed in the following sections.

II.A.1. DWBA Expression for Differential Cross Section

The differential cross section for the reaction A(a,b)B is given (Sa 64) by

$$\frac{d\sigma}{d\Omega} = \frac{\mu_a \mu_b}{(2\pi\hbar^2)^2} \frac{k_b}{k_a} \frac{\sum_{M_a m_a M_b m_b} |T|^2}{(2J_A+1)(2s_a+1)} \qquad \text{(II.1)}$$

where the transition amplitude is

$$T = \mathcal{J} \int d\underline{r}_a \int d\underline{r}_b \chi_b^{(-)*}(\underline{k}_b, \underline{r}_b) \langle B,b|V|A,a\rangle \chi_a^{(+)}(\underline{k}_a, \underline{r}_a). \qquad \text{(II.2)}$$

Here $\mathcal{J}$ is the Jacobian of the transformation to the relative coordinates $\underline{r}_a$ (the displacement of a from A) and $\underline{r}_b$ (the displacement of b from B), and μ_a and μ_b are the reduced masses of a and b. The functions χ_a and χ_b are the distorted waves and are taken to be the elastic scattering waves which asymptotically describe the relative motion of the a,A and b,B pairs before and after the collision, respectively. The distorted waves are usually calculated from an optical potential of the form shown in Chapter IV.

The remaining factor in (II.2) is the matrix element of the interaction causing the inelastic event, taken between the internal states of the colliding pairs, and it contains all of the nuclear structure information. Thus, the inelastic event is treated as a perturbation to

the elastic scattering. The matrix element can be expanded into terms corresponding to the transfer to the nucleus of a definite angular momentum j, comprised of an orbital part ℓ and a spin part s. These can be defined by

$$\underline{j} = \underline{J}_B - \underline{J}_A, \quad \underline{S} = \underline{s}_b - \underline{s}_a, \quad \underline{\ell} = \underline{j} - \underline{s},$$

where s_a, s_b are the intrinsic spins of particles a,b; and J_A, J_B are the nuclear spins of A,B. The transition amplitude becomes

$$J\langle J_B M_B, s_b m_b | V | J_A M_A, s_a m_a \rangle = \sum_{\ell s j} i^{-\ell} G_{\ell s j m}(\underline{r}_b, \underline{r}_a)$$
$$\times (-)^{s_b - m_b} \langle J_A j M_A, M_B - M_A | J_B M_B \rangle \langle s_a s_b m_a, -m_b | s, m_a - m_b \rangle$$
$$\times \langle \ell s m, m_a - m_b | j, M_B - M_A \rangle. \qquad \text{(II.3)}$$

The term $G_{\ell s j m}(\underline{r}_b, \underline{r}_a)$ is called the radial form factor and contains all of the information about the radial part of the interaction. In general, it is convenient to separate $G_{\ell s j m}$ as a product of a spectroscopic coefficient and a form factor:

$$G_{\ell s j m}(\underline{r}_b, \underline{r}_a) = A_{\ell s j} f_{\ell s j m}(\underline{r}_b, \underline{r}_a), \qquad \text{(II.4)}$$

where $A_{\ell s j}$ contains such quantities as fractional parentage coefficients. For the case of the (p,d) reaction, these are the coefficients of the expansion of the ground state

wavefunction of the target nucleus in terms of the wavefunctions of the final states in the residual nucleus coupled to the wavefunction of a single neutron.

The evaluation of T (II.2) involves a six-dimensional numerical integration, which is quite difficult. A simplification usually used is the zero-range approximation, in which the outgoing particle b is emitted at the point at which the incoming particle is absorbed. This results in

$$f_{\ell sjm}(\underline{r}_b,\underline{r}_a) \simeq f_{\ell sj}(r_a) Y_\ell^{m^*}(\theta_a,\phi_a)\,\delta(\underline{r}_b - \frac{M_A}{M_B}\underline{r}_a), \qquad \text{(II.5)}$$

where $f_{\ell sj}(r_a)$ is the radial wavefunction of the picked-up neutron for the (p,d) reaction. It now contains all of the information of nuclear structure. Under the zero range approximation, (II.3) implies an allowed parity change of $(-)^\ell$ (Sa 64).

If only one value each of s and ℓ are allowed, as in the (p,d) reaction where s = 1/2 and ℓ is determined by the parity change, the value of the differential cross section becomes (Sa 64, Ba 62)

$$\frac{d\sigma}{d\Omega} = \frac{2s_b + 1}{2s_a + 1} \sum_{\ell sj} S_{\ell sj}\sigma_{\ell sj}(\theta) \text{ mb/sr.} \qquad \text{(II.6)}$$

Thus, with $s_a = 1/2$, $s_b = 1$, and s = 1/2, the differential cross section, since only one ℓ and j are allowed, is

$$\frac{d\sigma}{d\Omega} = \frac{3}{2} S_{\ell j} \sigma_{\ell j}(\theta), \qquad \text{(II.7)}$$

where $\sigma_{\ell j}(\theta)$ is the cross section computed by the Oak Ridge code JULIE (Ba 62, Ba 66). The effect of using zero range rather than an effective range can be approximately removed by multiplying $\sigma_{\ell j}(\theta)$ by a factor of 1.5 (Au 64). Thus, the final expression for the differential cross section is

$$\frac{d\sigma}{d\Omega} = 2.25 S \sigma_{DWBA}(\theta) \ \text{(mb/sr)} \qquad \text{(II.8)}$$

where the subscripts have been dropped.

II.A.2. Finite-Range and Non-Locality Corrections

The neglect of finite-range effects has been investigated by Austern et al. (Au 64) and proved to be most important in reactions which involve large momentum transfers. The inclusion of exact finite-range calculations is difficult, but the effects are approximated by the local energy approximation (Bu 64, Pe 64) as a correction factor which multiplies the zero-range radial form factor $f_{\ell s j}(r_a)$. The effect is to lessen the contribution of the nuclear interior. A further correction to the calculation can be made by the inclusion of non-locality in the optical potentials. This can also be calculated in the local

energy approximation, resulting in a further lessening of the contribution of the nuclear interior.

II.A.3. Extraction of Experimental Spectroscopic Factors

In the ideal case one would find that the calculated DWBA angular distribution would reproduce the shape of the experimental angular distribution and would, therefore, differ at each point by a constant factor, as shown in (II.8). The spectroscopic factor S would, then, be unambiguous. Although the DWBA and experimental angular distribution shapes are similar in many cases, the application of (II.8) at different points of the distribution will not give unique results. A method for the extraction of spectroscopic factors which has been successfully applied for ($\ell_n \neq 0$) (Ku 67, Ko 67a) is to use (II.8) at the characteristic forward peak of angular distribution. One might expect that the assumption of a direct reaction is more valid for forward angle scattering. On a semi-classical picture, the impact parameter for forward angle scattering is much larger than for backward angle scattering, so the incoming particle tends to interact less with the nucleus and thus is less likely to excite more than one degree of freedom. It is also thought (Au 63) that exchange terms, which were not included in the

transition amplitude, are unimportant at forward angles, but they might make noticeable contributions at the backward angles. Also, the fit of the DWBA calculations to the data at the forward angles, where most of the integrated cross section is contained, is usually best.

Thus, (II.8) has been applied to the forward peak of the $\ell_n \neq 0$ angular distributions to obtain the corresponding spectroscopic factors given in this work. The situation for the extraction of $\ell_n=0$ spectroscopic factors is not clear, since the characteristic forward maximum occurs at $\theta_{c.m.}=0°$. In these cases approximate spectroscopic factors might be obtained by matching the DWBA calculations and the experimental data at several forward angles. However, owing to the uncertainties involved in such a procedure, no attempt was made to extract $\ell_n=0$ spectroscopic factors on this basis.

II.B. Intermediate Coupling Model

The two models used extensively to describe phenomena involving the interaction of particles having both angular momentum and intrinsic spin are the jj-coupling model and the LS-coupling model. The jj-coupling model (the nuclear shell model) has been very successful in explaining many features observed in heavy nuclei (Ma 50). In this model the spin-orbit force causes the orbital angular momentum

$\underline{\ell}$ and the intrinsic $\underline{s}$ for each nucleon to couple to form a resultant angular momentum $\underline{j}$. Then, the $\underline{j}$'s of the individual nucleons interact to produce a characteristic set of energy levels. The resulting wavefunctions can be used to predict various nuclear properties. In the LS-coupling model, which has been widely applied in the study of atomic spectra, the spins of all the particles are coupled to form a resultant spin $\underline{S}$, and the orbital angular momenta are coupled to produce a resultant angular momentum $\underline{L}$. These are then coupled by the spin-orbit interaction to produce a total angular momentum $\underline{J}$. The energy level schemes predicted by the two models are different, but the total number of states which can be formed in each case are the same.

The success of the jj-coupling model for heavy nuclei has not been repeated for the light nuclei, particularly the 1p shell nuclei (Ku 52). The LS-coupling model has not had much success for these nuclei either (Fe 37). The concept of intermediate coupling, of which jj- and LS-coupling are the two extremes, had been applied to the theory of complex atomic spectra (Co 35) and was used by Inglis (In 53) in an attempt to explain the energy level sequences of the 1p shell nuclei.

Since the energy level sequence and spacing is expected to depend upon the interactions of the lp nucleons, the interaction between any two of the nucleons must be considered (this, of course, ignores the effects of many-body forces). The central interaction is generally considered to be a central interaction $V(r_{ij})$ multiplied by an exchange operator O_{ij} usually approximated (Ro 48) by

$$O_{ij} \simeq 0.8P + 0.2Q, \tag{II.9}$$

where P is the Majorana space-exchange operator and Q is the Bartlett spin-exchange operator. A simple form of the spin-orbit coupling operator

$$H' = \sum a\underline{\ell}\cdot\underline{s} \tag{II.10}$$

is usually assumed as a perturbation term in the Hamiltonian. In the early works (In 53) the parameter a was assumed to be constant for a given nucleon shell. The diagonalization of the unperturbed Hamiltonian, which gives the energies of the levels, results in integrals of the form

$$L = \int \Psi^*(r_i)\phi^*(r_j)V(r_{ij})\Psi(r_i)\phi(r_j)d\underline{r}_i d\underline{r}_j$$

and

$$K = \int \Psi^*(r_i)\phi^*(r_j)V(r_{ij})\phi(r_i)\psi(rj)d\underline{r}_i d\underline{r}_j. \tag{II.11}$$

The integral L is commonly called the ordinary, or direct, integral, and K is called the exchange integral. The energies calculated are a linear combination of L and K, so that the splitting of the degeneracy by the perturbation can be expressed in terms of the parameters a,K, and L.

It has been found that the ratio L/K depends only upon the range of the nuclear forces; the value L/K = 6.8 is reasonable for the 1p shell (Ku 56). The ratio a/K provides a measure of the relative spin-orbit and central energy contributions. In general, a/K ≃ 2 for the Li isotopes, whereas a/K ≃ 5 or 6 gives reasonable agreement for masses 13 and 14. This effect is primarily due to a (Ku 56). The large values of a/K imply a close correspondence between the intermediate coupling and jj-coupling pictures. The value of K itself is usually determined from the known energy spacings. Once the parameters have been fixed, wavefunctions can be calculated and used to predict experimentally observable phenomena, such as radiative transition widths (Ku 57).

The most extensive application of the intermediate coupling model to 1p shell nuclei has been made by Cohen and Kurath (Co 65, Co 67). From the available experimental data they derived single particle energies and an effective

interaction for the 1p shell. The effective interaction was then used in intermediate coupling calculations to determine wavefunctions for the levels. From these wavefunctions they extracted coefficients of fractional parentage (CFP), from which spectroscopic factors can be derived.

The theoretical ℓ_n=1 spectroscopic factors for the $^{15}N(p,d)^{14}N$ reaction were extracted from the CFPs calculated by Cohen and Kurath (Co 67). They are given by

$$S = n|\langle T'1/2M'_T 1/2|TM_T\rangle|^2 \sum_j CFP_j^2,$$

where n is the number of nucleons in the 1p shell of the target (n = 11 for ^{15}N), and $\langle|\rangle$ is a Clebsch-Gordan coefficient which accounts for the amount of strength going into the neutron pickup reaction as opposed to the proton pickup reaction. T,T' and M_T, M'_T are the isotopic spins and their projections for the target and residual state, respectively. The first 1/2 in the Clebsch-Gordan coefficient is the isotopic spin of a nucleon, and the second 1/2 is the isotopic spin projection of the neutron. The summation is over all values of j possible for a given energy level.

CHAPTER III

EXPERIMENTAL APPARATUS AND METHODS

III.A. Proton Beam Production and Handling

III.A.1. Cyclotron

The proton beams for these experiments were produced by the Michigan State University sector-focused cyclotron (Bl 66). Two methods of acceleration and extraction were used during the course of this study. In one, negative hydrogen ions were accelerated to extraction radius, then stripped of their two electrons by a 700 $\mu g/cm^2$ aluminum foil. The Lorentz force on the ions is thus reversed, and they are deflected out of the cyclotron. The second method entailed the acceleration of positively charged hydrogen ions (protons) to extraction radius where they were extracted using an electrostatic deflector and a magnetic channel. This latter method is preferred owing to the higher intensity and better beam quality, i.e., higher phase space density. However, when the voltage on the electrostatic deflector necessary to deflect protons of a given energy was higher than conditions of the day

allowed, or when modifications were being made on the deflector, the former method was used successfully.

III.A.2. Analysis System

The philosophy and construction of the beam transport system has been described previously (Ma 67). A schematic diagram is shown in Fig. III-1. Momentum analysis is accomplished by the 45° magnets M3 and M4. The resolution of the beam is determined by the widths of the apertures S1 and S3, while its divergence can be limited by the aperture S2. These apertures are remotely controlled and have been described previously (Be 68a). For equal widths of S1 and S3 the energy resolution of the transmitted beam is 1 part in 10^4 per 0.013 in. of opening. Typical apertures used in these experiments varied between 0.060 in. and 0.100 in., corresponding to energy resolutions of 5 to 8 parts in 10^4. The distance between S1 and S2 is approximately 44 in., so a typical width of S2 of 0.40 in. gives a beam divergence of ±9 mrad. The energy of the beam was determined from the values of decapot settings of the magnet power supplies reached by a well-defined cycling procedure. The energy reproducibility of this system is believed to be 1 part in 15000, if the central fields of M3 and M4 are reproduced as indicated by nuclear magnetic resonance fluxmeters (Sn 67).

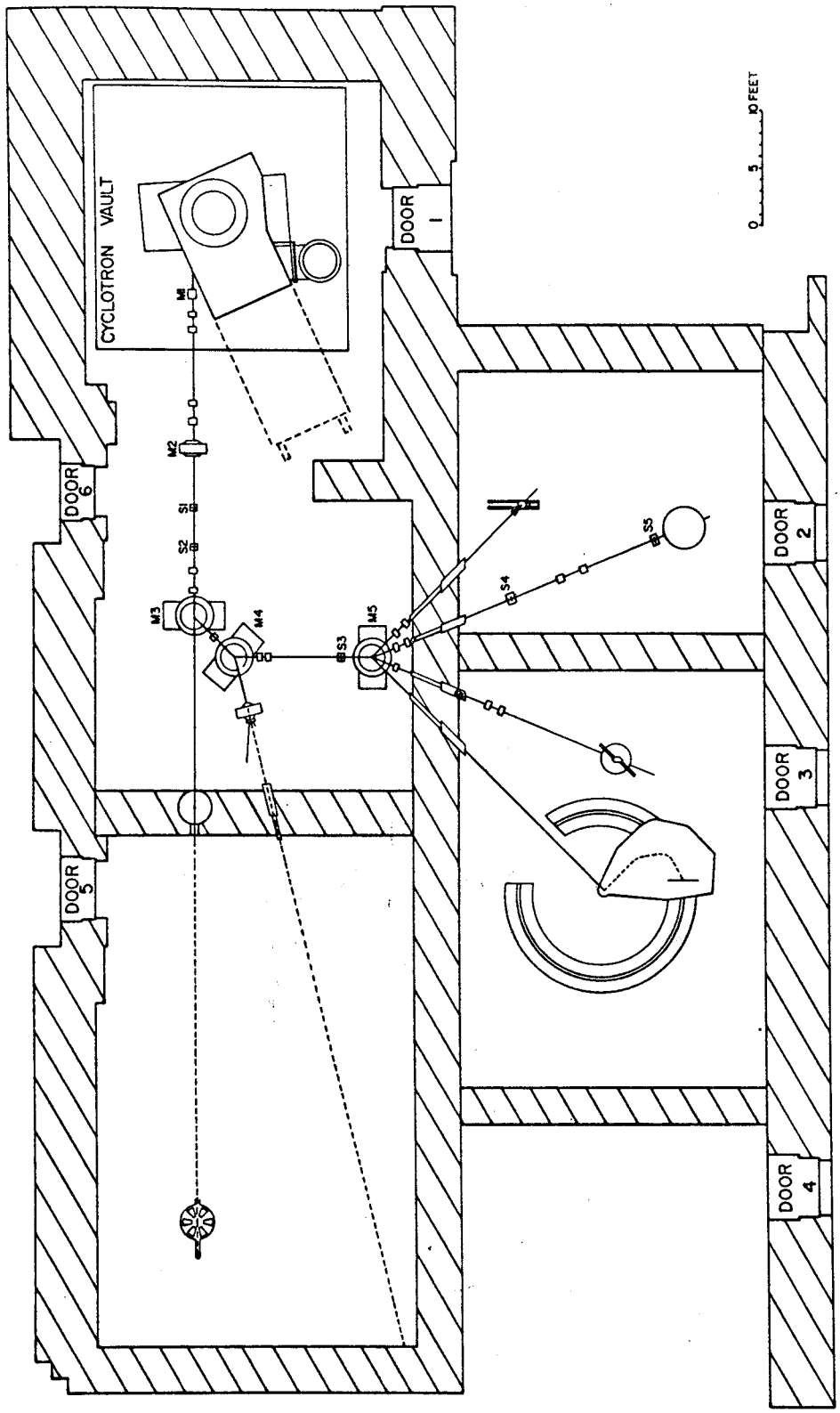

Figure III-1. Experimental area of the Michigan State University Cyclotron Laboratory.

III.A.3. Alignment of Beam to Scattering Chamber

A schematic diagram of the beamline leading to the scattering chamber is shown in Fig. III-2. After having been deflected through 22.5° by the switching magnet (M5), the beam was focused by a quadrupole doublet. A 0.375 in. square aperture was placed at the intermediate focus. A second aperture 0.40 in. wide and a third aperture 0.250 in. wide and 0.375 in. high were positioned immediately outside the scattering chamber and approximately 6 in. from the center of the chamber, respectively. A second quadrupole doublet focused the beam at the center of the chamber. The size and position of the beam spot on a 0.010 in. thick piece of Pilot B* plastic scintillator was viewed by closed-circuit television, and currents on the various apertures were monitored during the alignment. The excitation of M5 and the quadrupole doublets were adjusted to give minimum current readings on the apertures and the best possible beam spot on the scintillator. Beam spots were typically rectangular with a width of 0.100 in. and height of 0.150 in.

---

*Pilot Chemical, Watertown, Mass.

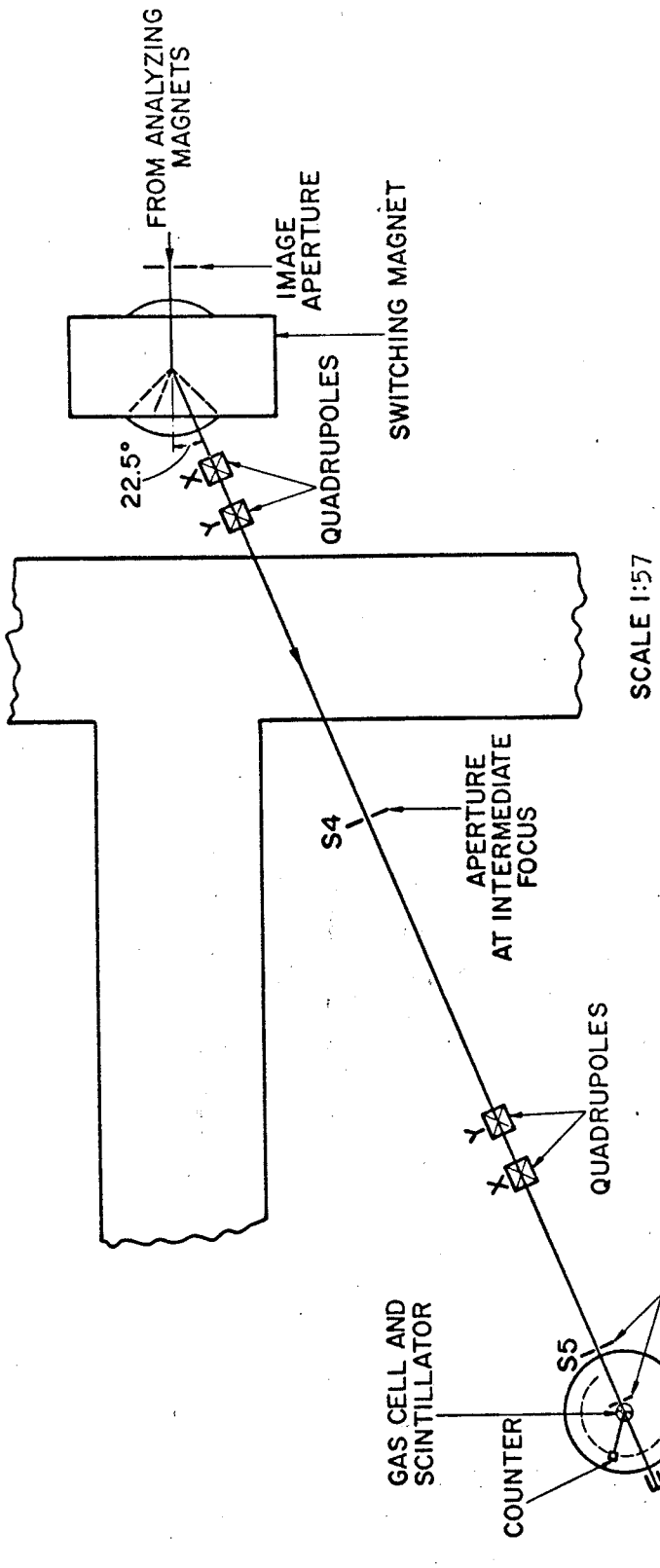

Figure III-2. Section of the beam system leading to the 36-in. scattering chamber, showing the apertures used for beam alignment.

III.A.4. Charge Integration

Protons passing through the target were collected by a Faraday cup located outside the rear wall of the chamber. The insulated cup is 2.88 in. in diameter and 11.5 in. deep. In previous studies (Ku 67) little change in the collected charge was detected when permanent magnets were placed near the entrance of the cup to prevent the escape of secondary electrons.

The beam current and integrated charge were measured using an Elcor model A310B current indicator and integrator. The accuracy of the instrument has been found to be within 1% using both internal and external calibration sources (Ku 67). The calibration of each scale was checked against the internal calibration source at the end of most experiments. These tests showed the calibration to be within 1.1%; the integrated charges were subsequently corrected for deviations in calibration.

III.B. Scattering Chamber Set-Up

III.B.1. Scattering Chamber

A 36 in. diameter scattering chamber was used in these experiments. The chamber contains a counter arm which can be remotely positioned over a useful angular range of ± 165°, the upper limit being determined by the geometry of the beam and counter collimators used in the experiment. The

digital readout has been calibrated against an internal protractor, and this calibration curve was used to correct the digital readout values. To eliminate errors due to backlash in the mechanism, care was taken to set all angles in a consistent manner. It is felt that these procedures led to a relative angular accuracy of better than ±0.2°. The chamber also contains a target post which can be remotely positioned in height and in angle. Ports are available in the side of the chamber through which electrical leads, etc., can be passed.

III.B.2. Targets

All data presented were taken using gas targets. For the ^{16}O experiments, natural oxygen gas, which has an isotopic abundance of ^{16}O of 99.76%, was used. An enriched gas consisting of 99% ^{15}N was used in the ^{15}N experiment. The gases were contained in gas cells during the experiments.

Two different cells were used, each having certain advantages and disadvantages. Most of the $^{16}O(p,d)^{15}O$ data was taken with a 5 in. diameter cell whose top and bottom plates were held apart by two struts placed 180° apart. The window of the cell was 0.0005 in. Kapton* clamped against an O-ring seal. Gas was introduced from outside

*E.I. DuPont de Nemours, Wilmington, Del.

the chamber until a pressure of 30 cm Hg, as measured by a mercury manometer, was attained. The pressure in the cell was continuously monitored by viewing the manometer with remote television. The temperature of the cell was assumed to remain at room temperature.

Certain problems and disadvantages were encountered while using this cell. The method used in sealing the window made replacement quite difficult: clamping a 0.0005 in. foil against an O-ring around a circular cell without causing a leak-producing wrinkle is extremely difficult. In fact, the cell was never completely tight. This method certainly was unacceptable for an expensive gas such as ^{15}N. Also, the volume of such a large cell is impractical for expensive gases. Finally, it was necessary to keep track of the relation of the supporting strut and counter positions in order that the counter would not inadvertantly be allowed to pass behind the strut.

All of these objections were removed by using a 3 in. diameter cell designed for the ^{15}N experiment. The cell (Fig. III-3) was machined from a solid piece of brass; the top and bottom were quite thick to reduce flexing, since there is support only on one side. The counters could be positioned from -40° to the limit of 165° previously mentioned without moving the cell. The window was 0.0005 in.

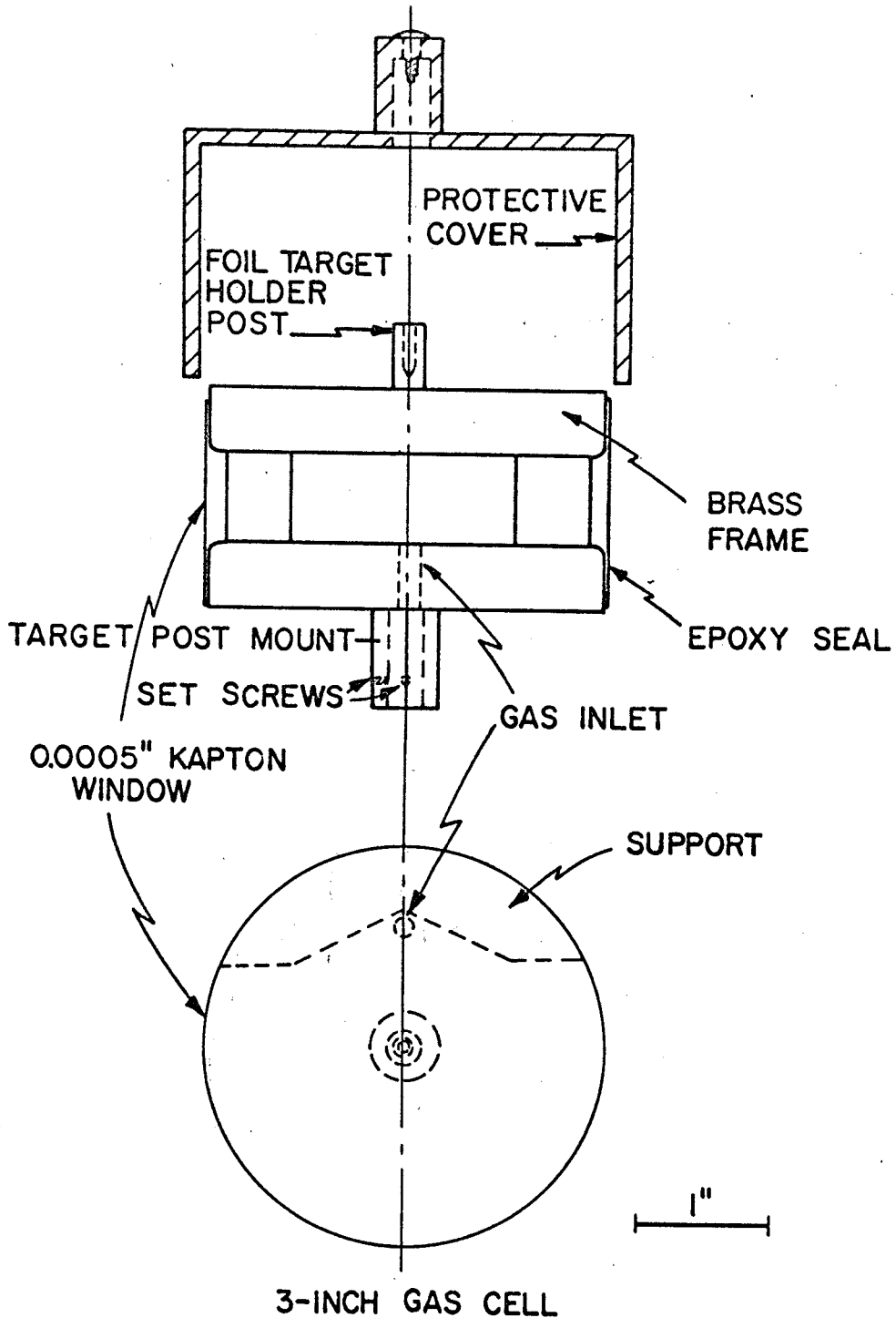

Figure III-3. Diagram of the 3-in. gas cell used in the experiment.

Kapton attached with an epoxy resin. The only disadvantage of a small cell is that the forward angle limit is determined by the scattering angle at which the counter "sees" the beam spot on the wall of the cell--the smaller the cell the larger this angle. However, with this cell data were taken as far forward as 10° in the laboratory frame with no difficulty. The smaller cell is helpful from the standpoint of resolution in that the incident and scattered particles travel through less gas and thus experience less energy straggling.

Kapton was chosen for the windows on the basis of its great strength, radiation resistance, and low density. Other foils which have been used in this laboratory are Havar* (successfully) and mylar (unsuccessfully). Kapton windows have taken hundreds of nanoampere-hours of 45 MeV protons in an 1/8 in. square spot without showing any signs of weakening. In contrast, a mylar window developed a bulge and leak after less than 50 nanoampere-hours. Beam currents as high as 300 nanoamperes have been used with the Kapton, and recent studies with 42 MeV alpha particles indicate that proton currents up to 500 nanoamperes could be used. Straggling from Kapton and mylar are

---

*Hamilton Watch Company, Lancaster, Pa.

comparable. Mylar was tried because a 0.00025 in. window was desired, and pinhole-free Kapton of that thickness was not available. On the other hand, Havar is stronger than Kapton, but has a higher effective Z and a higher density, so the straggling introduced is considerably worse.

III.B.3. Counter Systems

The counter used in the $^{16}O(p,p)$ experiments was a 0.25 in. square, 0.50 in. thick CsI(Tl) crystal mounted on the face of a photomultiplier. All other data were taken using commercial silicon surface barrier or lithium-drifted silicon detectors. The ΔE counters ranged in thickness from 54μ to 770μ depending on the incident proton energy. The E counters ranged from 270μ to 4000μ (two 2000μ counters in parallel) in thickness. All counters were cooled by circulating alcohol cooled to dry ice temperature (-78°C) through the counter mounts.

When using a gas target, two collimators are necessary to define the solid angle. A brass collimator having a lip thickness of 0.067 in. and an aperture 0.126 in. wide and ∿1.0 in. high was placed near the gas cell. This collimator was thick enough to stop all deuterons and to degrade elastic protons sufficiently in energy so that they were well-separated from the elastic protons passing through the aperture. Brass plates extended back from this collimator

to shield the detector from particles produced at the walls of the cell. A second collimator was placed immediately in front of the detector. In all of the (p,d) experiments, except the one using time-of-flight for particle identification, a 0.063 in. thick tantalum collimator with an aperture of diameter 0.1575 ± 0.001 in. was used. In the exception, an oval aperture 0.208 ± 0.001 in. long and 0.104 ± 0.001 in. wide in 0.060 in. thick tantalum was used. The second collimator for the $^{16}O(p,d)$ experiments was 0.125 in. thick tantalum with an aperture diameter of 0.125 ± 0.001 in. The rear collimator was placed from 9.1 to 14.7 in. from the center of the cell, with the corresponding distances between the two collimators ranging from 5.9 to 12.7 in. Angular acceptances corresponding to these collimator placements ranged from ∿1.2° to ∿0.6°, respectively.

III.C. Electronics

III.C.1. $^{16}O(p,p)^{16}O$ Experiments

Light from the CsI(Tl) crystal was detected by a photomultiplier tube. The signal was amplified with a Landis preamplifier and an ORTEC multimode amplifier. The signal was then analyzed, and events were stored in a 256 channel subgroup of a 4096 channel analyzer (Nuclear Data 160D). A window was set around the elastic group

using a single channel analyzer, and the resulting gate pulses were scaled.

III.C.2. $^{16}O(p,d)^{15}O$ Experiments

Most of the data were taken using two counters in a ΔE-E telescope arrangement, and particles were identified by a Goulding system. Early experiments were done using a system constructed at Michigan State University; later, an ORTEC modular system was used. A block diagram of the modular system is shown in Fig. III-4. Pulses from the detectors were amplified by Tennelec 100B charge-sensitive preamplifiers and by ORTEC selectable active filter amplifiers. The gains of the amplifiers had to be precisely matched since the E and ΔE pulses are added after amplification to produce a sum pulse which must be proportional to the total energy of the particle. A slow coincidence was required between the ΔE and E signals. Those pulses in coincidence were stretched and presented to the identifier module, which produced an energy pulse equal to $E + \Delta E$ and a "mass" pulse proportional to

$$(E + \Delta E)^{1.73} - E^{1.73}.$$

The "mass" pulse was fed into a timing single channel analyzer (TSCA) set to select pulses corresponding to deuterons. A linear gate was opened to let through only those energy pulses which corresponded to deuterons. These

pulses were analyzed and stored in a 1024 channel group of the ND-160D analyzer. The contents of the memory were punched on paper tape or "dumped" into the memory of the Laboratory's Scientific Data Systems Sigma 7 computer.

Another technique for particle identification was used quite successfully. It depended on the difference in flight times between the target and the detector for particles of different mass. A block diagram of the electronics is shown in Fig. III-5. Two counters were used--an E counter and a veto counter. The E counter thickness was sufficient to stop the deuterons of interest. Any particles passing through the E counter produced an anticoincidence pulse in the veto counter. An event in the E counter was detected by a time pickoff unit (TPO), and the resulting signal was used to start a time-to-amplitude converter (TAC), which was stopped by the cyclotron RF pulse. Since deuterons are the only stable mass 2 particles, their identification by time-of-flight was unambiguous. The time resolution was approximately 0.8 nsec. The E signal was amplified with an FET preamplifier and a selectable active filter amplifier. A slow coincidence was required between the energy and time signals which were input to the ND-160D analyzer used in the 64 x 64 channel mode. A window was then set, using a timing single channel

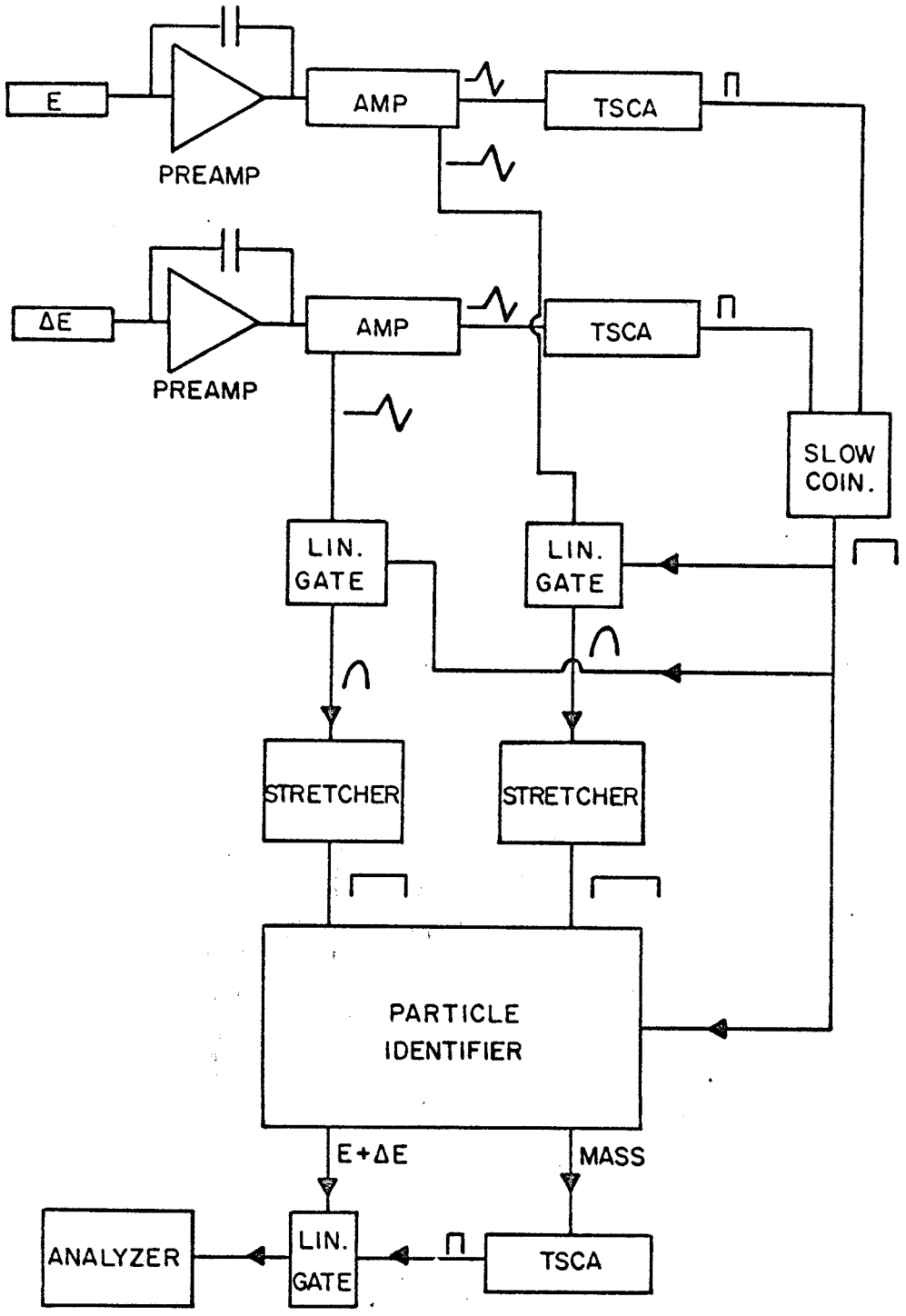

Figure III-4. Block diagram of the electronics for the Goulding method of particle identification.

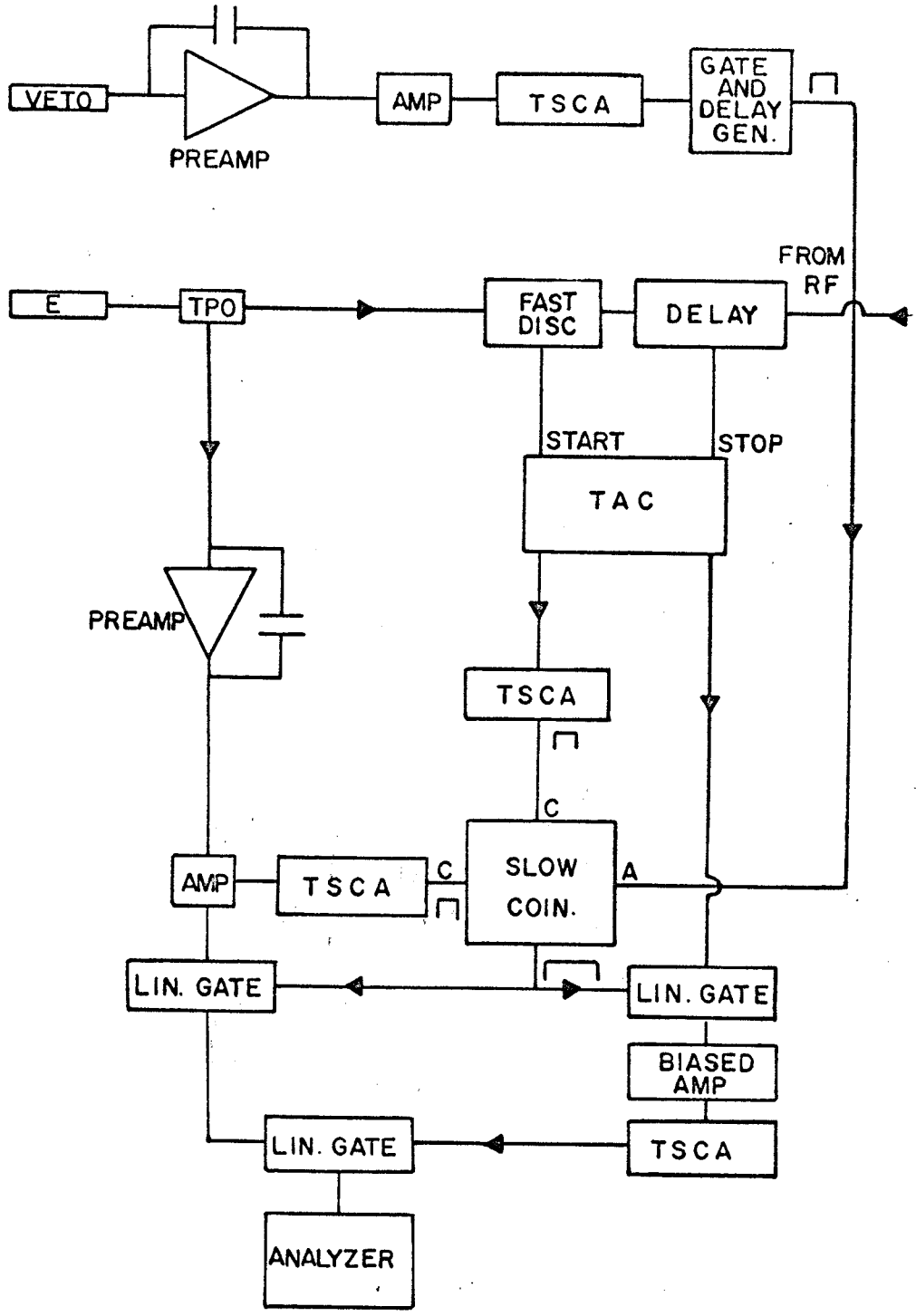

Figure III-5. Block diagram of the electronics for the time-of-flight method of particle identification.

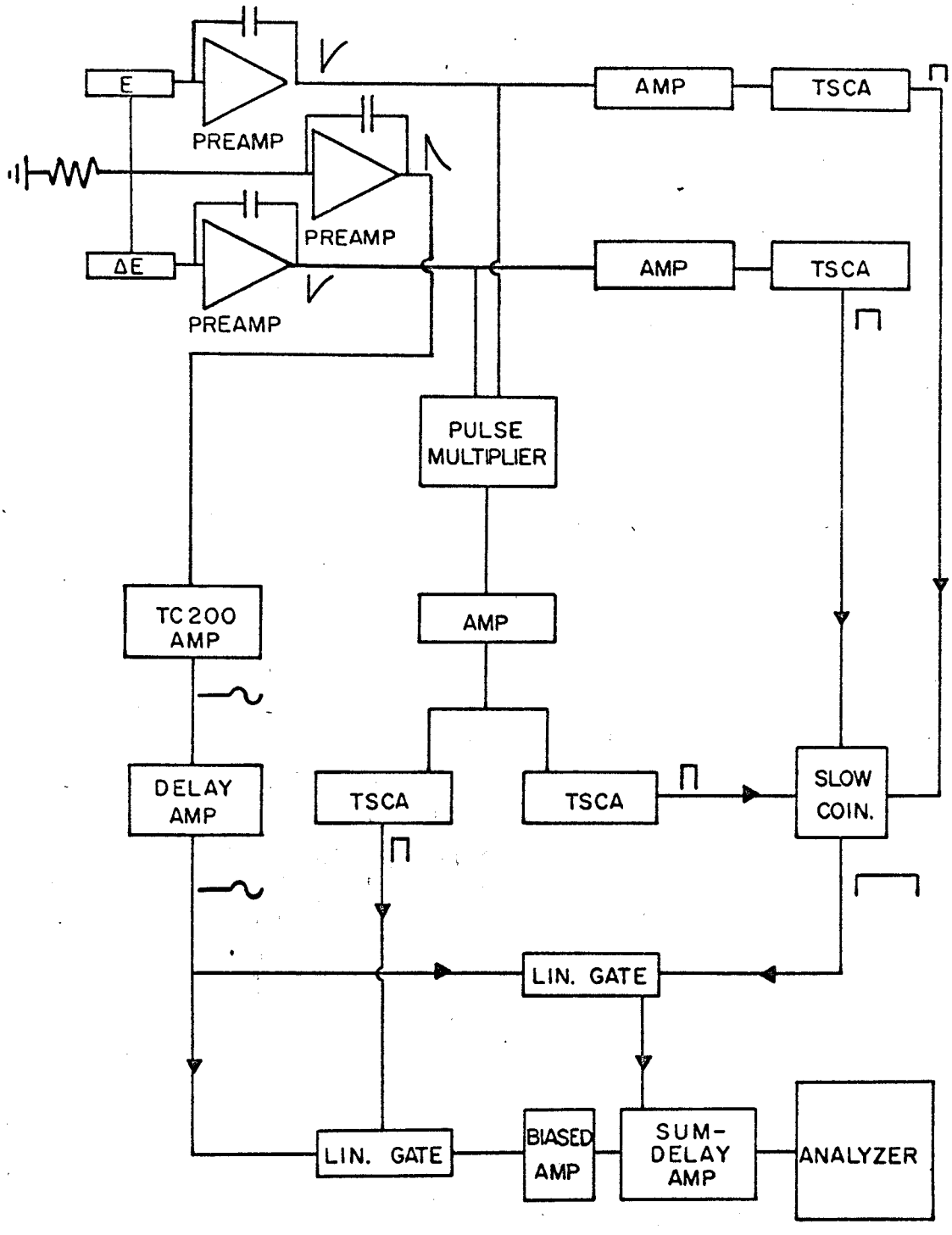

Figure III-6. Block diagram of the electronics for the pulse multiplication method for particle identification.

analyzer, to include only time pulses corresponsing to the deuterons. This signal was used to gate the energy pulses which were analyzed in the 1024 channel one-dimensional mode of the analyzer.

III.C.3. $^{15}N(p,p)^{15}N$ and $^{15}N(p,d)^{14}N$ Experiment

In this experiment an E-ΔE telescope was again used, but the particle identification was not done with a Goulding system. Instead, a pulse multiplier was used. A block diagram is shown in Fig. III-6. The E and ΔE pulses were amplified using Tennelec 100B charge-sensitive preamplifiers, then were fed into a pulse multiplier designed by V. Radeka and G. Miller (Mi 63). The pulse produced has the form

$$\Delta E(E + K_1 \Delta E + K_2)$$

which can be shown to be roughly proportional to MZ^2 of the particle (Gl 65).

The E and ΔE signals were summed at the detectors by placing a 5 megohm resistor between the normally grounded sides of the detectors and ground. The sum signal was amplified with an FET preamplifier and a Tennelec TC-200 amplifier and then was delayed by the amount of time necessary to place it in coincidence with delayed E and ΔE signals and the output of the pulse multiplier. The energy and mass signals were fed into the two sides of the ND-160D analyzer used in the 64 x 64 channel mode. By adjusting the

gains of the E and ΔE amplifiers in the pulse multiplier and the values of the constants K_1 and K_2, the different mass groups could be made to appear as straight bands in the two-dimensional spectrum. Windows were then set to include all the deuterons and the elastic protons (which were not stopped by the detectors and thus produced a mass pulse smaller than those of protons which were stopped) using two timing single channel analyzers. The proton pulses were sent through a biased amplifier to reduce their heights to values less than that of any deuteron pulse and then added to the deuteron pulses. Since these pulses did not arrive in coincidence, the sum signal contained either a proton pulse or a deuteron pulse. This signal was then input into a 4096 channel analyzer (Nuclear Data NDZ200). The spectra were stored in 1024 channel groups and contained both the elastic protons and the deuterons.

III.C.4. Comparison of the Systems for Particle Identification

Each of the systems described offers some advantages and disadvantages. With the exception of the pulse multiplier, all components necessary for each system are available in standard modular form. The Goulding system has a greater mass range than the multiplier system. A disadvantage

for high resolution work is the necessity of matching gains of the E and ΔE amplifier systems to high precision. This is especially true if one uses the $E + \Delta E$ output of the identifier module. It was quite difficult to have the gains match well over the energy range of the incoming particles. Also, the E and ΔE pulses must pass through a relatively large number of stages before being added and analyzed. The electronic noise using this system was typically 45 to 50 keV. This figure could undoubtedly be improved if one were to sum the E and ΔE pulses at the detectors, as was done with the pulse multiplier system. Then one could use the Goulding system only to produce mass pulses. Electronic noise in the sum pulses was approximately 30 keV for the pulse multiplier system. All noise values quoted were measured with the detectors cooled and under bias.

The best overall resolution was obtained with the time-of-flight system. Here again, the energy pulse passed through only a preamplifier, amplifier, and linear gate. Perhaps the greatest advantage of this system is that one gets the energy information from a single detector. Thus, the particle passes through only one detector "dead" layer instead of three. Also, the single, thick E counter has a much lower capacitance than the relatively thin ΔE counters that must be used for low-energy particles, thus

introducing less noise. The electronic noise for this system was approximately 20 keV. Of course, an obvious disadvantage of time-of-flight is its inability to distinguish between particles of the same mass such as ^{3}H and ^{3}He. However, deuterons, being the only stable mass 2 particles, are well-separated from protons and from the mass 3 particles. Another disadvantage is the fact that the mass lines are curved in an E vs t plot. This means that a linear "time" gate may not be sufficient to separate pulses corresponding to particles with different masses. If not, one must rely on the Q-values of the different reactions involved to keep clear the energy region of interest. This problem can be eliminated if an on-line computer such as the Sigma 7 is available. At present (but not when the data using time-of-flight were taken) one can use the computer as an analyzer and have it store events appearing in a curved band in the E-t plane.

III.D. Data Acquisition and Analysis

III.D.1. Data Acquisition

After the initial alignment of the beam and the initial adjustment of mass gates, etc., angular distributions were begun at forward angles. In order to minimize the dead time of the electronics and analyzer, the beam was kept at such a level that pileups seen on an oscilloscope monitoring the

output of the E amplifier were few. In all of the (p,d) work using the Goulding system, pulses corresponding to elastic protons were eliminated before reaching the identifier by requiring that the energy lost by a particle in the ΔE counter be greater than that lost by the elastics.

Zero corrections to the scattering angles indicated by the digital readout system were obtained by comparing values of the differential cross sections measured on both sides of the beam at angles where the slope of the angular distribution was steep. Progress of the experiment was monitored by calculating and plotting a relative cross section for one of the strongly excited states (usually the ground state). Often, as a check on consistency, at least one angle would be repeated. At periodic intervals the mass gate was checked and adjusted if necessary.

Angular distributions were generally taken from 10° to approximately 160° in the laboratory frame. Five-degree steps were used to approximately 70°, and then 7.5° steps were used. At times, additional intermediate points were taken between 10° and 20° to determine better the first peak of the angular distribution.

III.D.2. Data Analysis

The data stored in the analyzers were dumped either on paper tape or into the memory of the Sigma 7 and then punched

on computer cards for use by analysis programs. All spectra were plotted using the CALCOMP plotting routine of P. J. Plauger. Each peak was then identified by the channel numbers corresponding to each edge, and a background value was assigned at each edge on the basis of counts in neighboring "clear" regions of the spectrum. These data, along with the cards containing the spectrum, were input to the program PEAKSTRIP (written by R. A. Paddock) which computed a linear background under the peak, the centroid of the peak, the width of the peak (assuming a Gaussian shape), and the net area and background. The program punched all of these data on cards to be used in other programs. Also available were several data analysis routines which use the display oscilloscope connected to the Sigma 7. They allowed one to fit backgrounds of various polynomial orders either to an individual peak or to groups of peaks. Analyses with these programs were compared to those using PEAKSTRIP and were found to agree very well. Linear backgrounds under each peak were satisfactory. The scope analysis programs were not used extensively since that would have involved many hours of computer time.

The excitation energies of the peaks were determined by using the program GASCELCAL written by R. A. Paddock. Input data consisted of the PEAKSTRIP output data for all

angles at a given incident proton energy and data giving information about the target gas, scattering angles, and excitation energies of peaks to be used as calibration points. The program then produced a calibration curve of channel number vs particle energy at the detector by calculating the appropriate reaction kinematics and the energy losses of the incident and scattered particles in the gas and in the walls of the gas cell. Generally, a quadratic fit was used. The program then calculated the excitation energy of each peak in each run and listed it according to peak number. Since the energy levels of ^{15}O and ^{14}N are quite well-known, these calculations served mainly to identify the peaks. A useful option of this program allowed one to find, according to the calibration curve, the position of peaks corresponding to levels not observed in a particular spectrum. This method was used to search for peaks corresponding to the (p,d) reaction on the most likely target contaminant, ^{14}N. In those cases in which a measurable amount of ^{14}N contamination was found [the ^{15}N(p,d) data and one set of ^{16}O(p,d) data], the amount present was calculated by comparing the differential cross sections of one of the strongly excited states of ^{13}N to the values measured by Kozub et al. (Ko 67) at 33 MeV. Once the amount had been determined, the number of counts in any peak which overlapped a ^{13}N peak was corrected.

In the $^{16}O(p,p)$ experiments two additional corrections to the number of counts were made. A dead-time correction was made on the basis of a comparison of the scaled proton counts to those analyzed. This correction was significant only at laboratory angles smaller than 30°, and in most cases was less than 2%. However, the data taken at 38.43 MeV showed an 8% correction at 10°, but this number had dropped to 2% at 20°. The other correction was for counting losses due to reactions in the CsI(Tl) crystal. This correction was based on the following empirical expression deduced from data on NaI (Ca67):

$$\% \text{ Loss} = 0.001062\ E^2 + 0.01392\ E - 0.1554. \qquad \text{(III.1)}$$

This correction was approximately 2% at forward angles and decreased with the kinematic drop in energy of the scattered protons. These numbers agree well with results of a calculation in which the cross section for a reaction is assumed to be the geometrical cross section, so that the total probability of a reaction can be determined from range and density data.

Dead-time corrections were not necessary for the (p,d) data owing to the much smaller counting rates. Using the geometrical approximation described, calculations of counting losses for deuterons in silicon were made. These were less than 1% owing to the smaller range of deuterons in the silicon. Hence, no correction was made to the data.

When all necessary corrections were made, the yields and backgrounds were fed into a program which calculated the differential cross section for each level at each angle at which it was observed. The expression for the cross section in the laboratory frame can be written as

$$d\sigma/d\Omega = Y\sin\theta/nNG, \qquad \text{(III.2)}$$

where Y is the yield, n is the number of incident particles, and N is the number of target atoms per cm^3. The quantity G is a geometrical factor, to be found in a paper by Silverstein (Si 59), which contains terms accounting for effects due to a finite beam size and finite collimator apertures. The calculations of Silverstein have been extended by R. A. Atneosen (At 67) to include the case of an oval rear collimator. The G-factor can be written as

$$G = \frac{2Ab}{R_o h}\left(1 + \Delta_o + \frac{\sigma'}{\sigma}\Delta_1 + \frac{\sigma''}{\sigma}\Delta_2 + \ldots\right), \qquad \text{(III.3)}$$

where A is the area of the rear collimator aperture, b is the half-width of the front collimator aperture, R_o is the distance between the rear collimator and the center of the cell, h is the distance between the front and rear collimators, and the Δ_i are correction terms depending on the geometry of the beam and collimators. Inclusion of the Δ_o and Δ_1 terms have made differences of less than 0.1% at all angles. The Δ_o term has been included in all calculations. The program calculated cross sections in the

laboratory and center-of-mass frames and computed the statistical error according to the formula

$$e = \frac{\sqrt{Y + 2B}}{Y}, \qquad \text{(III.4)}$$

where Y is the net yield and B is the background. A total error was also computed in which the statistical error was added, in quadrature, to errors associated with other quantities in the calculation. An option allowed the angular distribution to be plotted on the CALCOMP plotter.

III.E. Analysis of Experimental Uncertainties

III.E.1. Beam Energy and Energy-Level Determination

The beam energy was determined from the values of the decapot settings of the analyzing magnet power supplies, which were calculated from the measured field values. Extensive checks of the energies thus determined have not been made over the range from 20 to 50 MeV, but a check at 33 MeV using the range-energy method described by Kull (Ku 67) and Kozub (Ko 67 a) was consistent with an uncertainty of ±100 keV.

The energy resolution for the $^{16}O(p,d)$ data was typically 100 keV, except for the data taken using the single counter and time-of-flight, where the resolution was approximately 60 keV. The resolution for the $^{15}N(p,d)$ data was approximately 90 keV. Major contributions to the resolution are given

in Table III-1. The quantity labelled "Other" includes the energy spread involved in charge collection in the detectors and straggling in the dead layers of the detectors, as well as other unknown sources.

The error in the energies of the excited levels depends upon the energy resolution to the extent that the error in the centroid of the peak is related to the width of the peak and to the extent that some peaks could not be resolved from adjacent peaks. The error in the centroid is also related to the number of counts in the peak. The contribution from the uncertainty in the absolute beam energy was negligible. Thus, for the relatively weak excited states an uncertainty as great as 15 keV could be expected. The overall calibration curve calculated by the code GASCELCAL had a typical uncertainty of 15 keV owing to scatter in the points. The average deviation of the calculated excitation energies was typically 20 keV. Of course, this number reflects the uncertainty in the calibration curve. Thus, an error of at least 20 keV should be attached to each excitation energy measured.

III.E.2. Differential Cross Sections

The major sources of error in the determination of the absolute differential cross sections are shown in Table III-2.

Table III-1. Contributions to the energy resolution obtained with the three methods of particle identification.

Source of Contribution	Goulding System[a]	Pulse Multiplier System[b]	Time-of Flight System[c]
Electronic noise	50 keV	35 keV	25 keV
Proton straggling in cell wall	6	7	8
Proton straggling in gas	12	8	5
Deuteron straggling in cell wall	17	18	30
Deuteron straggling in gas	32	14	22
Kinematic broadening	80	65	25
Beam resolution	36	32	16
Other	21	31	25
TOTAL	110 keV	90 keV	60 keV

[a] 45 MeV incident protons.
[b] 40 MeV incident protons.
[c] 32 MeV incident protons.

Table III-2. Estimated uncertainties in quantities involved in the calculation of absolute cross sections for $\theta_{LAB} \approx 30°$. The uncertainties are to be treated as standard deviations.

Type of Uncertainty	Value
Target temperature	1.5%
Target pressure	1.0%
Charge integration	1.5%
Solid angle determination	2.2%
Scattering angle (0.2°): $[d\sigma(\theta)/d\theta]$	1.6%
Total Measurement Uncertainty	3.6%

Although not shown, the uncertainty in the determination of the background counts for each peak was considered. This uncertainty was negligible for large peaks, but became significant for small peaks superimposed on rather large backgrounds. Even for those, however, this error was still smaller than the corresponding statistical error. Other sources of uncertainty not listed include those in the dead-time and counting loss corrections, which were themselves small. The effect of the uncertainty in beam energy was neglected since the differential cross sections changed slowly with incident proton energy (see Chapter V). An additional contribution to the uncertainty in the differential cross sections is the statistical error,

which must be added, in quadrature, to the measurement error. The statistical error was different for each data point, and ranged from 0.2% upward, depending on the strength of the level. The error bars shown on all data points represent the total error. Statistical and total errors are tabulated with the data in the appendices for the more strongly excited levels.

CHAPTER IV

ELASTIC SCATTERING DATA AND OPTICAL MODEL PARAMETERS

IV.A. Proton Elastic Scattering

IV.A.1. $^{16}O(p,p)^{16}O$

Differential cross sections for the elastic scattering of protons by ^{16}O were measured at incident energies (corrected for losses in the cell window and gas) of 25.46, 32.07, 35.10, 38.43, and 45.13 MeV over an angular range of 10° to 170° in the center-of-mass frame. Details of the experimental apparatus and procedures were discussed in Chapter III. At the end of each angular distribution the differential cross section at the position of the second maximum (50-60°) was measured over an energy range of $\pm$300 keV around the bombarding energy to detect the presence of any sharp resonances in the cross section. No significant fluctuations were found. As a check on the efficiency of the counter system, differential cross sections for the elastic scattering of protons by protons were measured at several angles between 15° and 22° in the laboratory frame. These were compared to those

measured by Johnston and Swenson (Jo 58) and were found to agree within the experimental errors.

A sample spectrum is shown in Fig. IV-1, and the five experimental angular distributions are shown in Fig. IV-2. They exhibit a rather smooth energy dependence, with the 25.46 MeV angular distribution showing a slightly different behavior beyond 60°. These data are in quantitative agreement with those of Cameron et al. (Ca 68), whose measurements covered the energy range 23.4--46.1 MeV. These authors found that the behavior of the cross sections below 30 MeV indicated the existence of broad resonances or intermediate structure in the p-^{16}O system. The behavior of the 25.46 MeV data is consistent with such a conclusion. These resonances were too broad to have been detected during the search for sharp resonances within 300 keV of the original proton energy.

IV.A.2. $^{15}N(p,p)^{15}N$

Differential cross sections for the elastic scattering of protons by ^{15}N were measured simultaneously with the measurement of the $^{15}N(p,d)^{14}N$ differential cross sections as has been described in Chapter III. The incident proton energy was 39.84 MeV, and an angular range of 10° to 145° in the center-of-mass frame was covered. The data are shown in Fig. IV-6 with the optical model fit discussed in

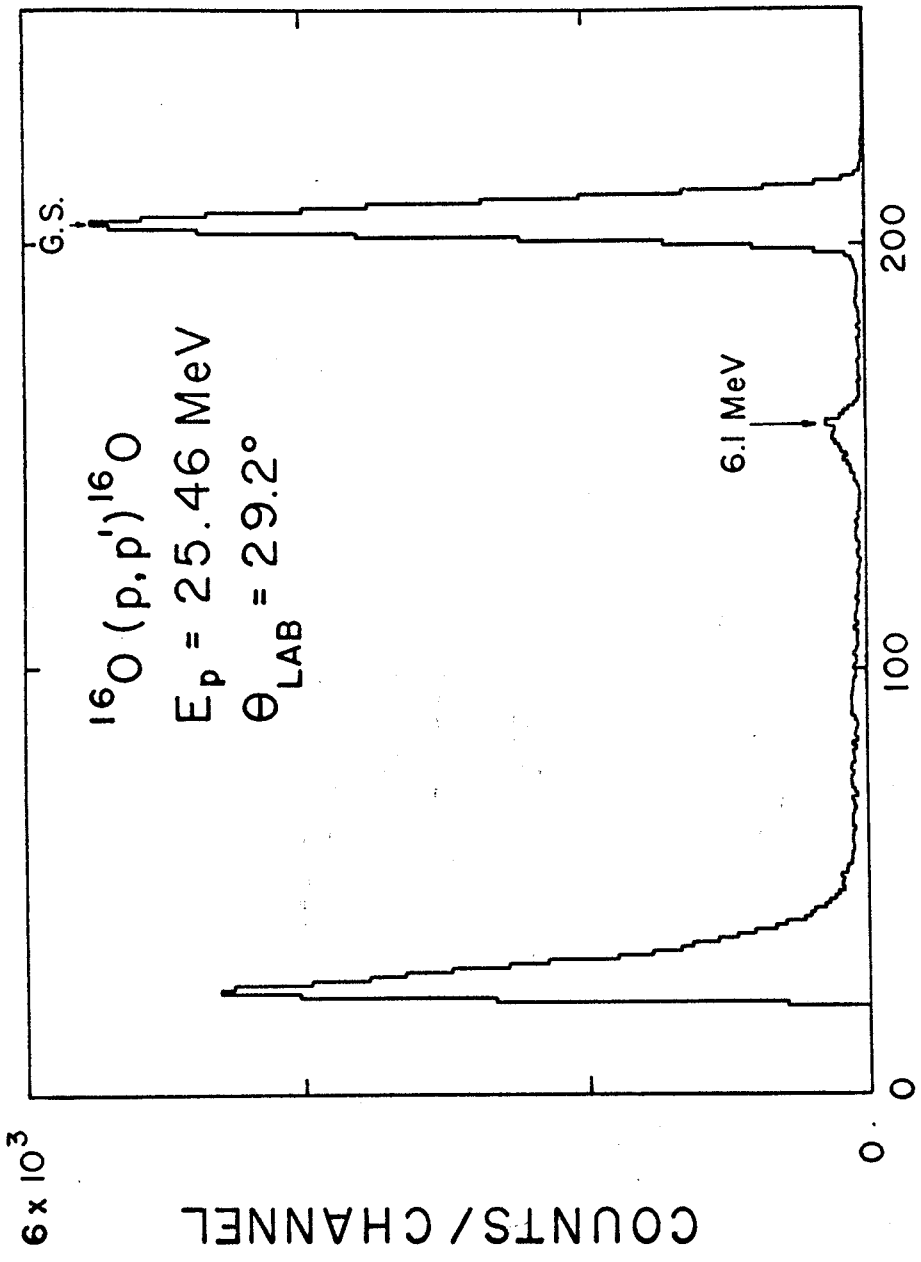

Figure IV-1. $^{16}O(p,p')^{16}O$ spectrum at θ_{LAB}=29.2° for E_p=25.46 MeV. The large number of counts around channel 30 are due to elastic protons which have passed through the lip of the front collimator.

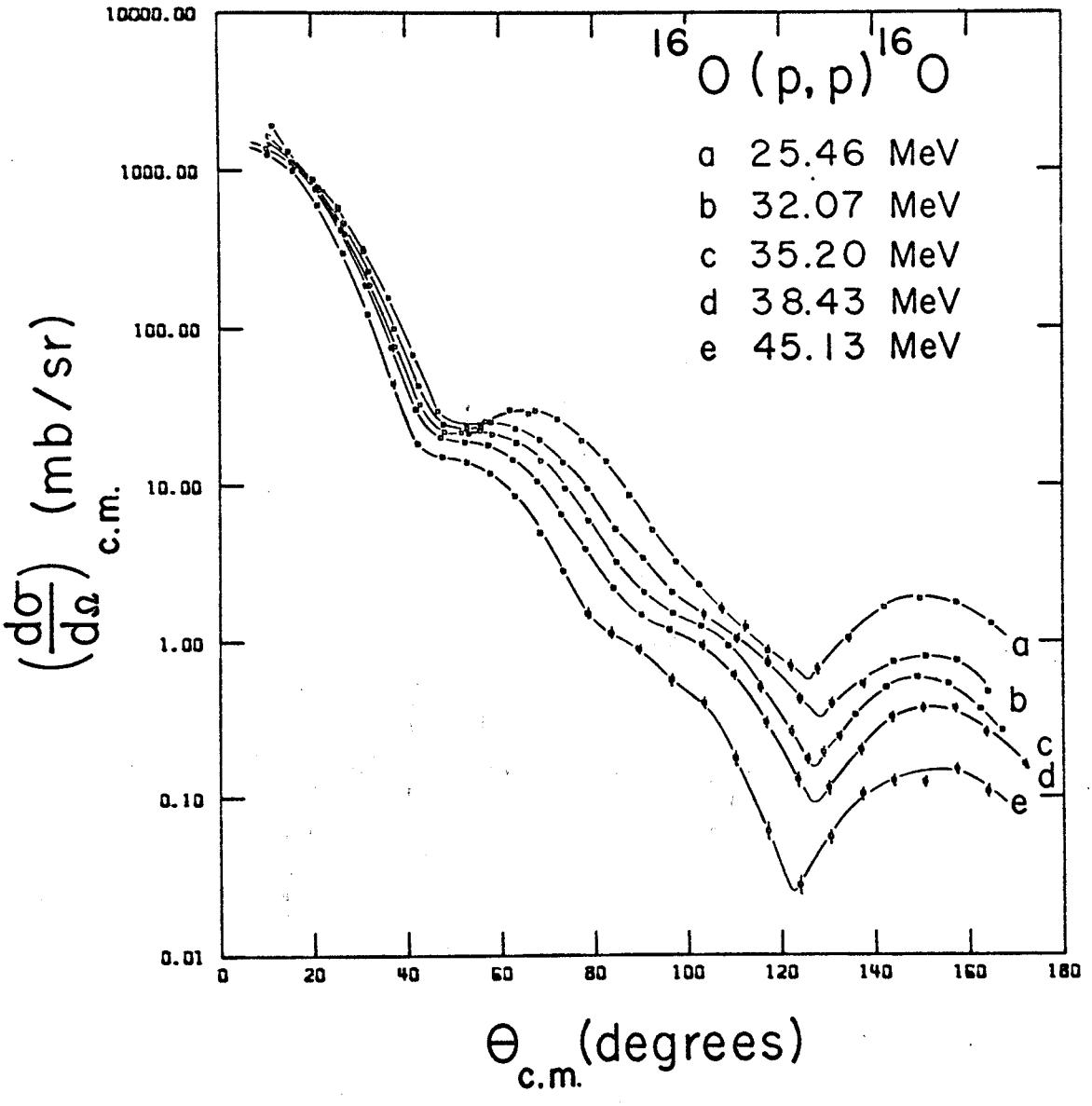

Figure IV-2. $^{16}O(p,p)^{16}O$ experimental angular distributions for E_p=25.46--45.13 MeV.

Section IV.B.2. This angular distribution is very similar to the oxygen angular distributions in the appropriate energy range.

IV.B. Optical Model Analysis of the Proton Elastic Scattering Data

In the optical model of elastic scattering it is assumed that the interaction of the two nuclei involved can be represented by scattering from a one-body complex potential having the form

$$V_{opt}(r) = V_c(r) - Vf(x) - i(W_S - 4\, W_D \frac{d}{dx'})f(x')$$

$$+ V_{so}\left(\frac{\hbar}{(m_\pi c)^2}\right)^2 \frac{1}{r}\frac{df(x)}{dr}\,(\underline{\ell}\cdot\underline{\sigma}),$$

where $V_c(r) = \dfrac{ZZ'e^2}{r}$, $r = R_c$ (IV.1)

$$= ZZ'e^2(3 - \frac{r^2}{R_c^2})/2R_c,\ r = R_c$$

$$R_c = r_c A^{1/3},$$

and $f(x) = (e^x + 1)^{-1}$,

with $x = (r - r_R A^{1/3})/a_R$, $x' = (r - r_I A^{1/3})/a_I$.

V_c is the potential felt by a point charge (Ze) interacting with a uniformly charged sphere of radius (R_c) and charge (Z'e).

Optical model analyses were performed with the Perey search code GIBELUMP*, which runs on both the CDC 3600 and the SDS Sigma 7 computers. The potentials and geometrical parameters could be varied singly or in combination. In general, the spin-orbit radius and diffuseness were set equal to the corresponding parameters of the real well, although this condition was not imposed by the code. The code sought to minimize the quantity

$$\chi^2/N = (1/N)\sum_i \{[\sigma_{th}(i) - \sigma_{exp}(i)]/\Delta\sigma_{exp}(i)\}^2, \qquad \text{(IV.2)}$$

where N is the number of experimental data points, $\sigma_{th}(i)$ and $\sigma_{exp}(i)$ are the theoretical and experimental cross sections at angles θ_i in the center-of-mass frame, and $\Delta\sigma_{exp}(i)$ is the error in $\sigma_{exp}(i)$.

As is well-known, the optical parameters exhibit certain ambiguities, such as the one represented by a constant value of Vr^2. To determine the effect of changing a given parameter and hence to determine which combinations of parameters would produce unambiguous results, the calculations represented in Fig. IV-3 were performed. The solid lines represent the standard calculation using the parameter values listed. Each

---

*Unpublished FORTRAN-IV computer code written by F. G. Perey and modified by R. M. Haybron at Oak Ridge National Laboratory.

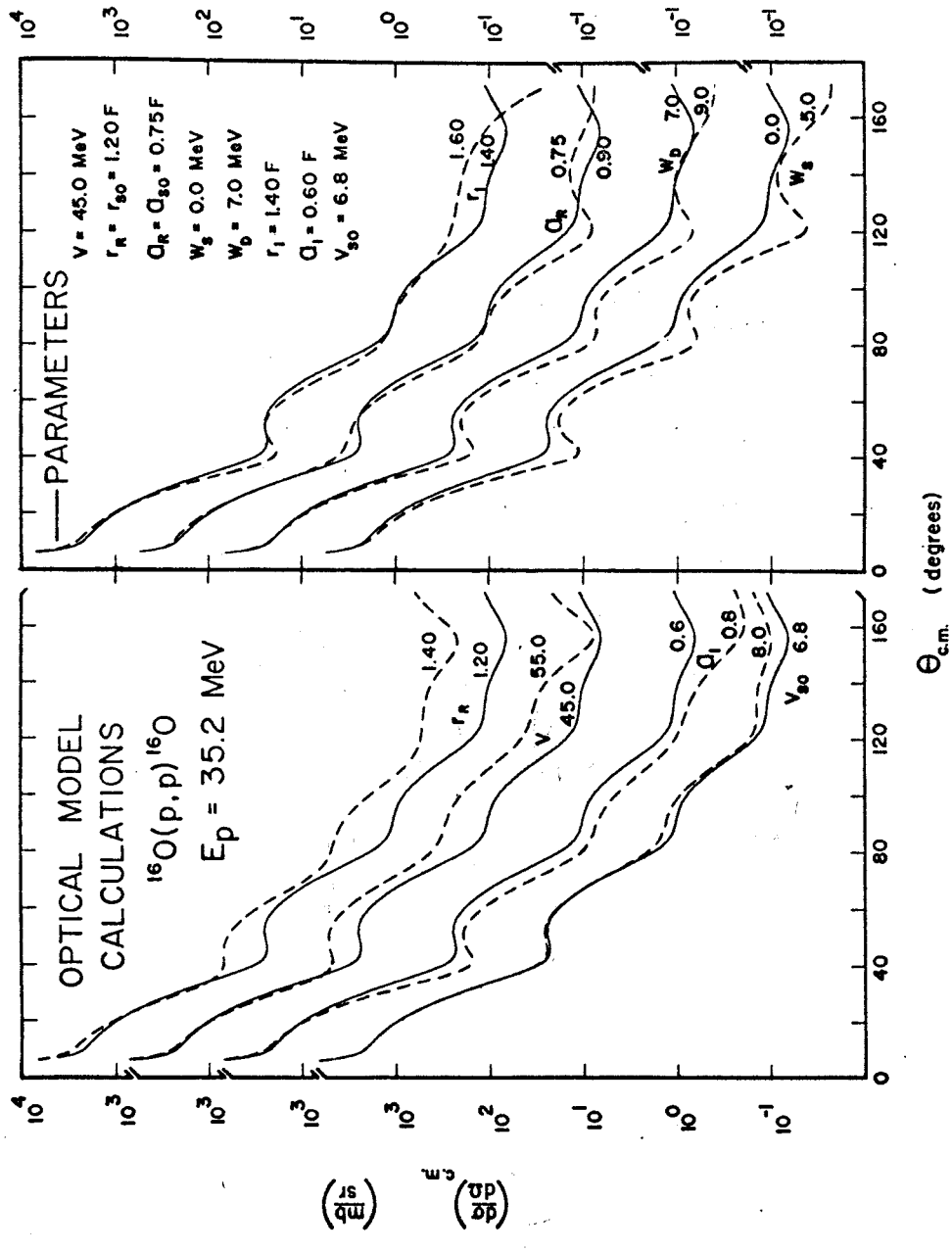

Figure IV-3. Effects of variations of individual optical model parameters on the calculated $^{16}O(p,p)^{16}O$ angular distributions. The solid curve represents a calculation using the parameters listed, and the dashed curve represents a calculation with one of the parameters increased.

dashed curve represents the effect of changing one parameter. It is interesting that a sizable change in V_{so} has very little effect on the calculated angular distribution.

IV.B.1. $^{16}O(p,p)^{16}O$

In the initial phase of the calculations an effort was made to obtain the set of parameters which gave the best overall fit to the five experimental angular distributions. Unambiguous combinations of parameters were searched on until the average χ^2/N was a minimum. The parameters and fits are shown in Fig. IV-4. The fits are only fair at forward angles and completely out-of-phase at the back angles. The relatively low value of 1.12 F for R_R was chosen on the basis of better fits.

Owing to non-locality effects not included in the optical potential, one expects the parameters to be somewhat energy-dependent. Starting from the average parameters, searches were made allowing the parameters to vary with the energy of the incident proton. It was found that the real radius and diffuseness parameters tended not to vary, so they were fixed at 1.12 F and 0.69 F, respectively. Owing to the lack of polarization data to be fitted simultaneously with the elastic scattering, no effort was made to search on V_{so}. As was pointed out earlier, the calculation was not sensitive to variations of V_{so}. A

value of 7.0 MeV for V_{so} was chosen on the basis of parameters found by Cameron (Ca 67) during preliminary analyses of elastic scattering (Ca 68) and polarization data (El 68). Cameron (Ca 67) had also measured reaction cross section data at incident proton energies appropriate to his work. Since these varied smoothly with energy, values of the reaction cross section (σ_R) for the incident proton energies of the present work were extracted by graphical interpolation. These were used as a guide in choosing between sets of optical parameters which gave essentially identical values of χ^2/N.

An effort was also made to keep as smooth as possible the variation of the parameters with energy. Thus, a set of parameters producing a much better value of χ^2/N for the 38.43 MeV data was judged unacceptable because the value of a_I was much smaller than those obtained for the other data. The final set of parameters is shown in Table IV-1, and the corresponding fits are shown in Fig. IV-5. It was found that the inclusion of a volume imaginary potential was necessary above 32.07 MeV, with its strength increasing with energy. This is probably due to the deeper penetration of the more highly energetic protons. The forward angle fits are improved, although the improvement is slight for the 25.46 MeV data. The back angle fits are very poor for

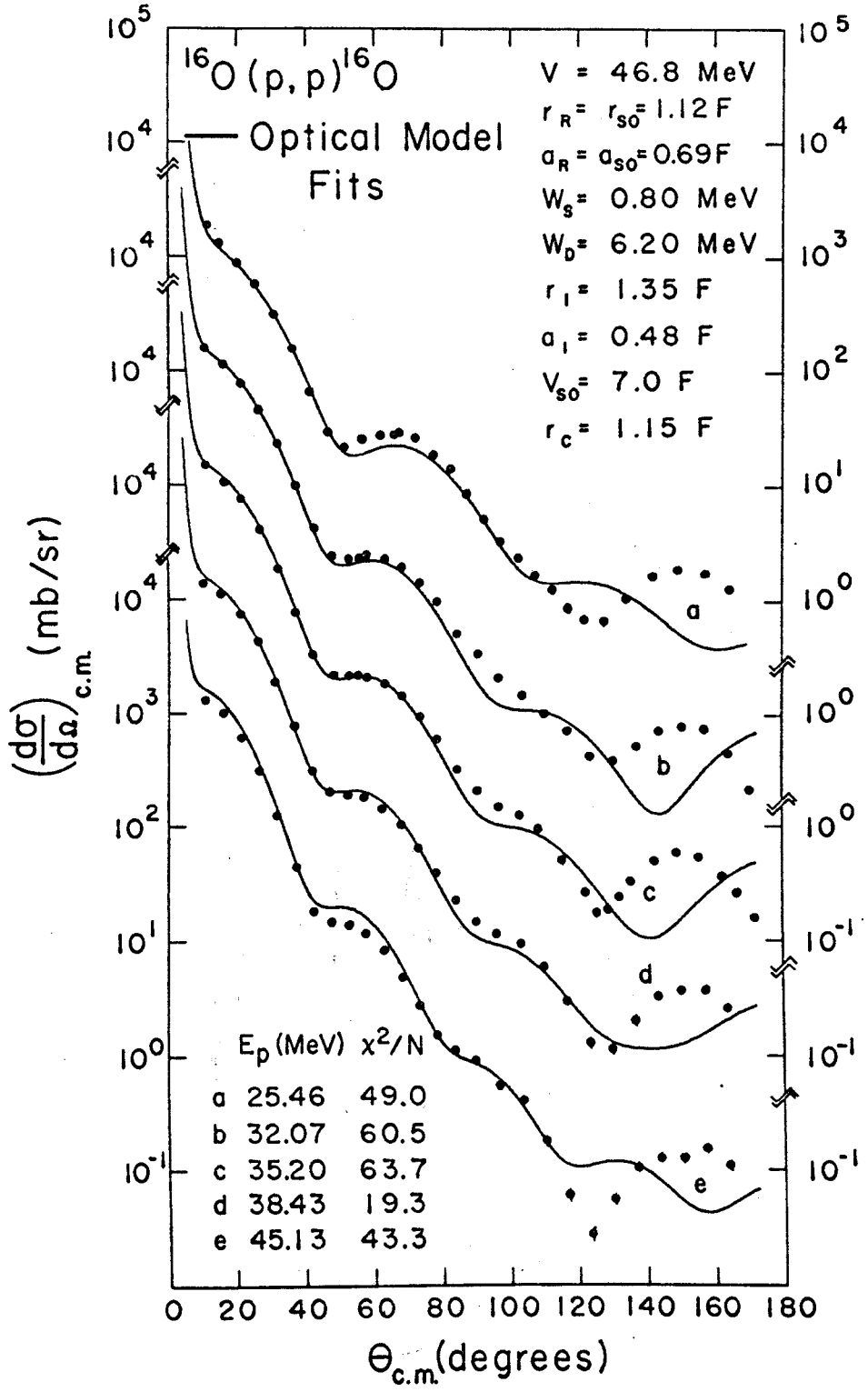

Figure IV-4. Optical model fits to the $^{16}O(p,p)^{16}O$ angular distributions using the average set of parameters listed. The average value of χ^2/N is 47.2.

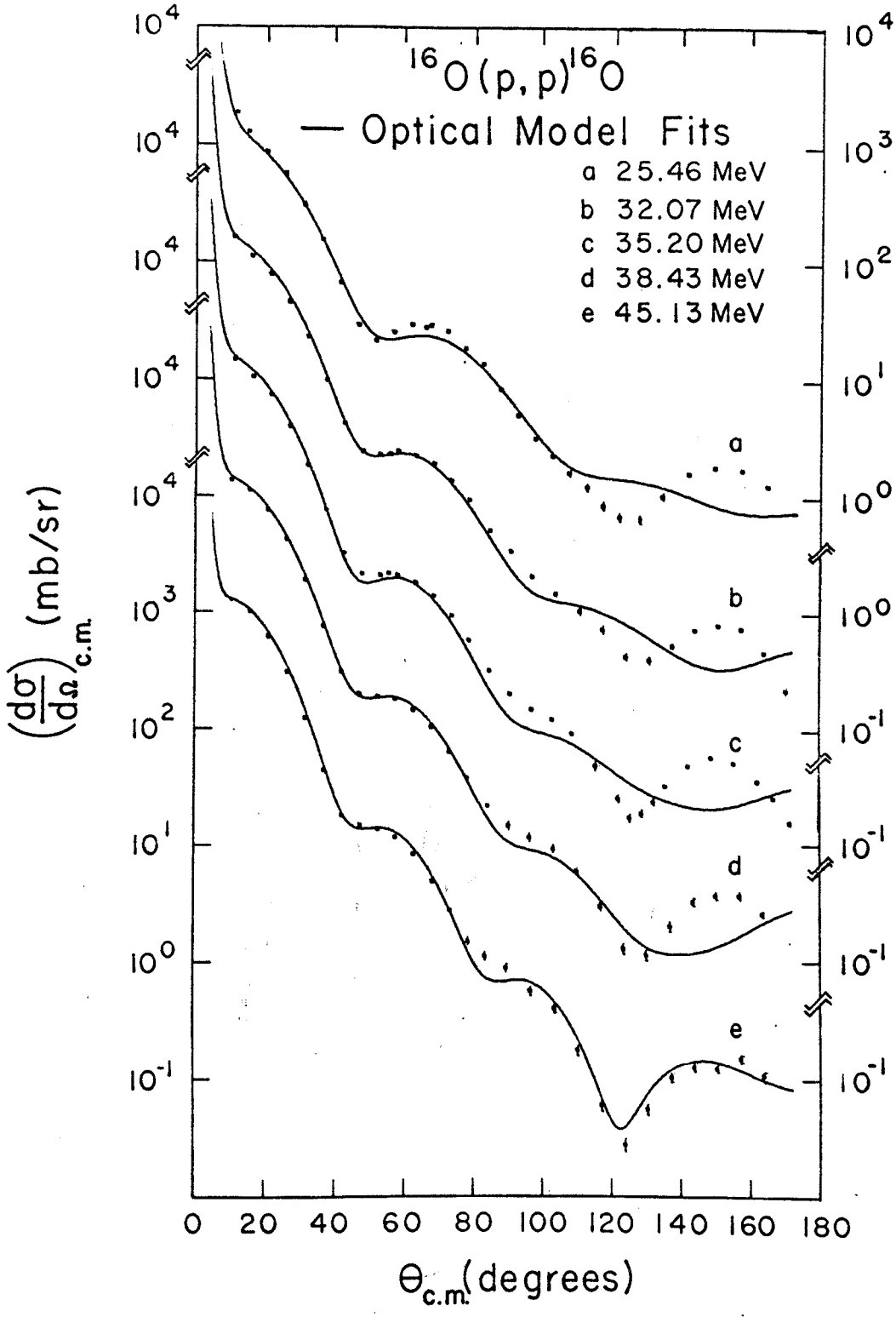

Figure IV-5. Optical model fits to the $^{16}O(p,p)^{16}O$ angular distributions using the energy-dependent sets of parameters listed in Table IV-1. The average value of χ^2/N is 27.1.

Table IV-1. Optical model parameters describing proton elastic scattering from ^{16}O and ^{15}N.

Target	E_p (Lab) (MeV)	V (MeV)	r_R (F)	a_R (F)	W_S (MeV)	W_D (MeV)	r_I (F)	a_I (F)	V_{so} (MeV)	σ_R(exp)* (mb)	σ_R(th) (mb)	χ^2/N
^{16}O	25.46	48.4	1.12	0.690	0.0	6.80	1.19	0.550	7.0	507	535	36.7
^{16}O	32.07	45.5	1.12	0.690	0.0	5.31	1.44	0.490	7.0	473	487	32.3
^{16}O	35.20	45.0	1.12	0.690	0.91	5.70	1.45	0.450	7.0	458	498	45.3
^{16}O	38.43	44.4	1.12	0.690	2.00	4.89	1.40	0.430	7.0	441	446	16.5
^{16}O	45.13	42.7	1.12	0.690	3.11	5.65	1.28	0.415	7.0	407	407	4.9
^{15}N	39.84	43.9	1.13	0.660	4.54	2.93	1.42	0.483	8.0	---	455	5.5

$r_{so} = r_R$, $a_{so} = a_R$, $r_c = 1.15$ F.

*Based on data found in Ref. Ca 67.

all but the 45.13 MeV data. This behavior is consistent with that found by van Oers and Cameron (Va 68) over the energy range of 23-53 MeV, by Barrett, et al. (Ba 65) at 30.3 MeV, by Kim et al. (Ki 64) at 31.0 MeV, and by Fannon et al. (Fa 67) at 49.48 MeV. It has been found in other work (Fr 67) that the use of a spin-orbit radius parameter of 10% to 15% smaller than the real radius parameter was helpful in obtaining fits to the back angle data. This was tried with no significant improvement. Thus, it appears that the optical model gives a poor description of proton elastic scattering from ^{16}O below 30 MeV where resonances occur, that between 30 and 40 MeV the description is poor beyond 100° in the center-of-mass frame, and that the optical model describes the scattering very well for incident protons above 40 MeV.

IV.B.2. $^{15}N(p,p)^{15}N$

Similar procedures were followed to obtain a set of parameters which describe the elastic scattering of protons from ^{15}N. The parameters are listed in Table IV-1, and the fit is comparable to that for the 38.43 MeV ^{16}O data, as was expected owing to the similarity of the incident proton energies. The optical model fit to the data is shown in Fig. IV-6.

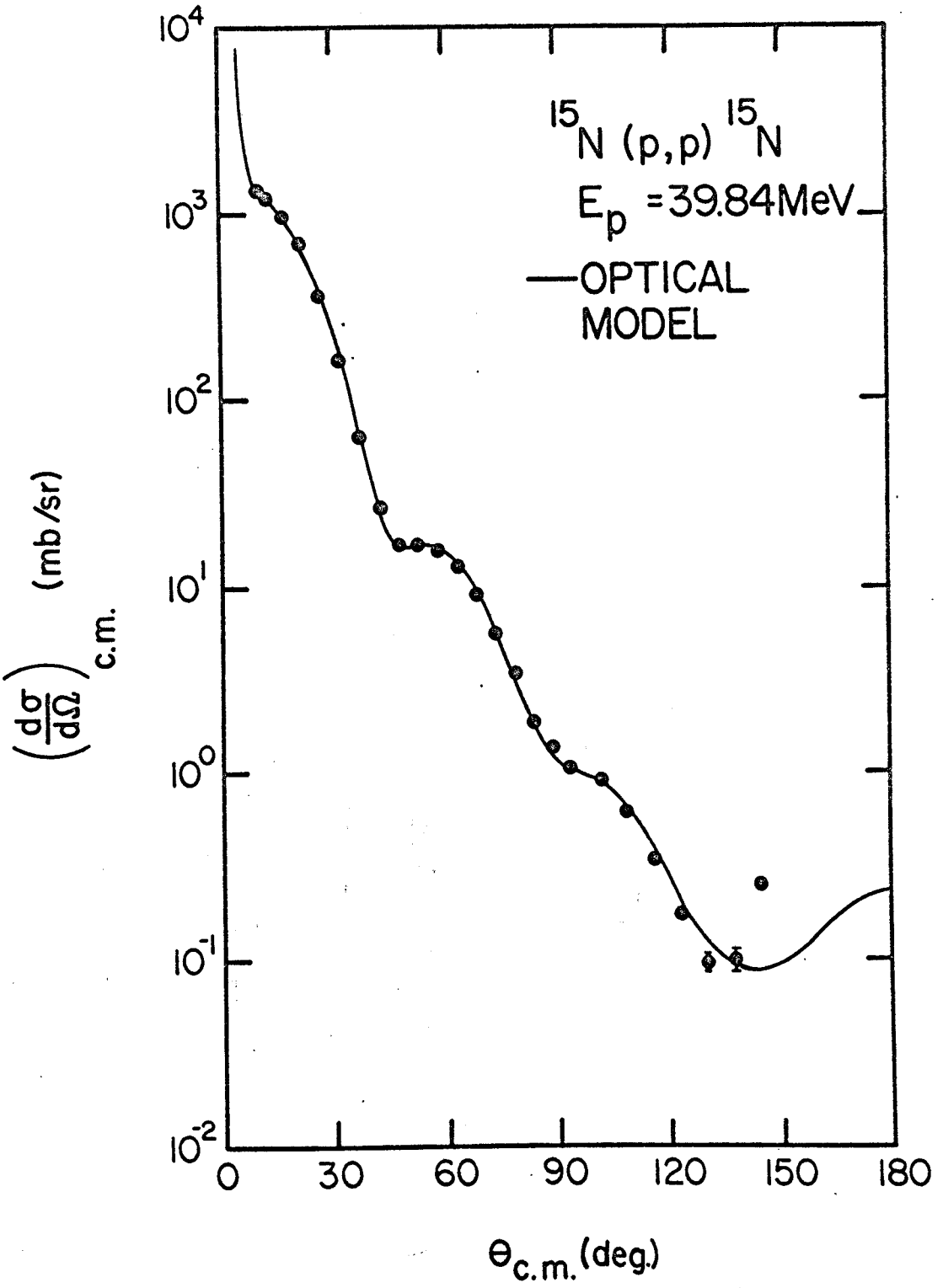

Figure IV-6. Optical model fit to the ^{15}N(p,p)^{15}N angular distribution. The parameters used are listed in Table IV-1.

IV.C. Deuteron Optical Model Parameters

Since it is impossible to measure the elastic scattering of deuterons by the unstable nucleus ^{15}O, data for deuteron scattering by ^{16}O was used. Sets of optical model parameters have been found for deuteron elastic scattering by ^{16}O for incident deuteron energies between 11.8 and 52 MeV (Fi 67, Ng 66, Co 66, Ho 66, Te 64, Ne 67, Du 66). Many studies have been done with lower energy deuterons, but the applicability of the optical model is questionable in these cases. The parameters for this work are based on the 11.8 MeV parameters of Fitz et al. (Fi 67), the 16.8 MeV parameters of Hodgson (Ho 66), the 34.4 MeV parameters of Newman et al. (Ne 67), and the 52 MeV parameters of Duelli et al. (Du 66). Each of these studies used a derivative surface absorption and included spin-orbit effects. These parameters are shown in Fig. IV-7. The solid curves were drawn with the constraint that they pass through the 34.4 MeV points. Very little weight was placed on the 16.8 MeV parameters since they differed significantly from the general trend of the other parameters in several cases.

Since the $^{16}O(p,d)^{15}O$ data covered a wide range of incident proton energies, and since for each incident energy there existed a wide range of Q-values, it was necessary to

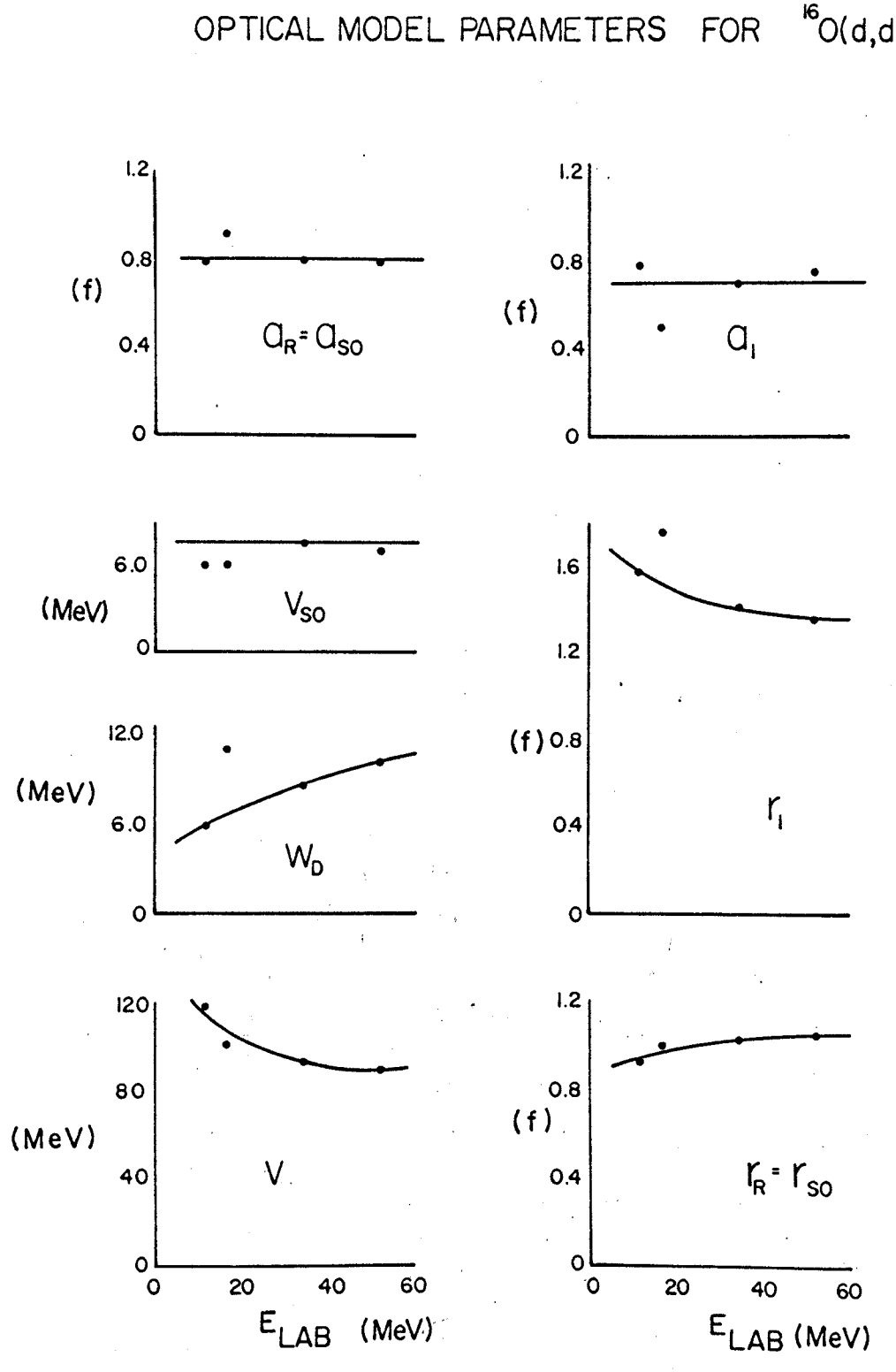

Figure IV-7. Optical model parameters from references quoted in the text describing the elastic scattering of deuterons from ^{16}O between 11.8 and 52 MeV. The curves represent the "best" values of the parameters, from which those used in the DWBA exit channel calculations were taken.

Table IV-2. Deuteron optical parameters used in the DWBA analysis of the $^{16}O(p,d)^{15}O$ and $^{15}N(p,d)^{14}N$ reactions. These are labeled by the laboratory energies of the deuteron and proton and the Q-value of the reaction.

E_d (MeV)	E_p (MeV)	Q (MeV)	V (MeV)	r_R (F)	a_R (F)	W_D (MeV)	r_I (F)	a_I (F)
33.2	45.34	-13.44	92.8	1.03	0.80	8.84	1.41	0.70
32.9	39.84	-8.61	93.5	1.02	0.80	8.70	1.41	0.70
26.2	{45.34 38.63	{-19.62 -13.44}	98.0	1.00	0.80	7.95	1.45	0.70
24.8	39.84	-15.64	98.5	1.00	0.80	7.80	1.46	0.70
19.0	{38.63 31.82	{-19.62 -13.44}	104.0	0.98	0.80	7.05	1.50	0.70
17.2	89.84	-22.33	106.0	0.97	0.80	6.80	1.52	0.70
10.4	{31.82 25.52	{-19.62 -13.44}	114.0	0.95	0.80	6.00	1.57	0.70
4.5	25.52	-19.62	130.0	0.90	0.80	5.00	1.68	0.70

$r_{so} = r_R$, $a_{so} = a_R$, $V_{so} = 7.57$ MeV, $r_{oc} = 1.30$ F.

have deuteron parameters corresponding to incident deuteron energies between 33.2 and 5.1 MeV. These were taken from Fig. IV-7; the ones of major interest (see Chapter VI) are listed in Table IV-2.

For the analysis of the $^{15}N(p,d)^{14}N$ data, optical model parameters for deuteron elastic scattering on ^{14}N at 32.8 MeV and lower were required. Very little data is available in the literature, and that which is available (Ng 66, Vi 66) corresponds to lower deuteron energies and was analyzed using simplified forms of the optical model potential. Thus, it was again decided to use parameters derived from $^{16}O(d,d)^{16}O$ data. Newman et al. (Ne 67) have shown that the variation of the parameters with Z and A is rather slow, so these parameters should be quite valid. Table IV-2 also lists the deuteron parameters used in the $^{15}N(p,d)^{14}N$ analyses.

CHAPTER V

EXPERIMENTAL RESULTS

Deuteron energy spectra and angular distributions are presented in this chapter for the $^{16}O(p,d)^{15}O$ and $^{15}N(p,d)^{14}N$ reactions. Some of the conclusions reached about possible spin and parity assignments are based upon the distorted wave Born approximation (DWBA) calculations discussed in Chapter VI; however, unless otherwise noted, the curves shown with the angular distributions represent only the general trend of the data. The error bars shown in the figures represent the total error in the differential cross section. Those not shown were smaller than the size of the data points.

V.A. $^{16}O(p,d)^{15}O$

V.A.1. Simple Model Predictions

Before discussing the data it would be instructive to determine which levels of ^{15}O should be populated in the $^{16}O(p,d)$ reaction. Considered as a direct reaction, the (p,d) reaction involves the removal of a single neutron from the target nucleus, which is assumed to be in its

ground state. The simple shell model picture of the ^{16}O ground state is shown in Fig. V-1. The single particle energies are given by Jolly (Jo 63) as 0.0, 27.0, 33.0, 44.0, and 45.0 MeV for the $1s_{1/2}$, $1p_{3/2}$, $1p_{1/2}$, $1d_{5/2}$, and $2s_{1/2}$ particles respectively. If the $1p_{1/2}$ neutrons were considered to be barely bound, the $1p_{3/2}$ neutrons would be bound by 6 MeV and the $1s_{1/2}$ neutrons by 33 MeV. Thus, one would expect either a $1p_{1/2}$ or a $1p_{3/2}$ neutron to be picked up; the pickup of a $1s_{1/2}$ neutron would be very unlikely owing to its strong binding. Since the ground state of ^{16}O is known to have $J^{\pi} = 0^{+}$, conservation of angular momentum and parity require the spin and parity of the final state to be that of the picked-up neutron, i.e., $1/2^{-}$ or $3/2^{-}$. The simplest shell model picture of ^{15}O is that of a single neutron hole in the ^{16}O core. These are also shown in Fig. V-1. On the basis of these simple pictures one would expect the deuteron energy spectra to contain one $1/2^{-}$ peak, one $3/2^{-}$ peak, and no others.

It is known, however, that the simple shell model is much too naive, even for the case of a "closed" shell nucleus such as ^{16}O. One should consider the effects of low-lying deformed states in the closed shell nucleus (M9 56, En 65, Br 66a, Br 66b) when using that nucleus as

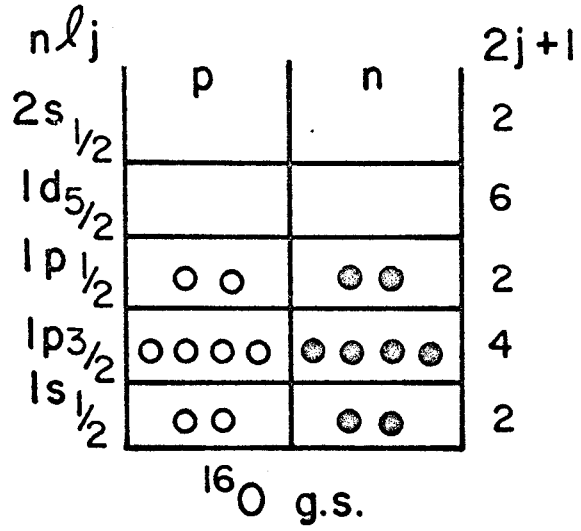

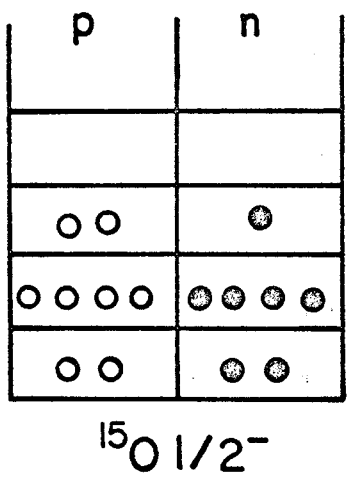

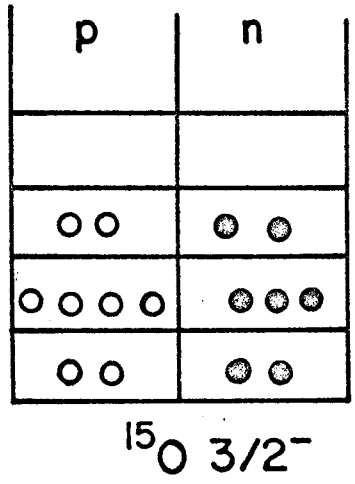

Figure V-1. Simple shell model configurations of the ^{16}O ground state and the ^{15}O $1/2^-$ and $3/2^-$ states. The value 2j+1 is the number of protons or neutrons required to fill a given nℓj subshell.

a core. Such effects are known as core polarization. Brown and Shukla (Br 67) have performed such calculations for ^{15}O and ^{15}N. They predict, in addition to the strong 0.0 MeV, $1/2^-$ and 6.18 MeV, $3/2^-$ levels, the existence of a $3/2^-$ level between 10.0 and 11.0 MeV of excitation and a $1/2^-$ level approximately 1.0 MeV lower. Bertsch (Be 68) has predicted that core polarization could result in many highly fragmented states with excitation energies of approximately 20 MeV. Hence, core polarization can result in the sharing of the $1p_{1/2}$ and $1p_{3/2}$ strengths among several states. One would also expect the ^{16}O ground state to be more complex. Calculations have been performed (Br 66a) in which 2 particle-2 hole and 4 particle-4 hole admixtures have been considered. If such admixtures existed, one would expect to pickup some $1d_{5/2}$ and $2s_{1/2}$ neutrons, leading to positive parity levels in ^{15}O.

V.A.2. Energy Spectra

Fig. V-2 shows an energy level diagram of the ^{15}O nucleus beside which has been placed a deuteron spectrum taken at a laboratory angle of 20.1° with 45.34 MeV incident protons. All of the known levels below 11 MeV are shown. All energies, spins, and parities for the levels below 9 MeV were taken from the gamma-ray work of Warburton et al. (Wa 65), those of the levels between

9 and 10 MeV from the work of Lambert and Durand (La 67), and those of levels above 10 MeV from Lauritsen and Ajzenberg-Selove (La 62). One immediately notices the presence of the two very strong peaks corresponding to $1p_{1/2}$ and $1p_{3/2}$ neutron pickup. All other states excited are much weaker. It is interesting to note here the surprisingly good agreement with the simplest shell model picture discussed in the preceding section.

Additional deuteron energy spectra obtained for incident protons of energies 45.34, 38.63, 31.82, and 25.52 MeV are shown in Figs. V-3--V-5. The Goulding particle identification system was used in obtaining each of these spectra. Fig. V-6 shows a spectrum obtained using the time-of-flight system for mass identification. The peaks corresponding to ^{14}N levels are due to ^{3}He particles from the $^{16}O(p,^{3}He)^{14}N$ reaction which reached the detector within the accepted time window. The closely spaced levels near 5.2 and 6.8 MeV are partially resolved here. The other spectra obtained between 12.4° and 30° in the laboratory frame using time-of-flight showed comparable resolution. This data will be discussed in Section V.A.4. A tabulation of the peak cross sections for the levels excited is contained in Table VI-3.

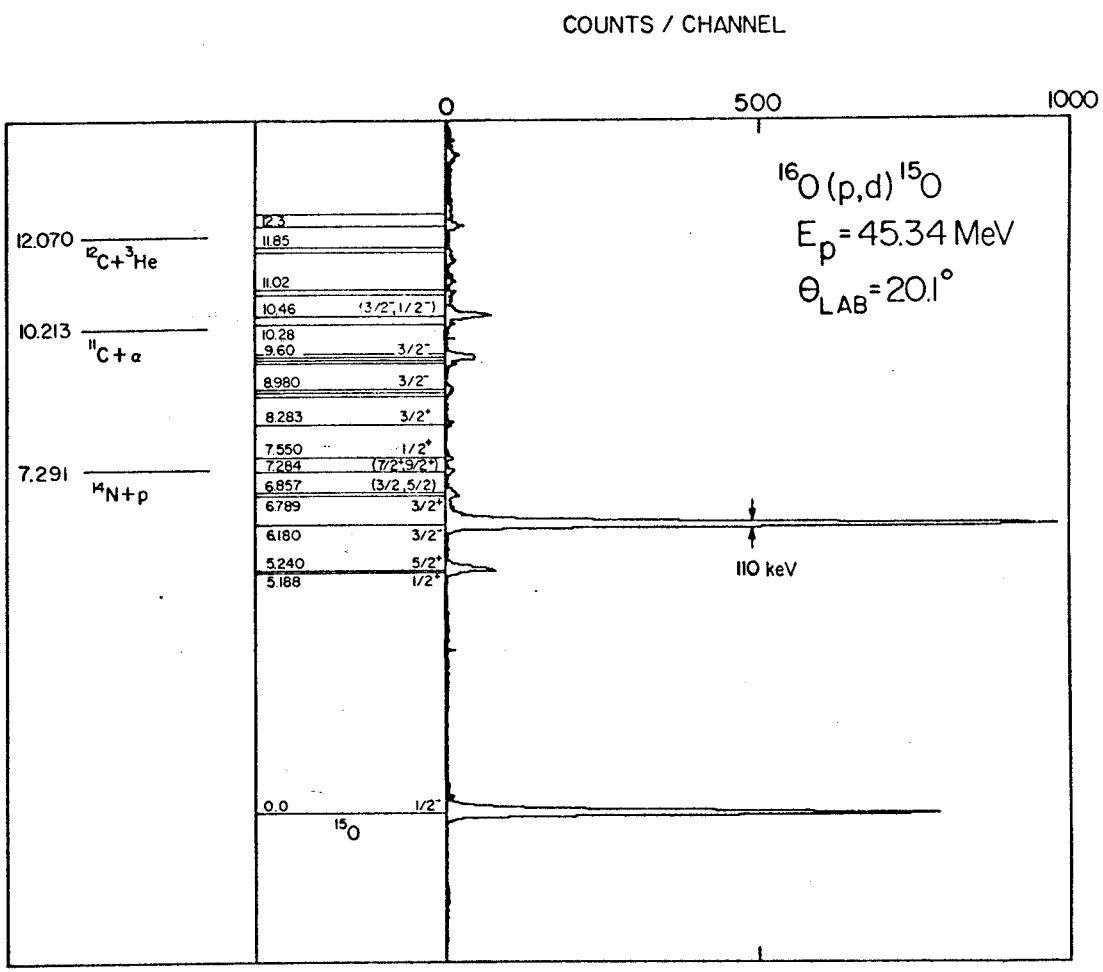

Figure V-2. Energy level diagram of ^{15}O displayed beside a deuteron energy spectrum from the $^{16}O(p,d)^{15}O$ reaction for E_p=45.34 MeV and θ_{LAB}=20.1°. The two strongly excited levels are those predicted in the simple shell model picture.

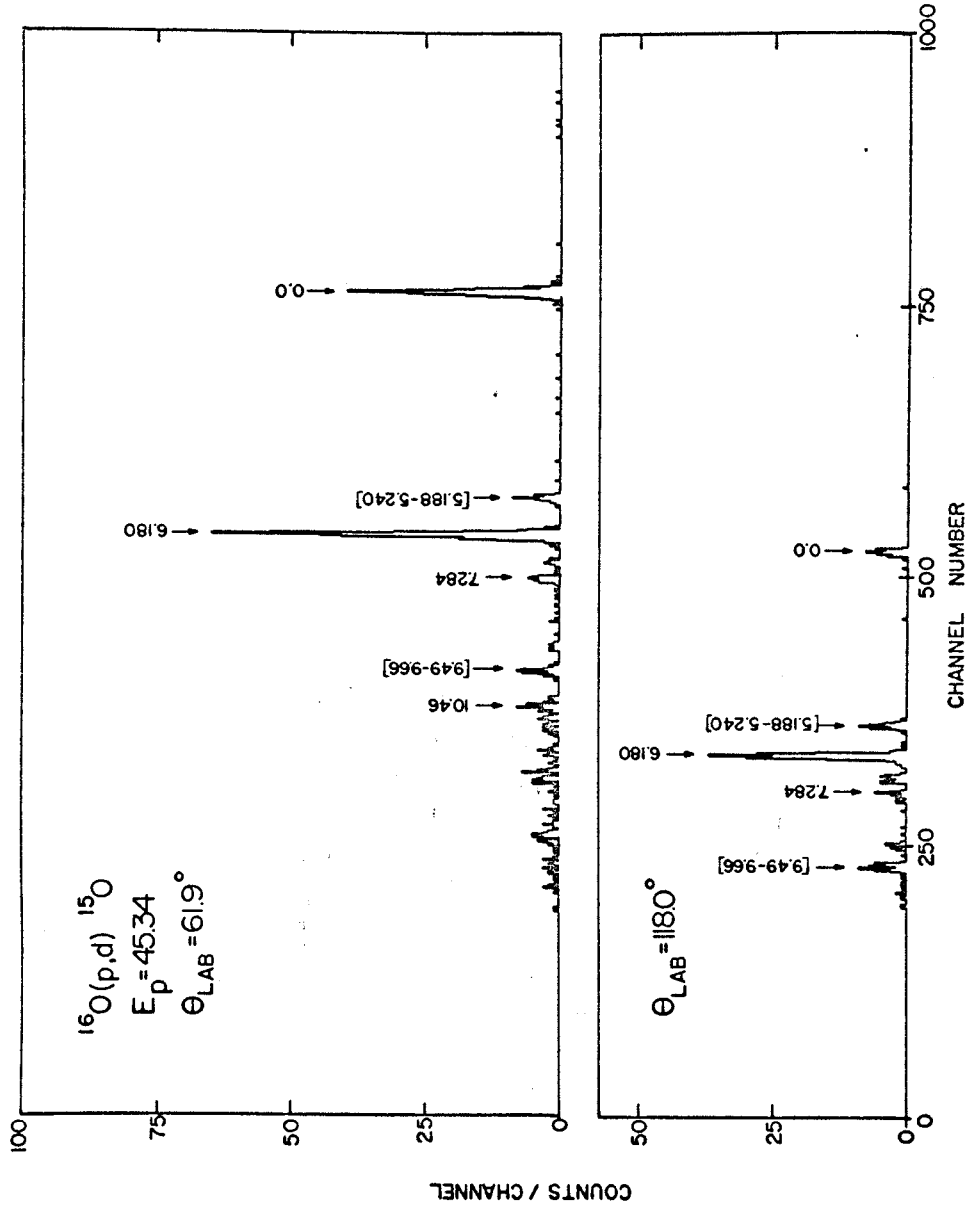

Figure V-3. Deuteron energy spectra at θ_{LAB}=61.9° and 118.0° from the $^{16}O(p,d)^{15}O$ reaction for E_p=45.34 MeV.

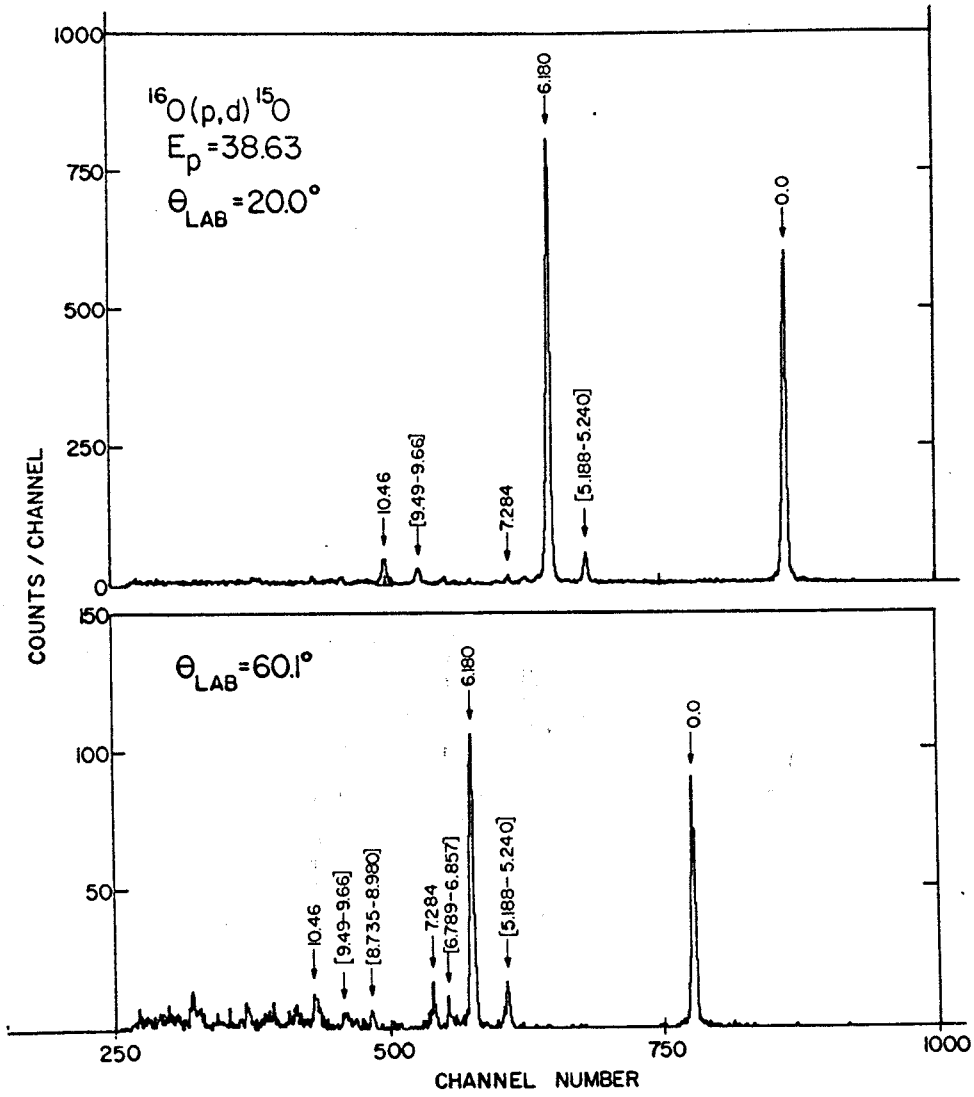

Figure V-4. Deuteron energy spectra at θ_{LAB}=20.0° and 60.1° from the $^{16}O(p,d)^{15}O$ reaction for E_p=38.63 MeV.

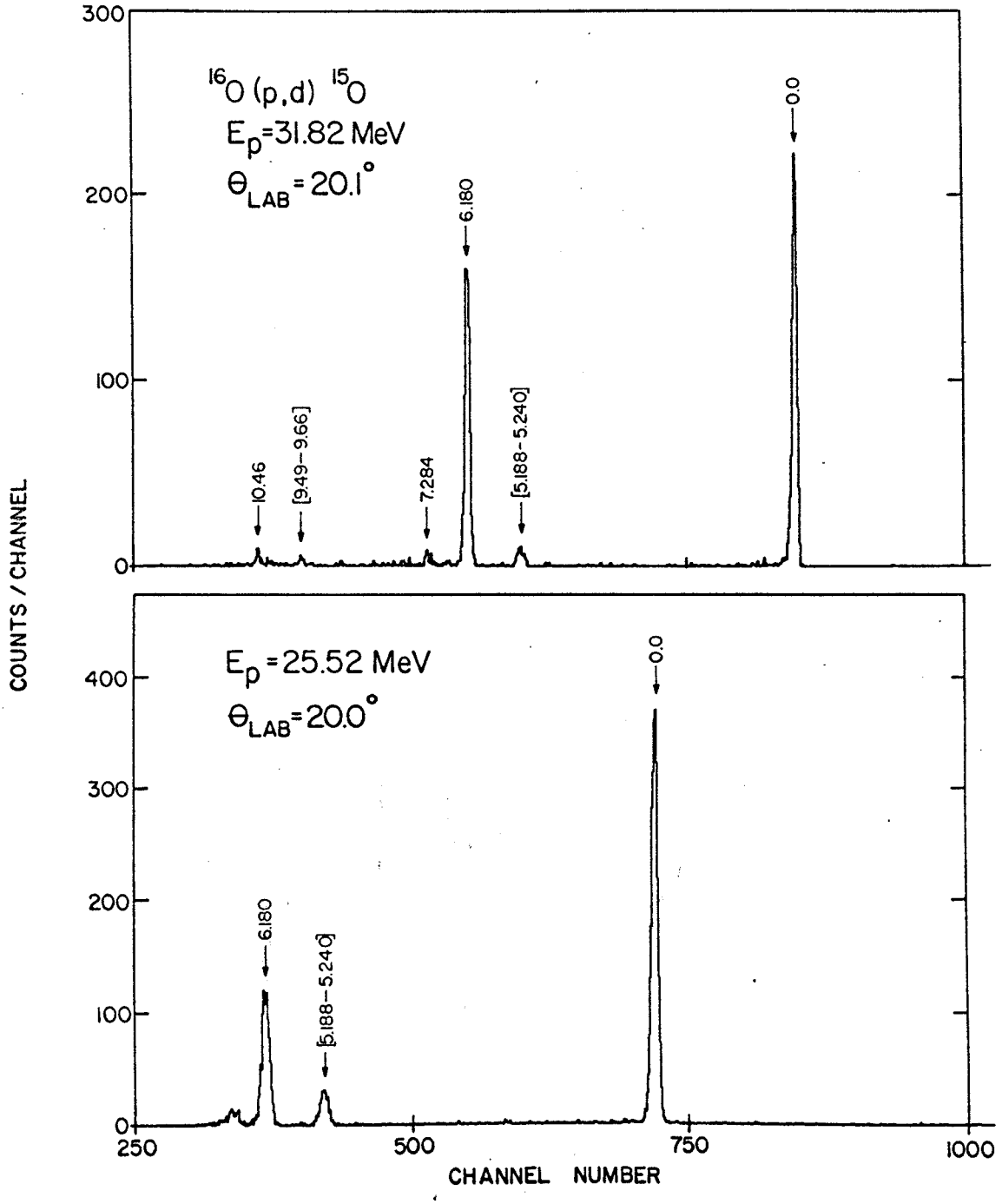

Figure V-5. Deuteron energy spectra at θ_{LAB}=20.1° and 20.0° from the $^{16}O(p,d)^{15}O$ reactions at E_p=31.82 and 25.52 MeV, respectively.

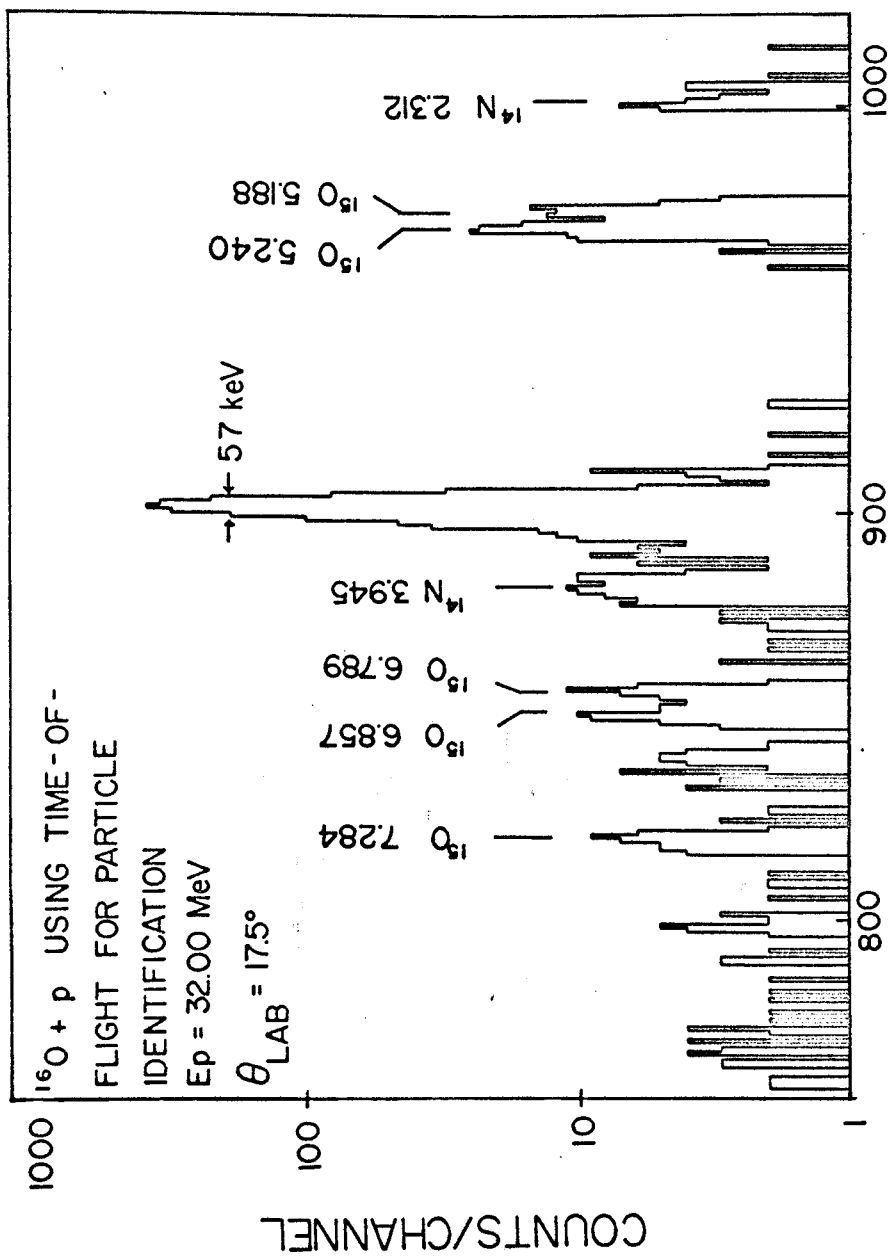

Figure V-6. High resolution energy spectrum of reaction products at θ_{LAB}=17.5° for 32.00 MeV protons incident on ^{16}O, obtained by the use of time-of-flight techniques for particle identification. The ^{14}N peaks are due to deuterons from the $^{16}O(p,^{3}He)^{14}N$ reaction which reached the counter during the accepted time window.

V.A.3. Negative Parity Levels

Below an excitation energy of 16.5 MeV the existence of one $1/2^-$ and three $3/2^-$ levels have been confirmed (Wa 65, La 67, La 62). The $1/2^-$ level at 0.0 MeV and the $3/2^-$ level at 6.180 MeV are those predicted by the simplest shell model. Angular distributions measured for these states are shown in Figs. V-7 and V-8. The existence of a first maximum between 10° and 20° in the center-of-mass frame is characteristic of $\ell_n=1$ pickup. The angle at which the first maximum occurs decreases as the incident proton energy increases. J-dependence in this reaction exhibits itself in the generally steeper slope and more pronounced oscillation of the $J^\pi=1/2^-$ data.

The magnitude of the differential cross section at the first $\ell_n=1$ maximum is used in the extraction of spectroscopic factors (see Chapters II and VI). This quantity is shown as a function of the incident proton energy in Fig. V-9. Included in this figure are points from other studies of the $^{16}O(p,d)^{15}O$ reaction between 18.5 and 100 MeV (Ch 67, Ko 67a, Le 67, Le 63, Sh 67). The dashed curves are drawn to accentuate the general trend of the data. The $3/2^-$ peak cross section becomes larger than the $1/2^-$ peak cross section at some point between 45 and 100 MeV. At 100 MeV it is interesting to note that the ratio of the $3/2^-$ to the $1/2^-$ cross section is $\sim$1.3.

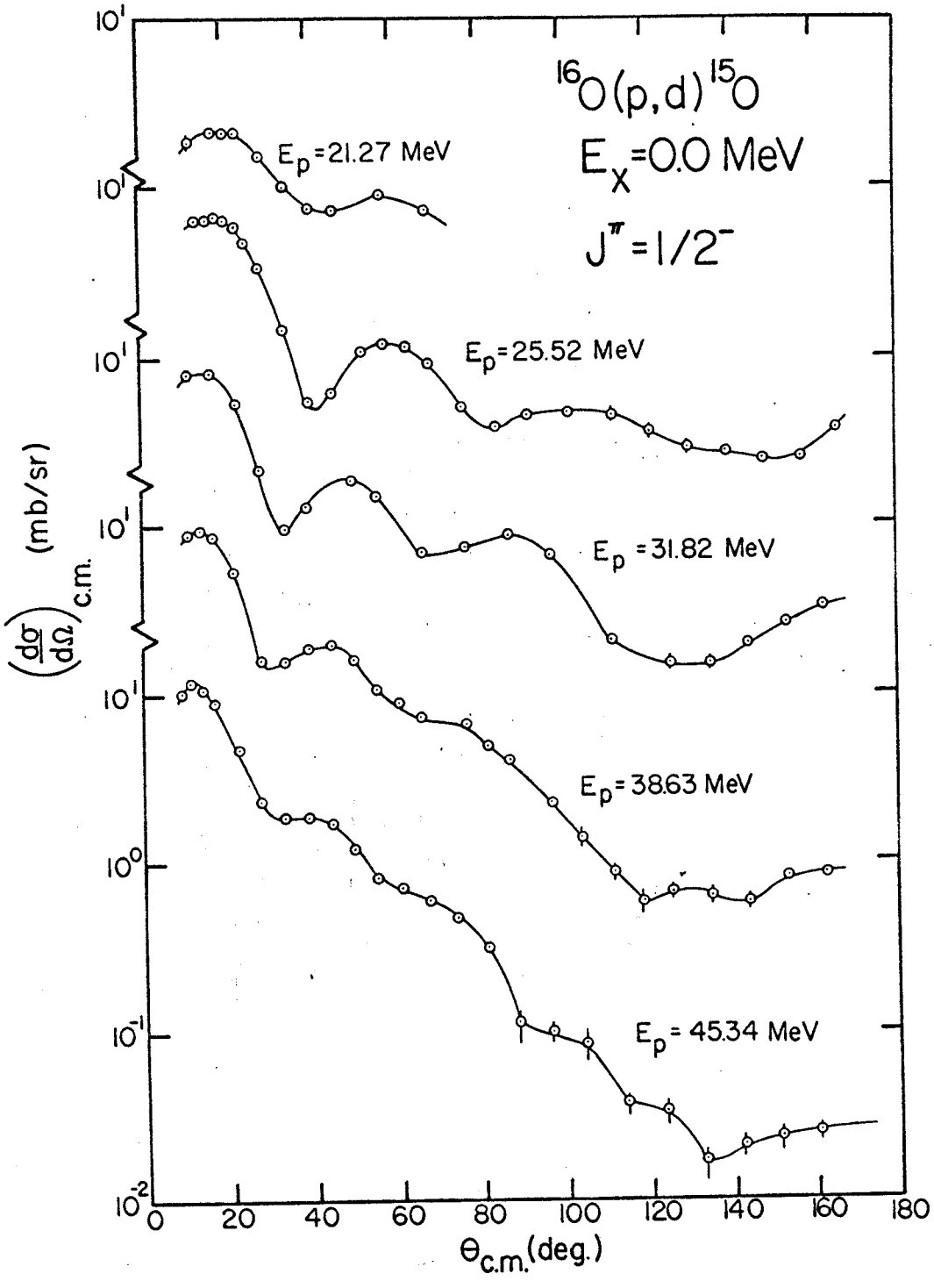

Figure V-7. Deuteron angular distributions for the 0.0 MeV, $1/2^-$ level of ^{15}O from the $^{16}O(p,d)^{15}O$ reaction for incident proton energies between 21.27 and 45.34 MeV.

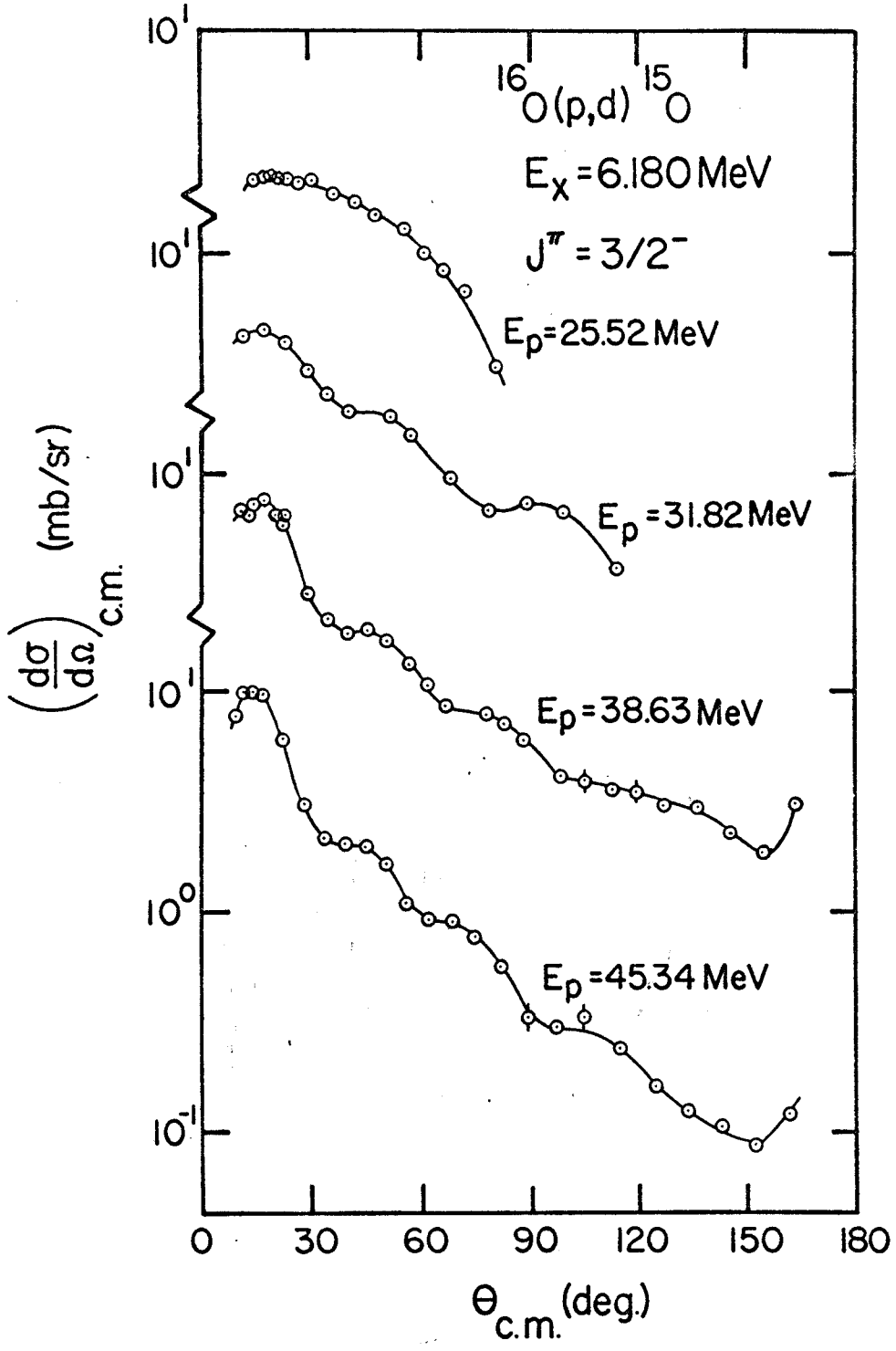

Figure V-8. Deuteron angular distributions for the 6.180 MeV, $3/2^-$ level of ^{15}O from the $^{16}O(p,d)^{15}O$ reaction for incident proton energies between 25.52 and 45.34 MeV.

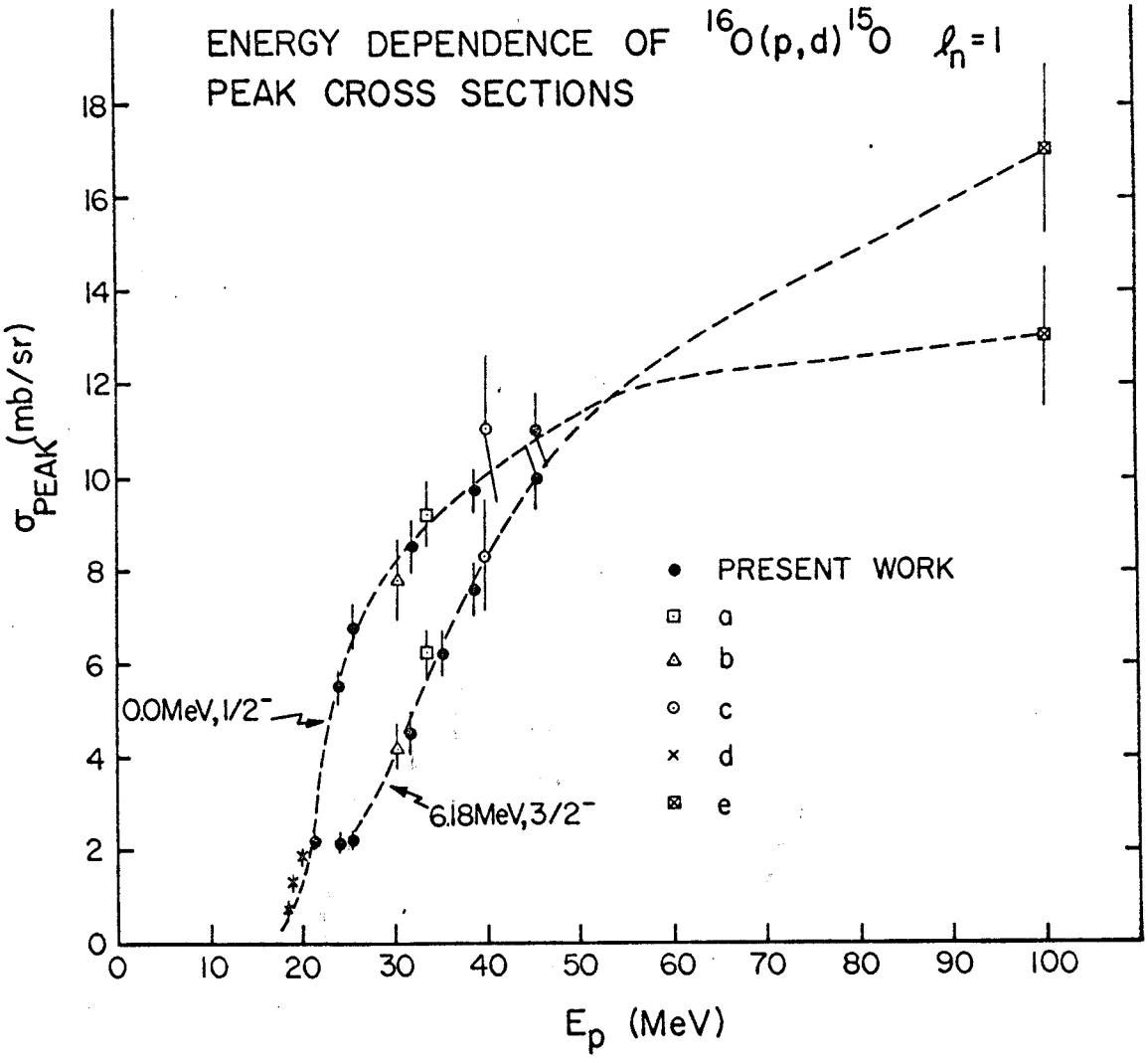

Figure V-9. Dependence of the ℓ_n=1 peak cross section of the 0.0 MeV, $1/2^-$ and 6.180 MeV, $3/2^-$ levels of ^{15}O from the $^{16}O(p,d)^{15}O$ reaction on the incident proton energy. The data represented by symbols a--e are found in Refs. Ko 67a, Ch 67, Sh 66, Le 63, and Le 67, respectively.

In an attempt to explain the phase of the E2/M1 mixing ratio for the (6.18 MeV, $3/2^-$ → 0.0 MeV, $1/2^-$) transition in ^{15}O, Rose and Lopes (Ro 65, Lo 66) proposed that only 40% of the $1p_{3/2}$ hole strength was contained in the 6.18 MeV state, and that much of the remaining strength was contained in the 8.98 MeV level. However, $^{16}O(p,d)^{15}O$ data (Ba 64) and $^{16}O(^3He, \alpha)^{15}O$ data (Wa 65a) indicated that there was no appreciable ($\leq$10%) $1p_{3/2}$ component at excitation energies between 6.5 and 13 MeV. The deuteron energy spectra in Figs. V-2--V-5 indicate that the excitation of the 8.98 MeV level is very weak, the peak cross section being less than 0.1 mb/sr. However, there are two relatively strong deuteron groups corresponding to levels of higher excitation energy. The first corresponds to the levels at 9.49, 9.53, 9.60, and 9.66 MeV, which have $J^\pi = 5/2^-$, $1/2^+$, $3/2^-$, and $(7/2, 9/2)^-$ respectively (La 67). Careful examination of the energy spectra showed that all four levels were excited, but that approximately 70% of the area of the peak was due to excitation of the 9.60 MeV, $3/2^-$ level. The other deuteron group comes from the excitation of the 10.46 MeV level, which was resolved from the 10.28 MeV level. Angular distributions for these levels are shown in Fig. V-10. The angular distribution labeled 9.60 contains contributions from the other three close-lying levels. The curves represent

empirical ℓ_n=1 shapes corresponding to the Q-values of the reactions leading to these states, obtained by graphical interpolation between the shapes of the 0.0 and 6.18 MeV angular distributions for 45.34 and 38.63 MeV incident protons. Both levels are seen to be ℓ_n=1 in character. On the basis of shape, the assignment of $3/2^-$ to the 10.46 MeV level is preferred. The data certainly do not disagree with the previous $3/2^-$ assignment for the 9.60 MeV level. Estimates of the $1p_{3/2}$ hole strength in these levels will be given in Chapter VI, where spectroscopic factors will be discussed.

V.A.4. Positive Parity Levels

As was noted in Section V.A.1., the only way in which a positive parity level can be reached in ^{15}O by the direct pick-up of a neutron from ^{16}O is for the ^{16}O ground state to contain an admixture of even-ℓ neutrons. The most likely admixtures being $1d_{5/2}$ and $2s_{1/2}$ neutrons, one would look for $5/2^+$ and $1/2^+$ levels. The levels at 5.188, 7.550, 8.735, and 9.53 have previously been shown to be $1/2^+$. The level at 5.240 MeV has an assignment of $5/2^+$, and the (3/2, 5/2) level at 6.857 MeV appears to be the mirror level of the 7.15 MeV, $5/2^+$ level in ^{15}N.

Examination of Figs. V-2--V-6 shows that the 5.188-5.240 MeV doublet has considerable strength. Angular distributions

for the unresolved doublet are shown in Fig. V-11. The time-of-flight data taken with 32.00 MeV incident protons had sufficient resolution to allow a Gaussian peakshape analysis to be performed to separate the states. Using a non-linear least squares method, a skewed Gaussian was fitted to the single 6.18 MeV level to determine a peak shape. Then the areas and centroids of two Gaussians having this shape were adjusted, keeping a fixed separation corresponding to the known separation of the levels, until the fit to the 5.188-5.240 MeV group was judged best. The ratios of the areas were applied to the 31.82 MeV data to obtain partial angular distributions, also shown in Fig. V-11. The large errors ($\sim$30%) are due to the poor statistics of the data and the uncertainty in the ratios of the areas. The shape of the 5.188 MeV angular distribution is characteristic of ℓ_n=0 pickup, whereas the occurrence of the first maximum near 30° for the 5.240 MeV angular distribution indicates an $\ell_n \geq 2$, consistent with the $5/2^+$ assignment. This data disagrees with the $^{16}O(d,t)^{15}O$ data of the Rochester group (quoted in Wo 68), which showed no direct reaction pattern for the $1/2^+$ member of the doublet.

Excitations of the other $1/2^+$ and $5/2^+$ levels are very weak, with the exception of the 7.550 MeV, $1/2^+$ level, which does not exhibit the characteristics of ℓ_n=0 pickup

(Fig. V-13). Wong (Wo68) in a study of centroids and sums of direct reaction strengths with ^{16}O as a target, has found that central force (e.g., Rosenfeld, Soper) calculations imply that most of the $1d_{5/2}$ strength is in the 5.24 MeV level, whereas calculations using realistic forces (e.g., Brueckner-Gamel-Thaler, Hamada-Johnston) imply that the dominant part of the $1d_{5/2}$ strength will be in a higher $5/2^+$ state. Thus, the present data tend to support the use of central forces.

Weak excitation of the $3/2^+$ levels at 6.789 and 8.283 MeV has been found, which could be due to the pickup of a $1d_{3/2}$ neutron. The shapes of the angular distributions (Fig. V-13) are not inconsistent with such a pickup. A very interesting angular distribution was measured for the level at 7.284 MeV, which had been assigned a spin of $\leq 9/2$ and appears to be the mirror level of the 7.56 MeV, $7/2^+$ level of ^{15}N. If it were excited by a direct reaction, it would correspond to the pickup of a $1g_{7/2}$ neutron. The angular distribution for this level obtained with 45.34 MeV incident protons is shown in Fig. V-12. The curves are DWBA calculations with and without a lower integration cutoff (to be discussed in Chapter VI). The $\ell_n=4$ shape fits the data well. An alternative process for the excitation of this level is a two-step one in which the 6.13 MeV, 3^- level of ^{16}O is first excited, with the pickup of a 1p neutron

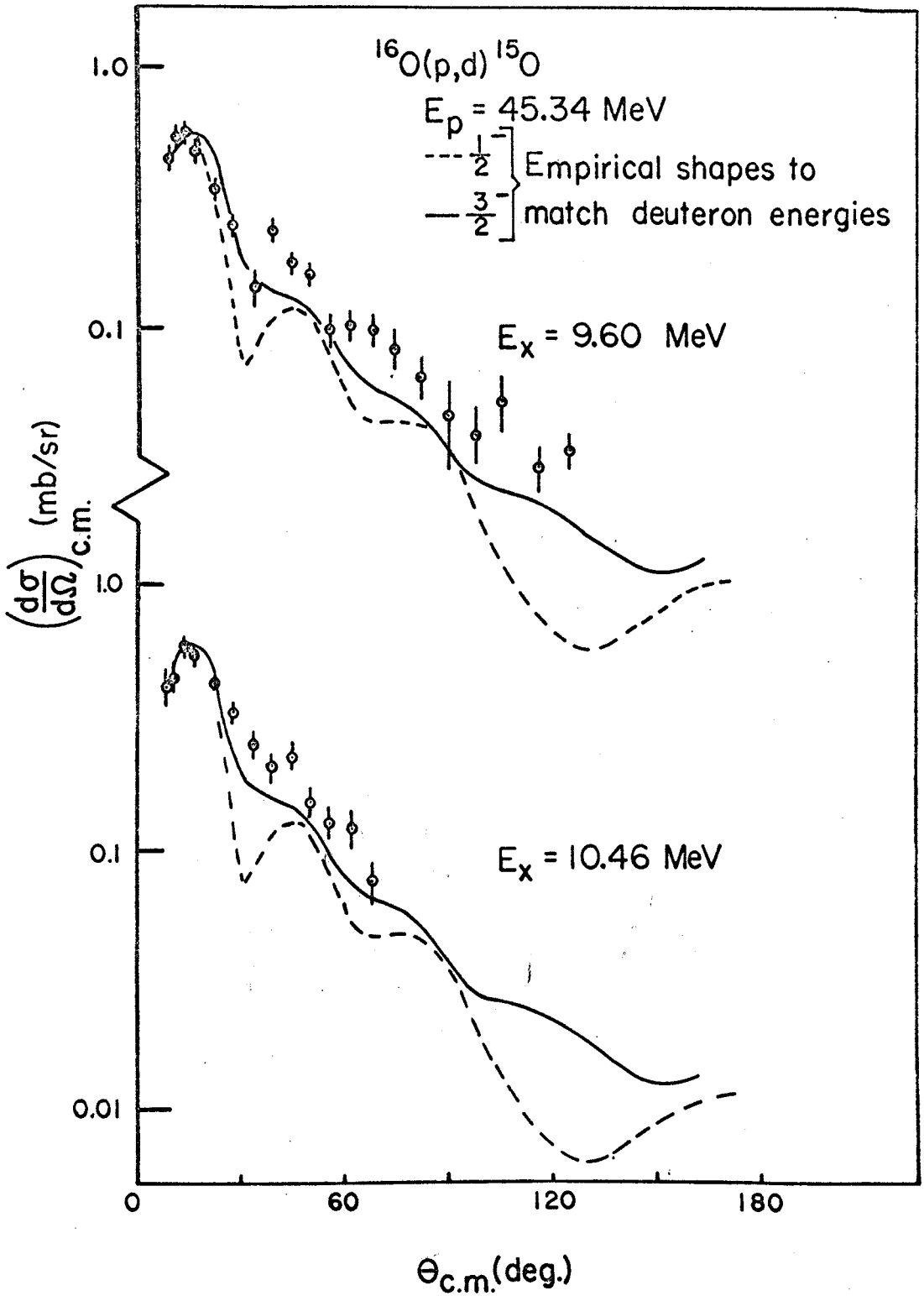

Figure V-10. Deuteron angular distributions for the 9.60 and 10.46 MeV levels of ^{15}O from the $^{16}O(p,d)^{15}O$ reaction for E_p=45.34 MeV. The contributions of the 9.49, 9.53, and 9.66 MeV levels have not been separated from the 9.60 MeV angular distribution. The curves were obtained empirically from the 45.34 and 38.63 MeV data.

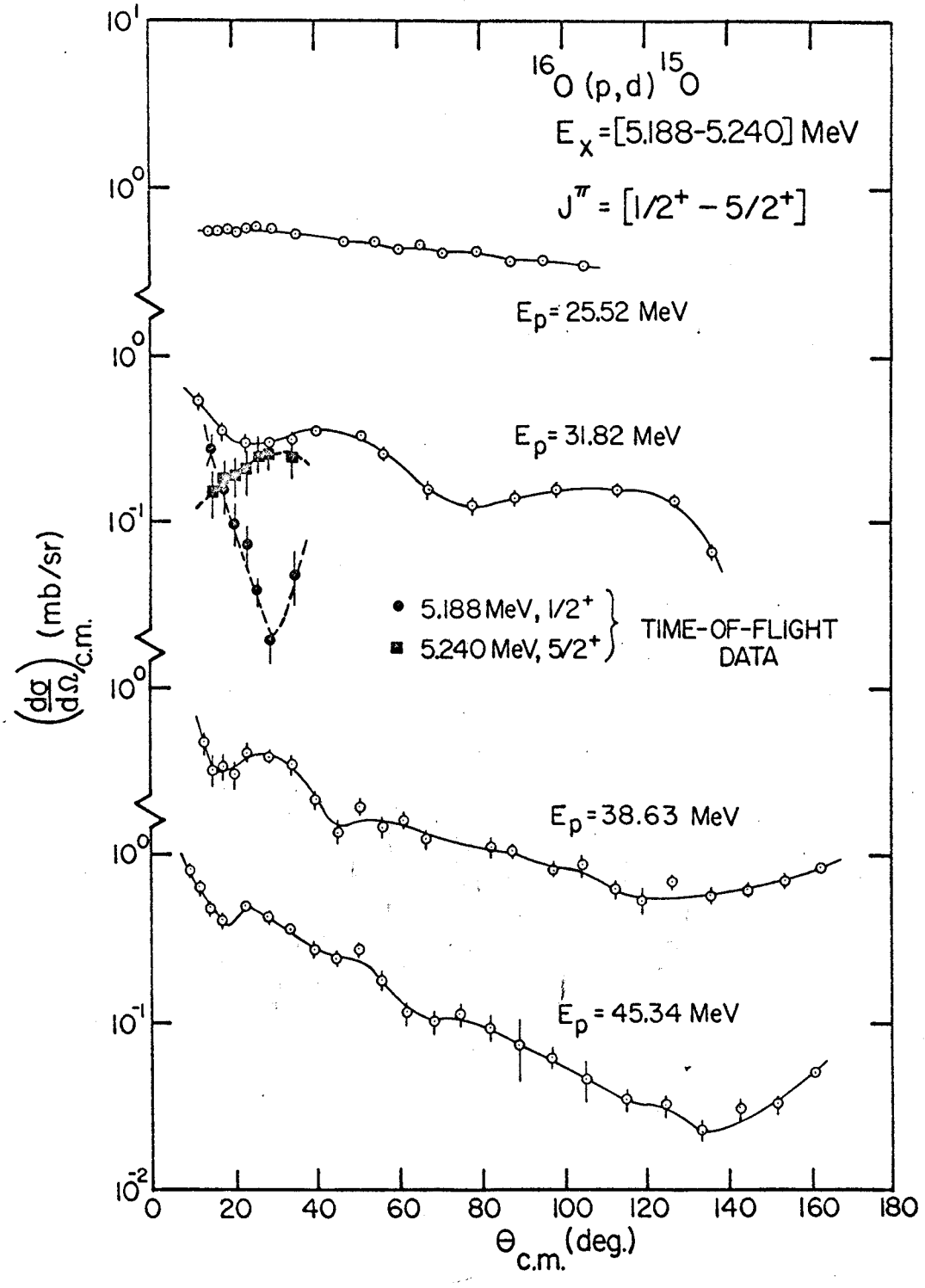

Figure V-11. Deuteron angular distributions for the 5.188-5.240 MeV doublet of ^{15}O from the $^{16}O(p,d)^{15}O$ reaction for incident proton energies between 25.52 and 45.34 MeV. The solid symbols represent a decomposition of the 31.82 MeV angular distribution based on a Gaussian peakshape analysis of the time-of-flight data.

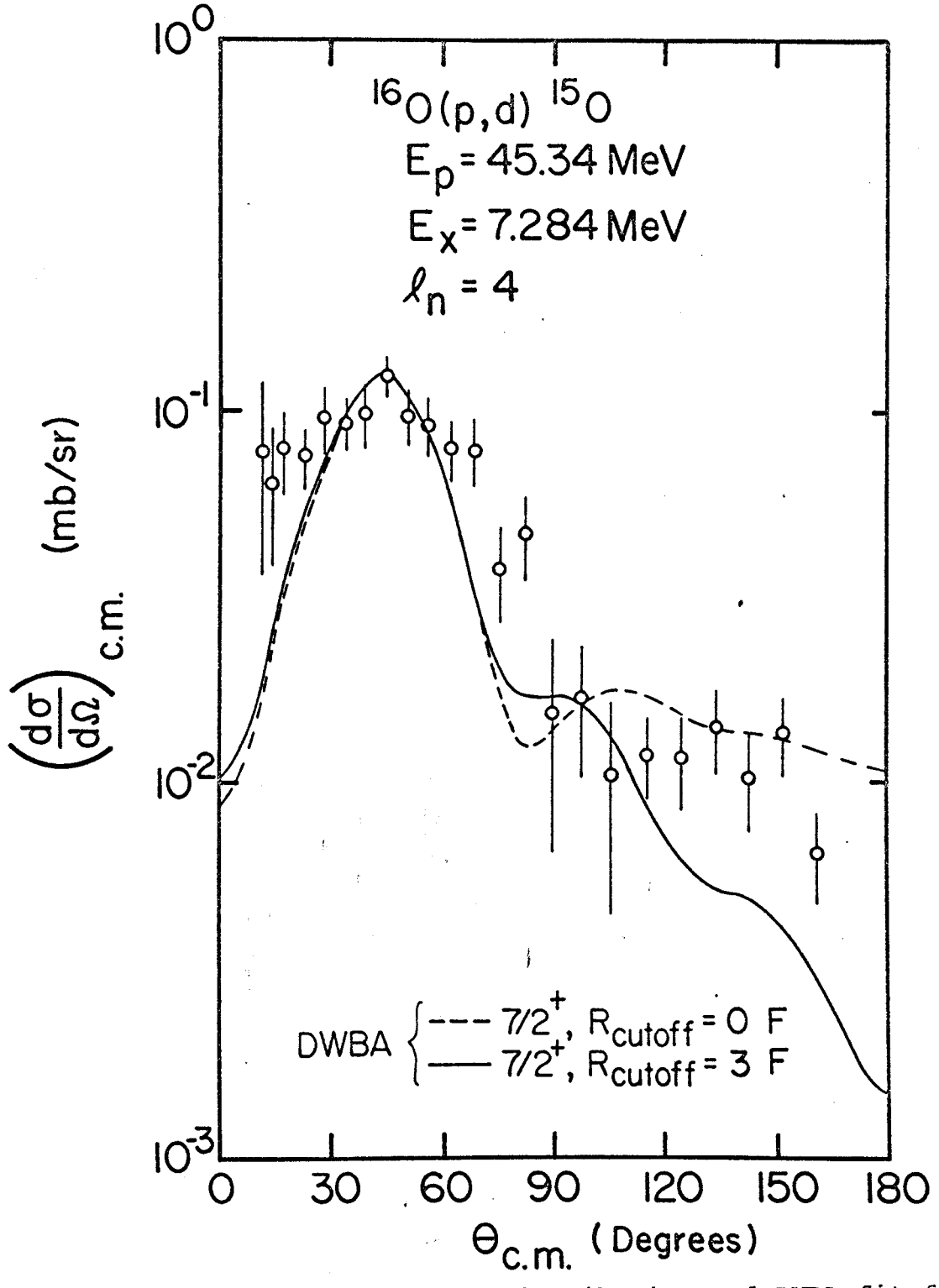

Figure V-12. Deuteron angular distribution and DWBA fit for the 7.284 MeV, $(7/2^+)$ level of ^{15}O from the $^{16}O(p,d)^{15}O$ reaction for E_p=45.34 MeV.

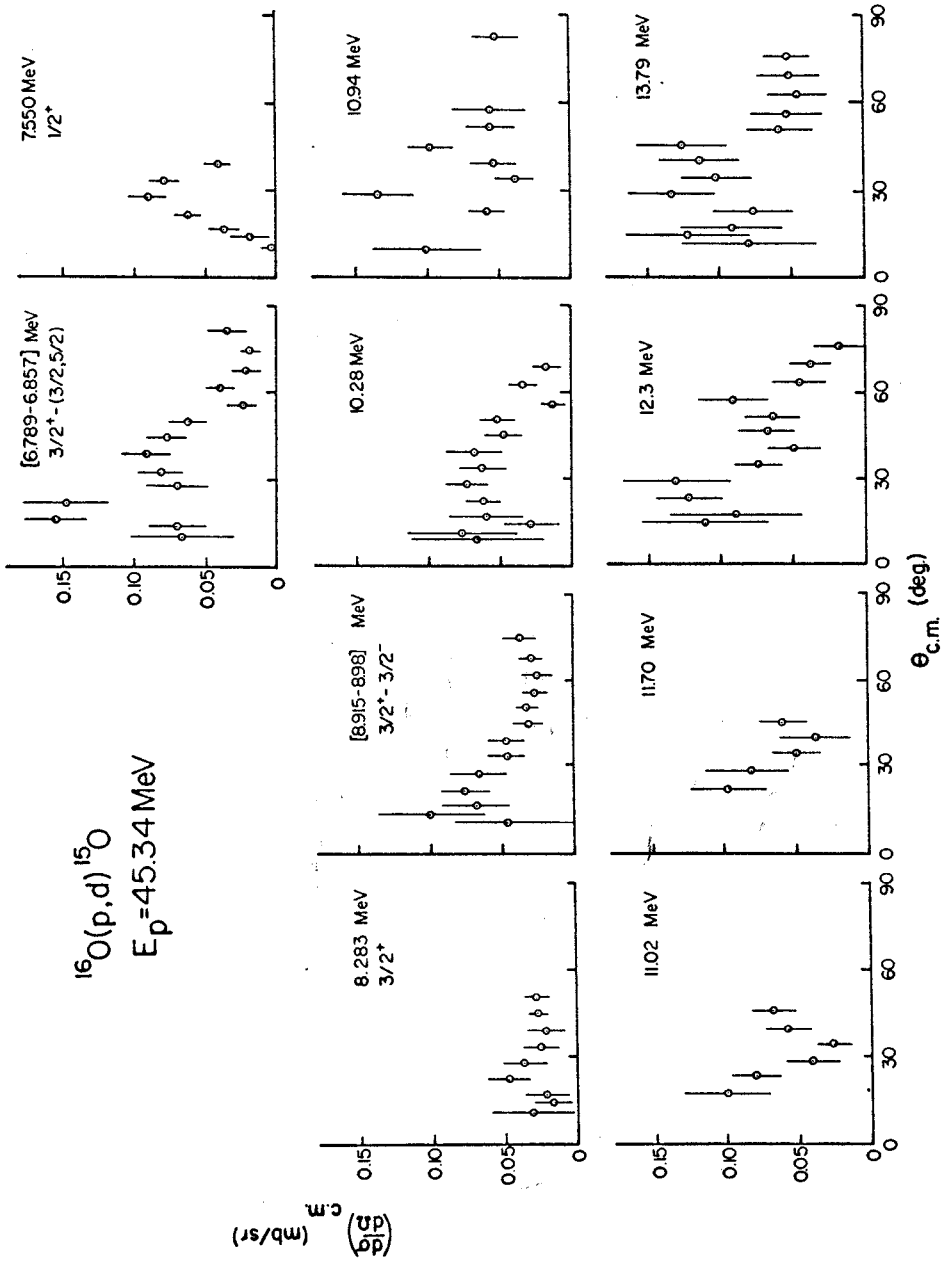

Figure V-13. Deuteron angular distributions for other levels excited in ^{15}O from the $^{16}O(p,d)^{15}O$ reaction at E_p=45.34 MeV. Spins and parities indicated were obtained from references quoted in the text.

(probably a $1p_{1/2}$ neutron) following. Evidence for such a process has been found in the $^{12}C(d,^3He)^{11}B^*(6.67, 7/2^-)$ reaction (Du 68). A $5/2^+$ level could also be excited by the pickup of a $1p_{3/2}$ neutron in a two-step process. The other angular distributions shown in Fig. V-13 exhibit little character. However, the 12.30 and 13.79 MeV levels are quite strong (0.12 mb/sr).

V.B. $^{15}N(p,d)^{14}N$

V.B.1. Simple Model Predictions and Energy Spectra

The simplest shell model configuration for the ^{15}N ground state is that of one $1p_{1/2}$ proton hole in a ^{16}O core. Thus, the neutron configuration is the same as that of ^{16}O. The spin and parity of the ^{15}N ground state is $1/2^-$, so the pickup of a $1p_{1/2}$ neutron populates ^{14}N states having $J^\pi = 0^+, 1^+$, and the pickup of a $1p_{3/2}$ neutron leads to states having $J^\pi = 1^+, 2^+$. Based upon the simplest shell model, using only 1p nucleons, one can construct the ^{14}N configurations shown in Fig. V-14. The isotopic spin quantum number (T) is good for all of the states shown. The particular combinations of the two terms of (c) were necessary in order that T be good. The T=1 states are those in which a neutron could be transformed into a proton, or vice versa, without violating the Pauli

principle. There are nine levels which could be reached by 1p pickup from ^{15}N, the population of the 3^+ level being forbidden by angular momentum conservation. The three other levels having configuration ($_b$) are not populated in the simplest model since they require the excitation of one of the protons in ^{15}N. Thus, one would expect to see six strong levels (one 0^+, T=1; two 1^+, T=0; one 1^+, T-1; one 2^+, T=0; and one 2^+, T=1) whose relative strengths are discussed later.

There are over fifty known levels in ^{14}N between 0.0 and 14.0 MeV, sixteen of which have been identified as 0^+, 1^+, or 2^+. All energies, spins, and parities have been taken from (Za 67) and the references therein. An energy level diagram of ^{14}N, displayed beside a deuteron energy spectrum obtained at $\theta_{LAB}=20°$ for an incident proton energy of 39.84 MeV, is shown in Fig. V-15. It is seen that many levels are excited to some extent. However, the strongly excited levels are seen to be either 0^+, 1^+, or 2^+ (the assignment for the 13.72 MeV level coming from the present work). Other deuteron energy spectra obtained at $\theta_{LAB}=59.8°$ and 119.6° are presented in Fig. V-16.

V.B.2. Levels Reached by $\ell_n=1$ Pickup

Six of the sixteen levels which could be reached by 1p neutron pickup had peak cross sections of 40 μb/sr or

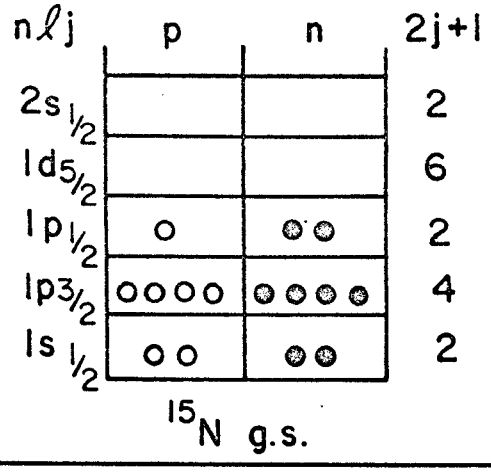

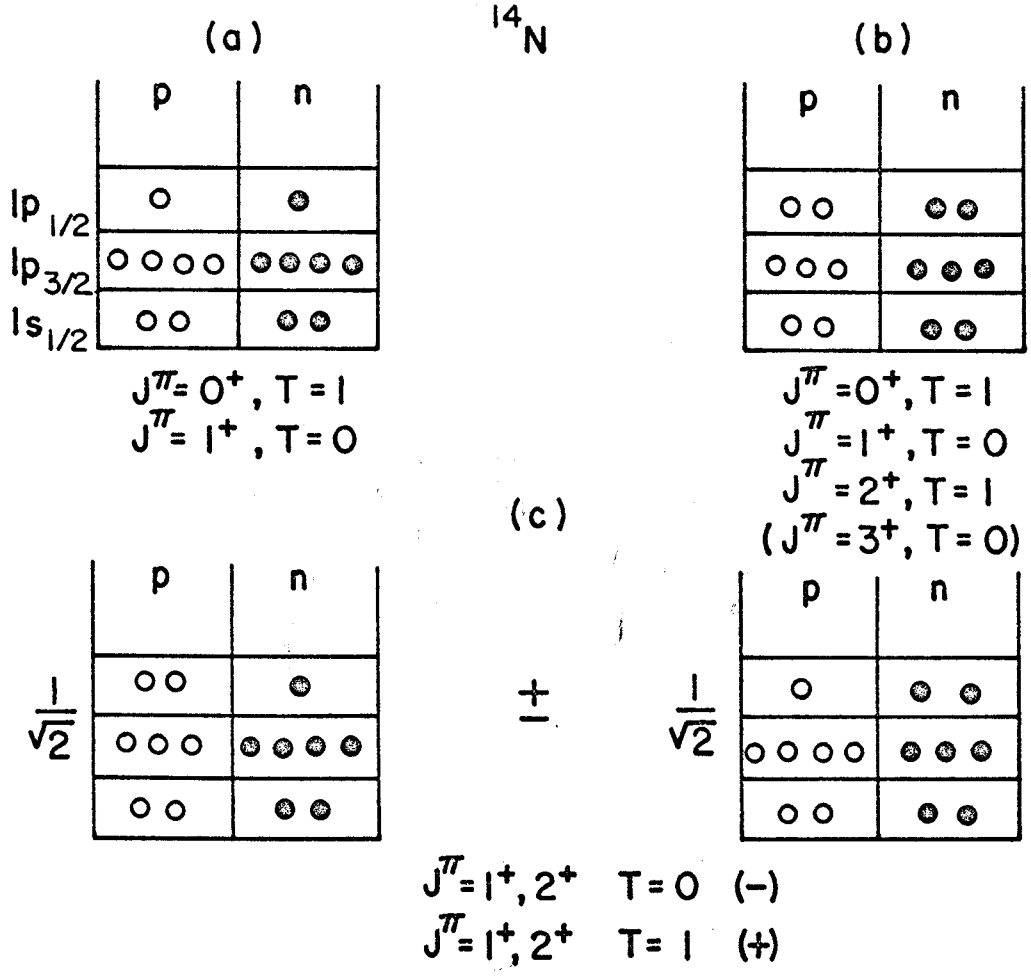

Figure V-14. Simple shell model configurations of the ^{15}N ground state and the ^{14}N levels based only on 1s-1p nucleons. The $J^{\pi}=3^{+}$ level cannot be reached by 1p neutron pickup because of angular momentum conservation. The other levels of configuration (b) will not be reached by the direct pickup of a 1p neutron from ^{15}N.

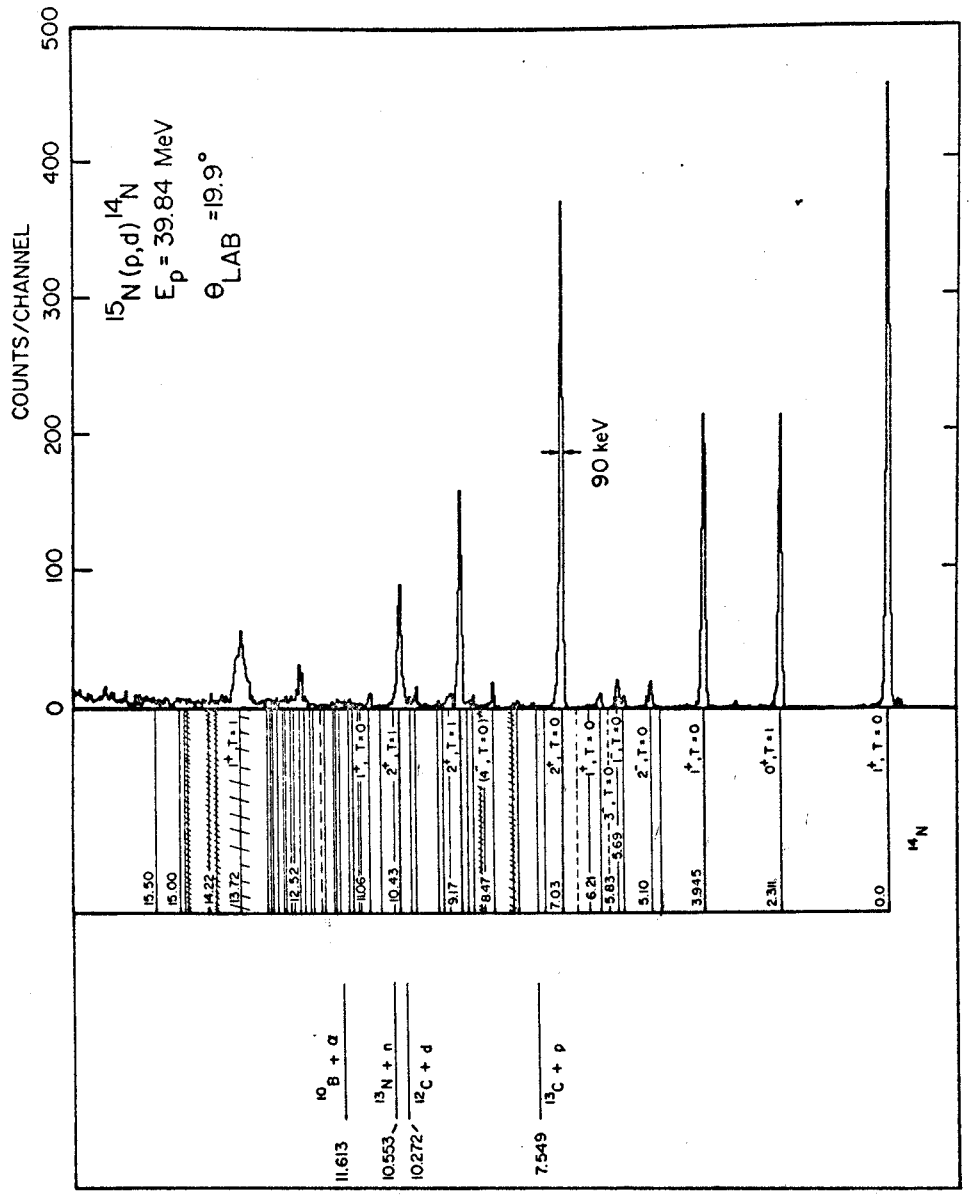

Figure V-15. : Energy level diagram of ^{14}N displayed beside a deuteron energy spectrum from the $^{15}N(p,d)^{14}N$ reaction for Ep=39.84 MeV and θ_{LAB}=19.9°. The seven strong levels are formed by 1p neutron pickup.

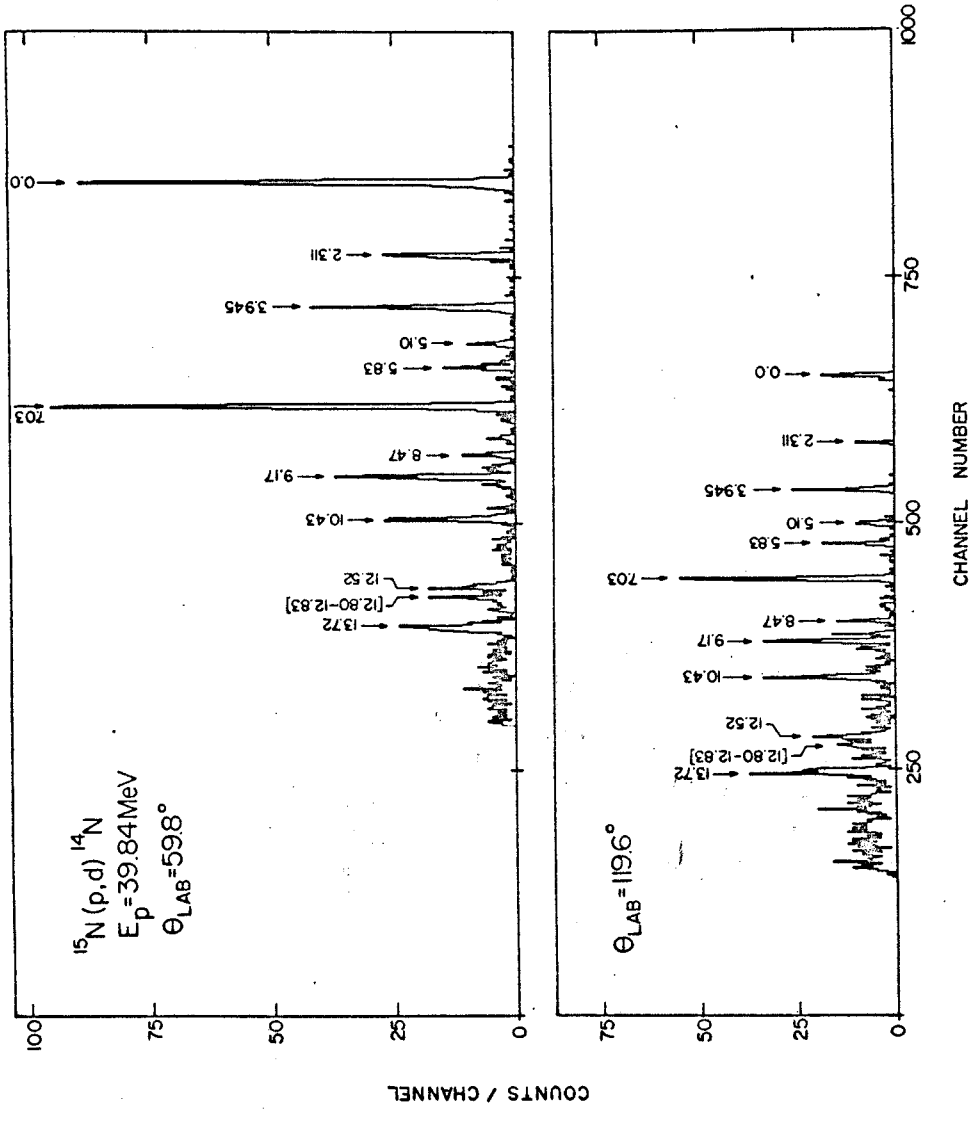

Figure V-16. Deuteron energy spectra at θ_{LAB}=59.8° and 119.6° from the $^{15}N(p,d)^{14}N$ reaction for E_p=39.84 MeV.

less. Angular distributions for the ten remaining levels are presented in Fig. V-17 and Fig. V-18. They all exhibit the characteristics of ℓ_n=1 transfer. J-dependence is again seen in the steeper slope of the 0^+ angular distribution ($p_{1/2}$ pickup) as compared to the 2^+ angular distributions ($p_{3/2}$ pickup). A Q-dependent effect is seen in the decreasing slopes of the 2^+ angular distributions with increasing excitation energy. The slopes of the 0.0 MeV, 1^+ and the 2.311 MeV, 0^+ angular distributions are very nearly the same, indicating, on the basis of J-dependence, that the ground state is populated mainly by $1p_{1/2}$ pickup, as one might expect from energy considerations. The other 1^+ angular distributions exhibit less steep slopes, indicating $1p_{3/2}$ pickup. The $^{15}N(p,d)^{14}N$ and $^{16}O(p,d)^{15}O$ ℓ_n=1 angular distributions are very similar.

The broad level at 13.72 MeV is particularly interesting. Its angular distribution (Fig. V-17) definitely exhibits an ℓ_n=1 shape, contradicting the previous assignment of J=3 (La 62). The strong excitation is also indicative of 1p neutron pickup, with the slope of the curve indicating $1p_{3/2}$ pickup. The width of the state has been determined from the various energy spectra by subtracting (in quadrature) the resolution from the measured width of the state. This value is 210±30 keV.

Angular distributions for the other levels which have been previously assigned $J = 0^+, 1^+, 2^+$ are shown in Fig. V-21. These levels are weakly excited, and their angular distributions do not contradict the assignments.

V.B.3. Levels Reached by $\ell_n \neq 1$ Pickup

The presence of levels other than 0^+, 1^+, or 2^+ is an indication of admixtures in the ground state of ^{15}N. As for the ^{16}O ground state, the most likely admixtures are $1d_{5/2}$ and $2s_{1/2}$, leading to the excitation of 2^- or 3^- and 0^- or 1^- states, respectively. Angular distributions for those levels having previous spin and parity assignments of 2^- and 3^- are shown in Fig. V-19. Most of the levels are very weakly excited. The level at 12.52 MeV had no previous assignment. It is rather strongly excited, especially for a state with such a high excitation energy, and its angular distribution is consistent with 1d pickup. Levels having previous spin and parity assignments of 0^- and 1^- are shown in Fig. V-20. These levels are also weak, in general, with the angular distributions of the levels at 4.91, 5.69, and 8.06 displaying the rise of the cross section toward a maximum at $\theta_{c.m.} = 0°$, which is characteristic of $\ell_n = 0$ pickup. If the 11° point is ignored, the shape of the angular distribution of the 13.17

MeV level is consistent with ℓ_n=0 pickup. The 1^- level at 10.213 MeV could be populated either by $2s_{1/2}$ or $1d_{3/2}$ pickup.

Also shown in Fig. V-20 are angular distributions for levels having previously been assigned $J^\pi = 3^+$ or 4^+. These would require 1f neutron pickup in the direct reaction picture. The angular distributions for the 12.61 and 12.80 MeV levels may contain contributions from other close-lying levels. Again, the cross sections are small. The existence of a level between the 10.55 and 11.06 MeV levels has been reported at 10.71 MeV (Pe 65), at 10.78 MeV (Ma 67a), and at 10.85 MeV (Ha 66), and at 10.85±0.02 MeV (Za 67). The spin and parity of this level have been given as (4^+) (Ma 67a). In the present work this level was very weakly excited, with an average excitation energy of 10.80±0.05. The angular distribution is shown in Fig. V-20. Several other levels were weakly excited. Spins and parities cannot be assigned by inspection of the angular distributions, which are shown in Fig. V-21. The peak cross sections for all levels excited in the $^{15}N(p,d)$ reaction are listed in Table VI-4.

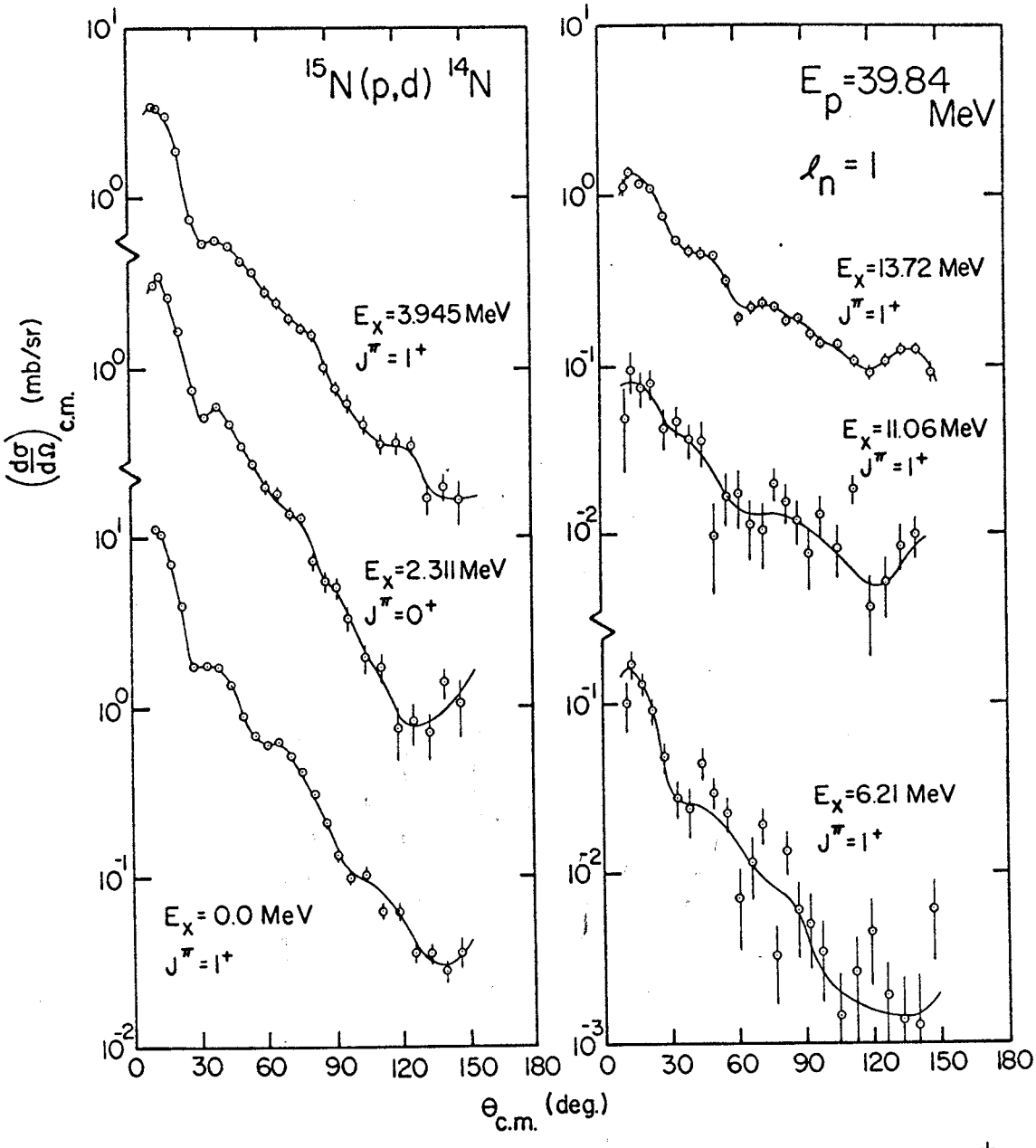

Figure V-17. Deuteron angular distributions for the 0^+ and 1^+ levels of ^{14}N strongly excited in the $^{15}N(p,d)^{14}N$ reaction for E_p=39.84 MeV.

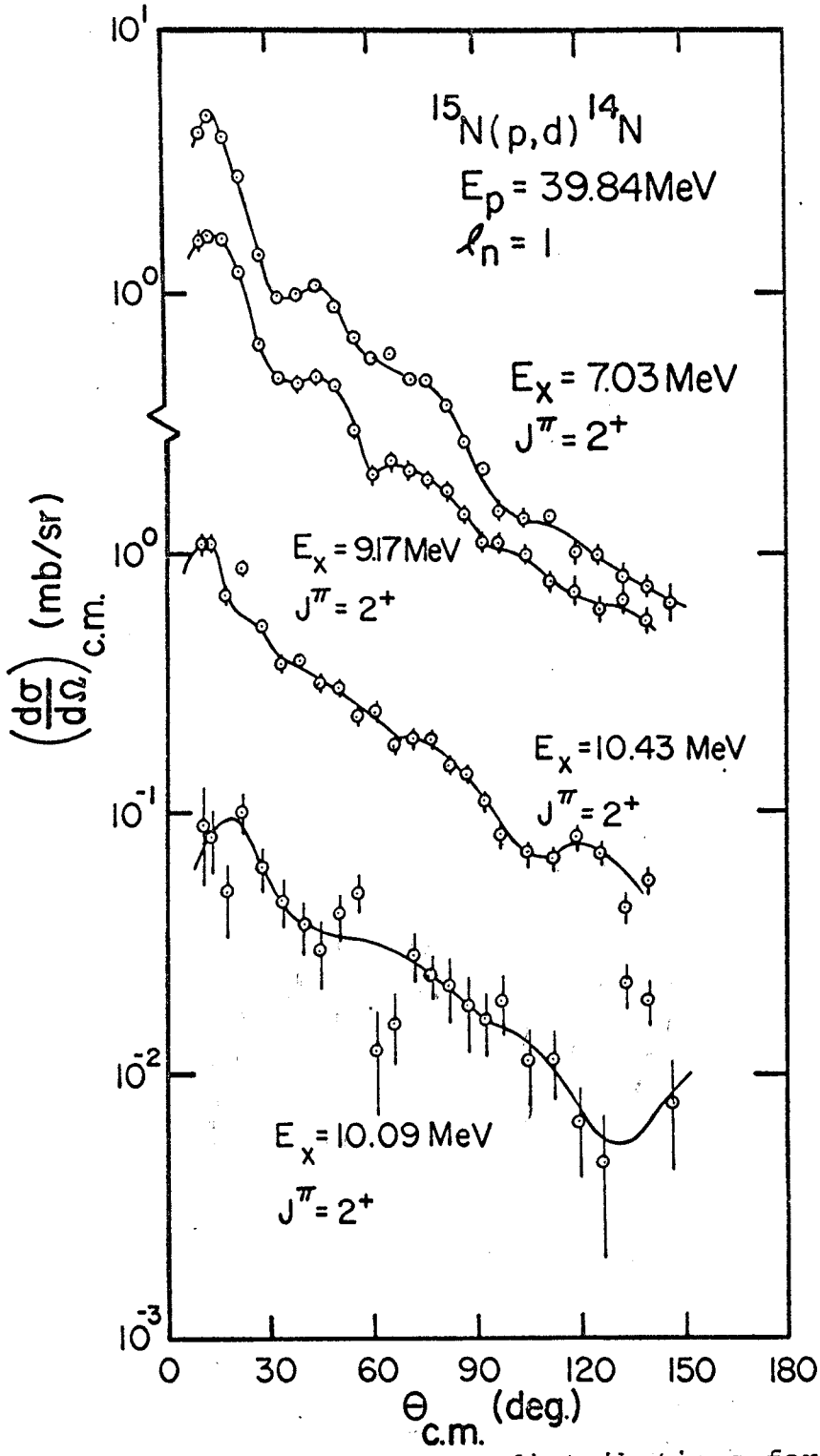

Figure V-18. Deuteron angular distributions for the 2^+ levels of ^{14}N strongly excited in the $^{15}N(p,d)^{14}N$ reaction for E_p=39.84 MeV.

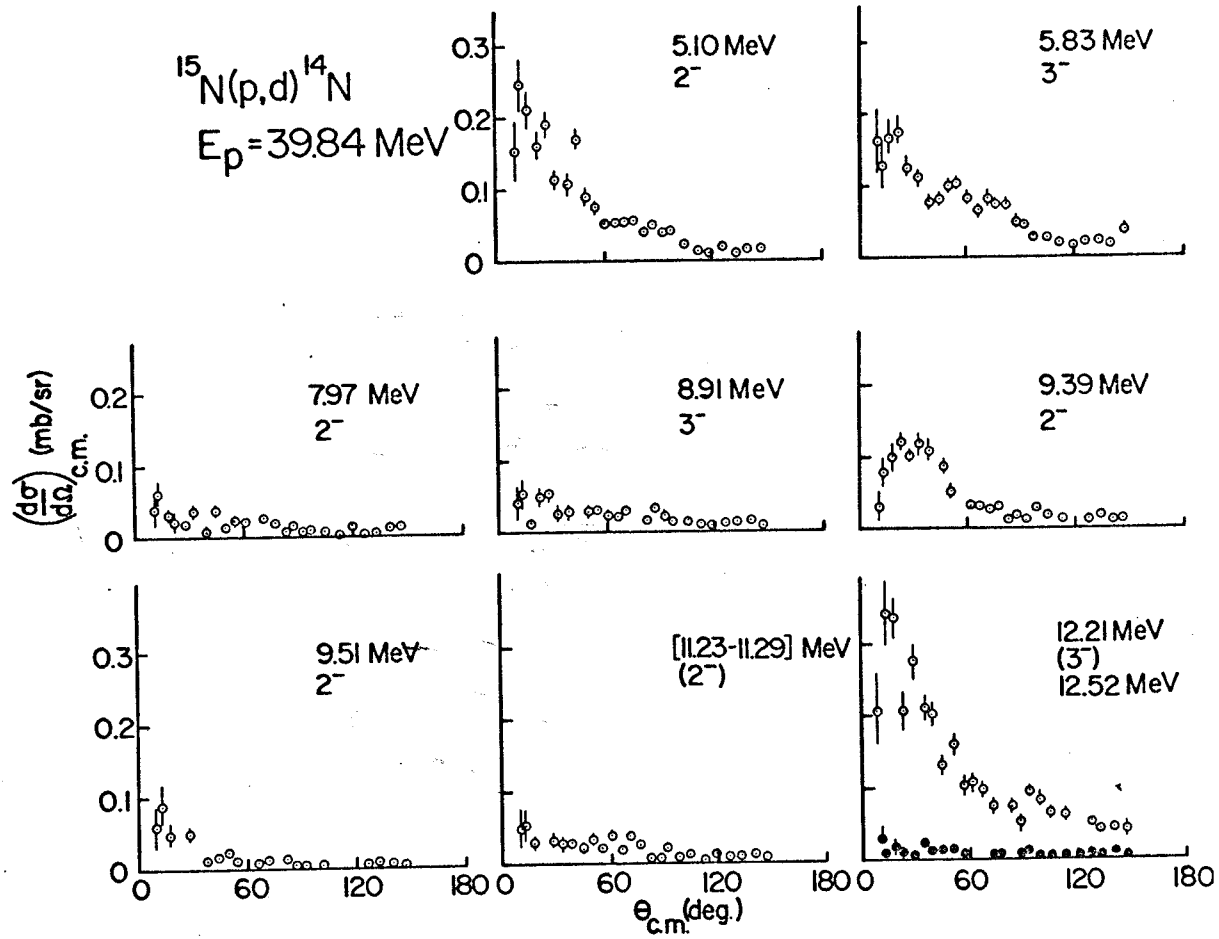

Figure V-19. Deuteron angular distributions for the 2^- and 3^- levels in ^{14}N excited by the $^{15}N(p,d)^{14}N$ reaction for E_p=39.84 MeV. The spin and parity assignments are from references quoted in the text.

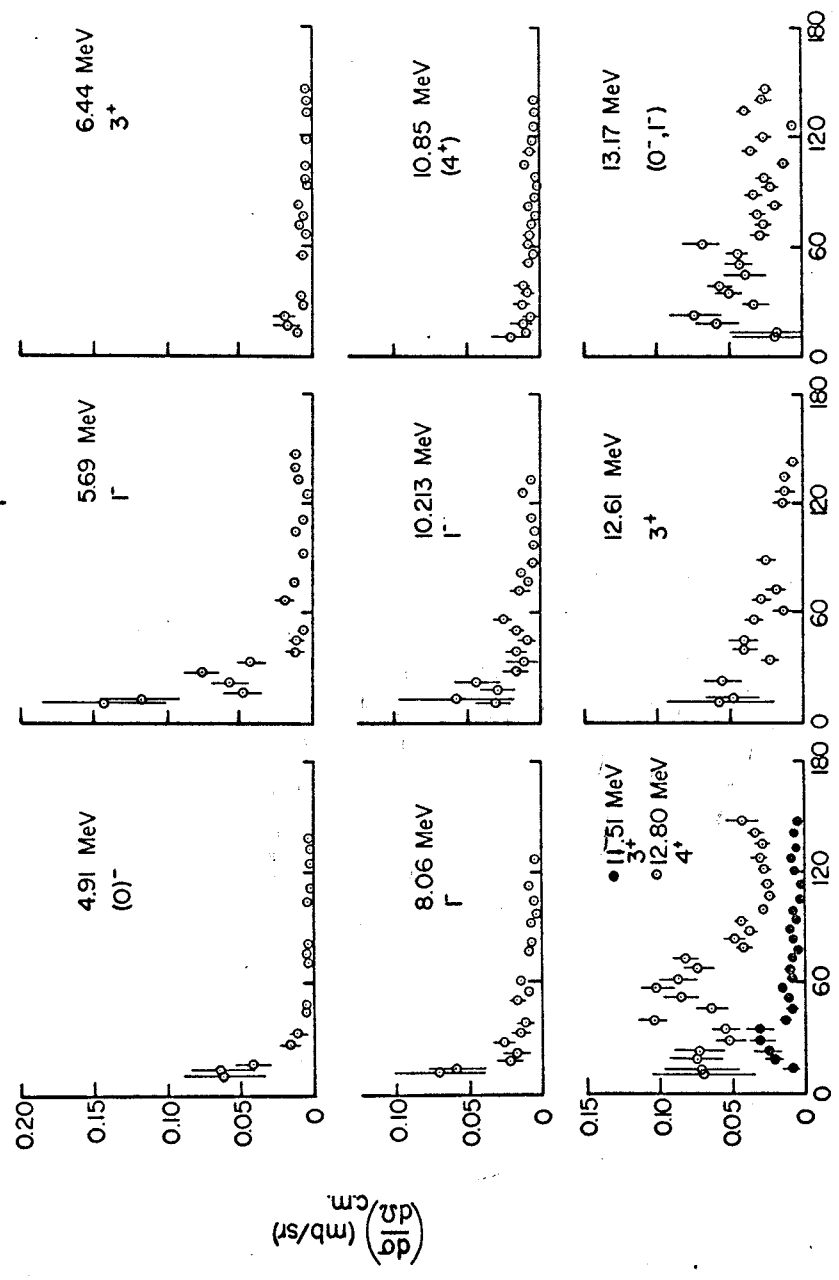

Figure V-20. Deuteron angular distributions for the 0^-, 1^-, 3^+, and 4^+ levels in ^{14}N excited by the $^{15}N(p,d)^{14}N$ reaction for E_p=39.84 MeV. The spin and parity assignments are from references quoted in the text.

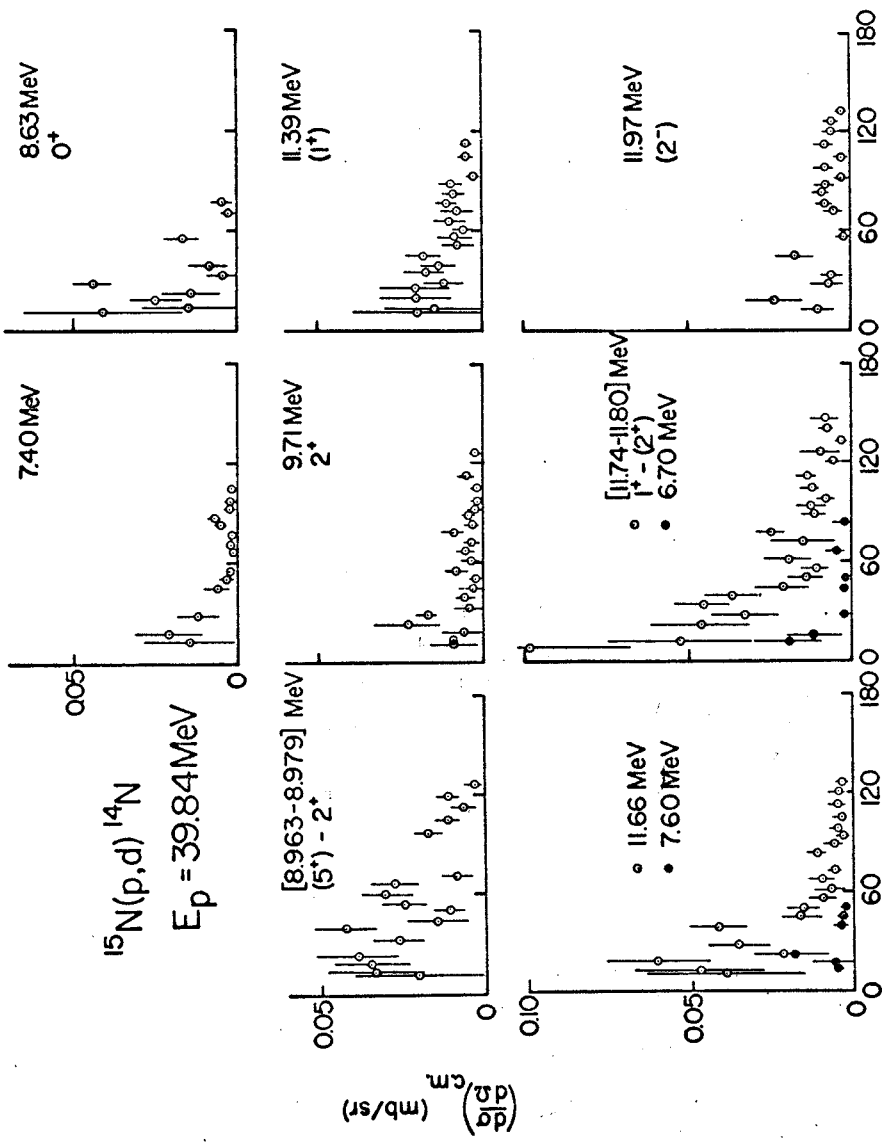

Figure V-21. Deuteron angular distributions for other levels of ^{14}N weakly excited by the $^{15}N(p,d)^{14}N$ reaction for E_p=39.84 MeV. The spin and parity assignments are from references quoted in the text.

CHAPTER VI

DWBA ANALYSIS, EXTRACTION OF SPECTROSCOPIC FACTORS, AND COMPARISON TO THEORY

VI.A. $^{16}O(p,d)^{15}O$

As was stated in Chapter I, one of the major purposes of this work was to study the extraction of spectroscopic factors (discussed in Chapter II) for neutron pickup from a light nucleus. The nucleus ^{16}O was chosen as a target because one has some feeling about the values of the spectroscopic factors for the reaction. The simplest shell model predicts spectroscopic factors of 2 and 4 for the 0.0 MeV, $1/2^-$ and the 6.18 MeV, $3/2^-$ levels of ^{15}O, respectively. These are just the numbers of $1p_{1/2}$ and $1p_{3/2}$ neutrons available for pickup. If, however, some of the 1p strength lies in other ^{15}O levels of higher excitation, the spectroscopic factors for the 0.0 and 6.18 MeV levels will be reduced, but the sum of the 1p spectroscopic factors will still be 6. However, if the ground state of ^{16}O were to contain admixtures of neutrons from other shells, the total number of 1p neutrons available for pickup would be less than 6, and since the

$1p_{1/2}$ neutrons are less strongly bound than the $1p_{3/2}$ neutrons, one might expect the $1p_{1/2}$ subshell to be depleted more than the $1p_{3/2}$ subshell. Thus, one would expect the ratio of the summed $1p_{3/2}$ spectroscopic factors to the summed $1p_{1/2}$ spectroscopic factors to be greater than 2. These conditions were considered when evaluating the results of a DWBA calculation.

A FORTRAN version of the Oak Ridge code JULIE,* running on the CDC 3600 computer at the Michigan State University Computer Center, was used for all DWBA calculations.

VI.A.1. DWBA Calculations and Spectroscopic Factors for the 0.0 and 6.18 MeV Levels

Initial DWBA calculations were made for 45.34 MeV incident protons. Optical model parameters for the entrance and exit channels are listed in Tables IV-1 and IV-2. The parameters for the bound state well were $r_{on} = 1.12$ F, $a_n = 0.69$ F, and $\lambda = 25$. The geometric parameters are the same as those of the real proton well, and the value of the spin-orbit strength is the one normally used for nucleons. No lower integration cutoff was used in initial calculations. As can be seen in

---

*JULIE is described in Refs. Ba 62 and Ba 66.

Fig. VI-1, the shape of the calculated angular distribution does not match the data. However, in studies of (p,d) reactions in 1p shell and 2s-1d shell nuclei, Kull (Ku 67) and Kozub (Ko 67a) found that an increase in the imaginary well depth (W_D) of the deuteron optical potential led to shapes which were in better agreement with the data. They found that increases of from 200 to 300% produced changes in the magnitude of the first peak of the differential cross section (hereafter referred to as σ_{peak}) of less than 20%. This was important since the value of the experimental spectroscopic factor depends on the value of σ_{peak} (see Chapter II for a discussion of the extraction of experimental spectroscopic factors). The same procedure was followed in the present case; the results are presented in Fig. VI-1. The shape does improve as W_D increases, but the shape of the data still is not well-reproduced. The worst feature, however, is that the magnitude of σ_{peak} decreases from 1.5 mb/sr to 0.6 mb/sr as W_D increases from W_{D0} to $4W_{D0}$. These values give spectroscopic factors of 3.6 and 8.9, respectively, much too large for $1p_{1/2}$ pickup.

Siemssen (Si 67) also encountered the difficulty of reproducing the shape of the data from (d,p) reactions with 1p shell nuclei. He obtained reasonable fits by using a

lower integration cutoff in the DWBA calculation. Following a similar procedure, W_D was kept at the value found from optical model calculations, and a series of DWBA calculations was made with different values of the lower integration cutoff radius (R_{cutoff}). The effect of the cutoff radius on σ_{peak} is shown in Fig. VI-2. Two maxima exist, one at R_{cutoff} = 0 F and one at R_{cutoff} = 3 F. For R_{cutoff} = 0 F the spectroscopic factor for the 0.0 MeV level is 3.2, whereas for R_{cutoff} = 3 F it is 1.8, a much more acceptable value. For the 6.18 MeV level there is no appreciable difference in the spectroscopic factors for R_{cutoff} = 0 F and R_{cutoff} = 3 F. Figures VI-3 and VI-4 show the DWBA angular distributions for the ground and 6.18 MeV states. The shape for R_{cutoff} = 3 F is better than that for R_{cutoff} = 0 F, but is still not very good. However, the first maximum is reasonably well-reproduced, so the prescription of using the measured optical parameters with a lower integration cutoff of 3 F was adopted for all of the DWBA calculations.

Fixing the optical parameters and the integration limits left only the parameters of the bound state well to be investigated. Since the value of 1.12 F for the radius parameter (r_{on}) was somewhat smaller than that generally used, calculations were performed for r_{on} = 1.25 and 1.35 F.

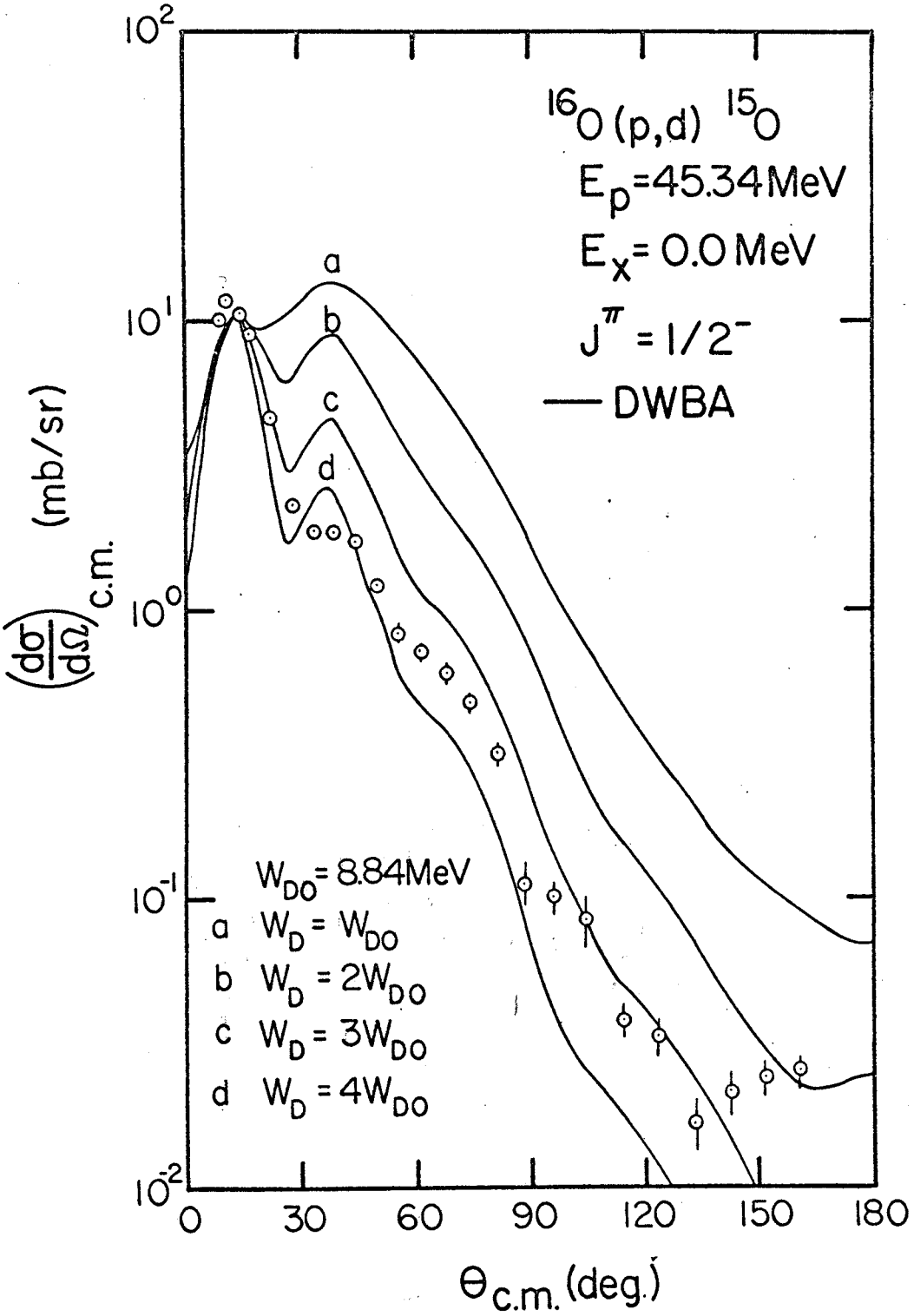

Figure VI-1. DWBA fits to the $^{16}O(p,d)^{15}O$, E_p=45.34 MeV, E_x=0.0 MeV, J^π=1/2$^-$ angular distribution for different values of the imaginary well depth. All curves have been normalized to the first maximum of the experimental angular distribution.

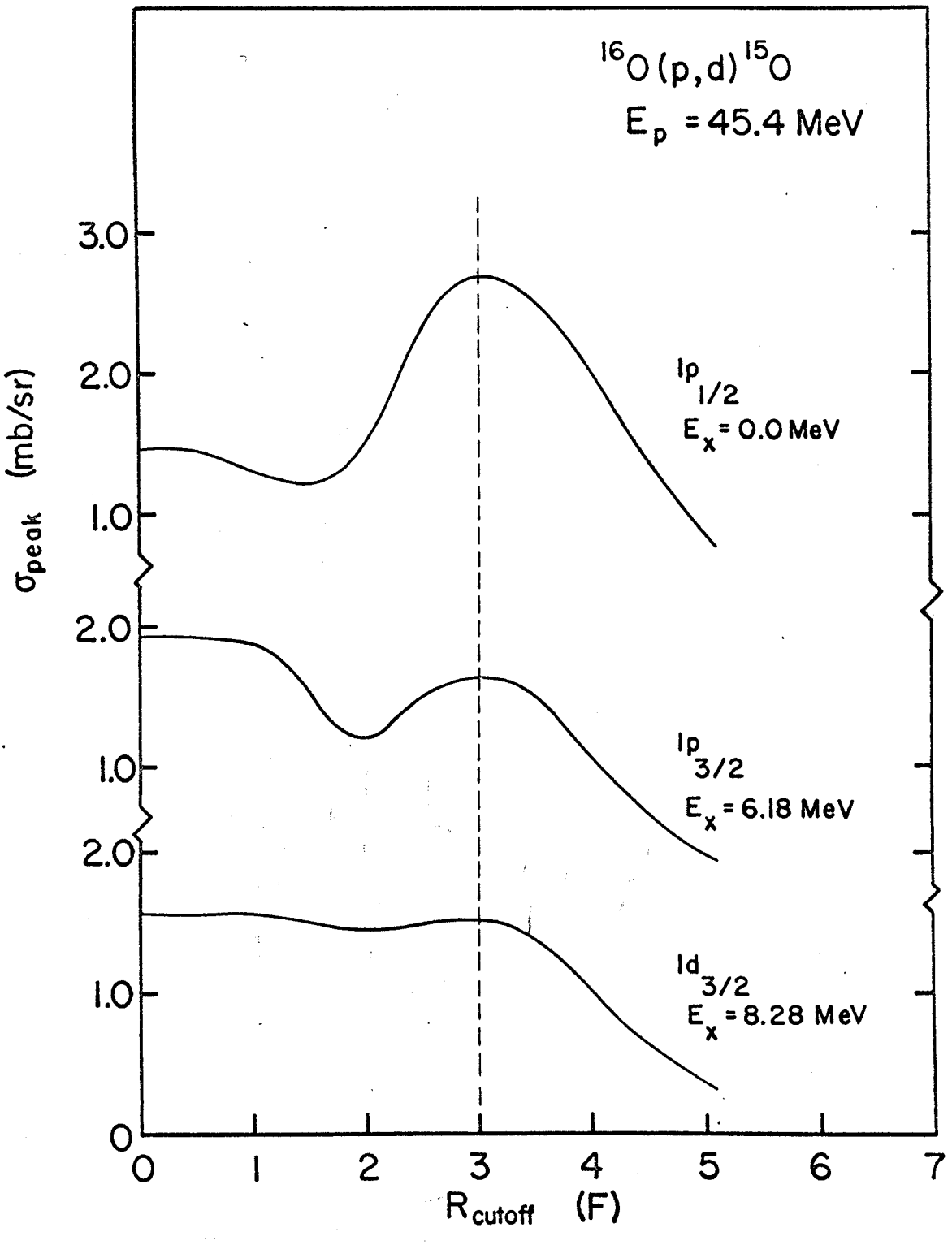

Figure VI-2. Dependence of the calculated ℓ_n=1 and ℓ_n=2 peak cross sections from the $^{16}O(p,d)^{15}O$ reaction for E_p=45.34 MeV on the value of the lower radial integration cutoff used in the DWBA calculations.

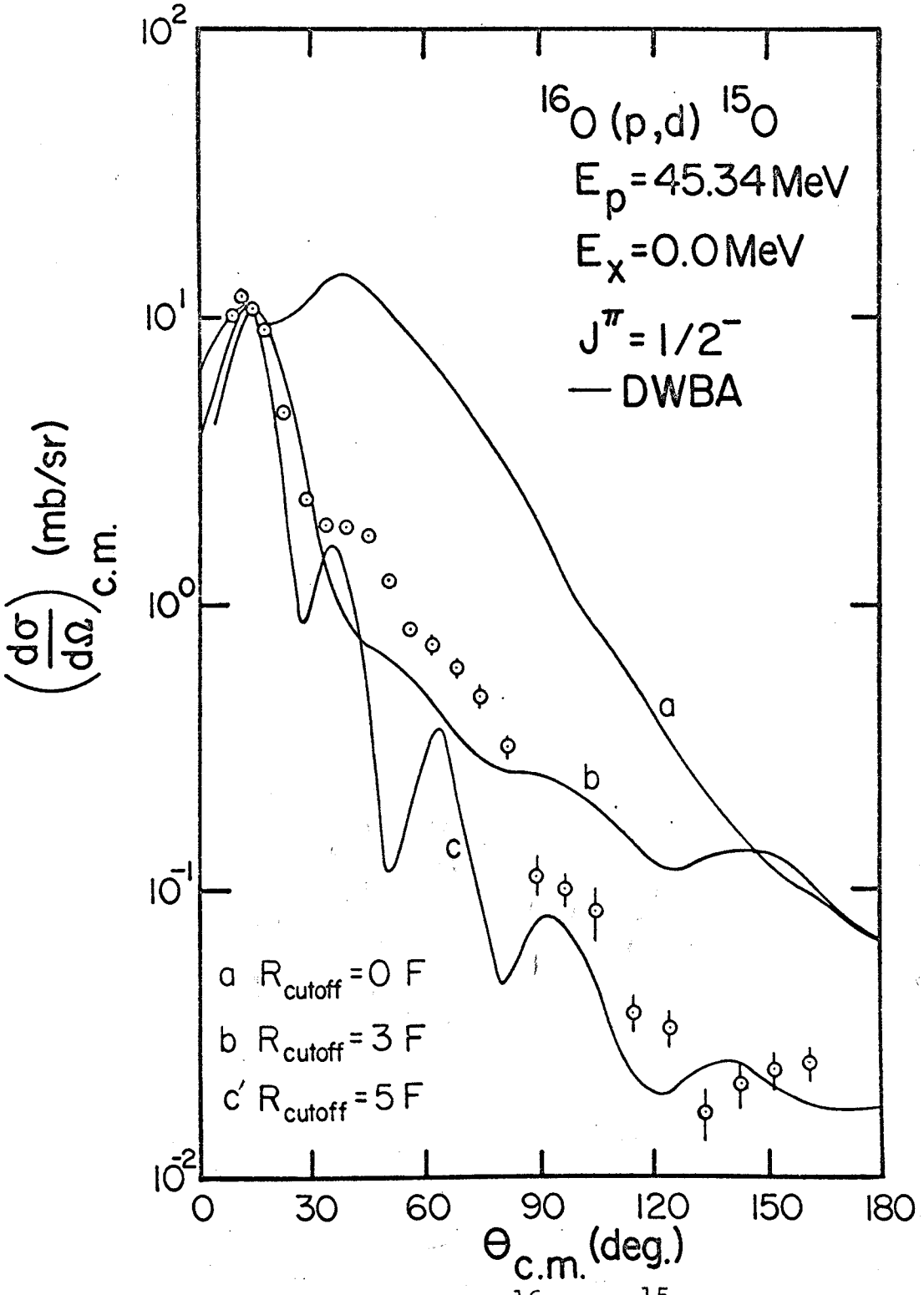

Figure VI-3. DWBA fits to the $^{16}O(p,d)^{15}O$, E_p=45.34 MeV, E_x=0.0 MeV, J^π=1/2$^-$ angular distribution for different values of the lower radial integration cutoff. All curves have been normalized to the first maximum of the experimental angular distribution.

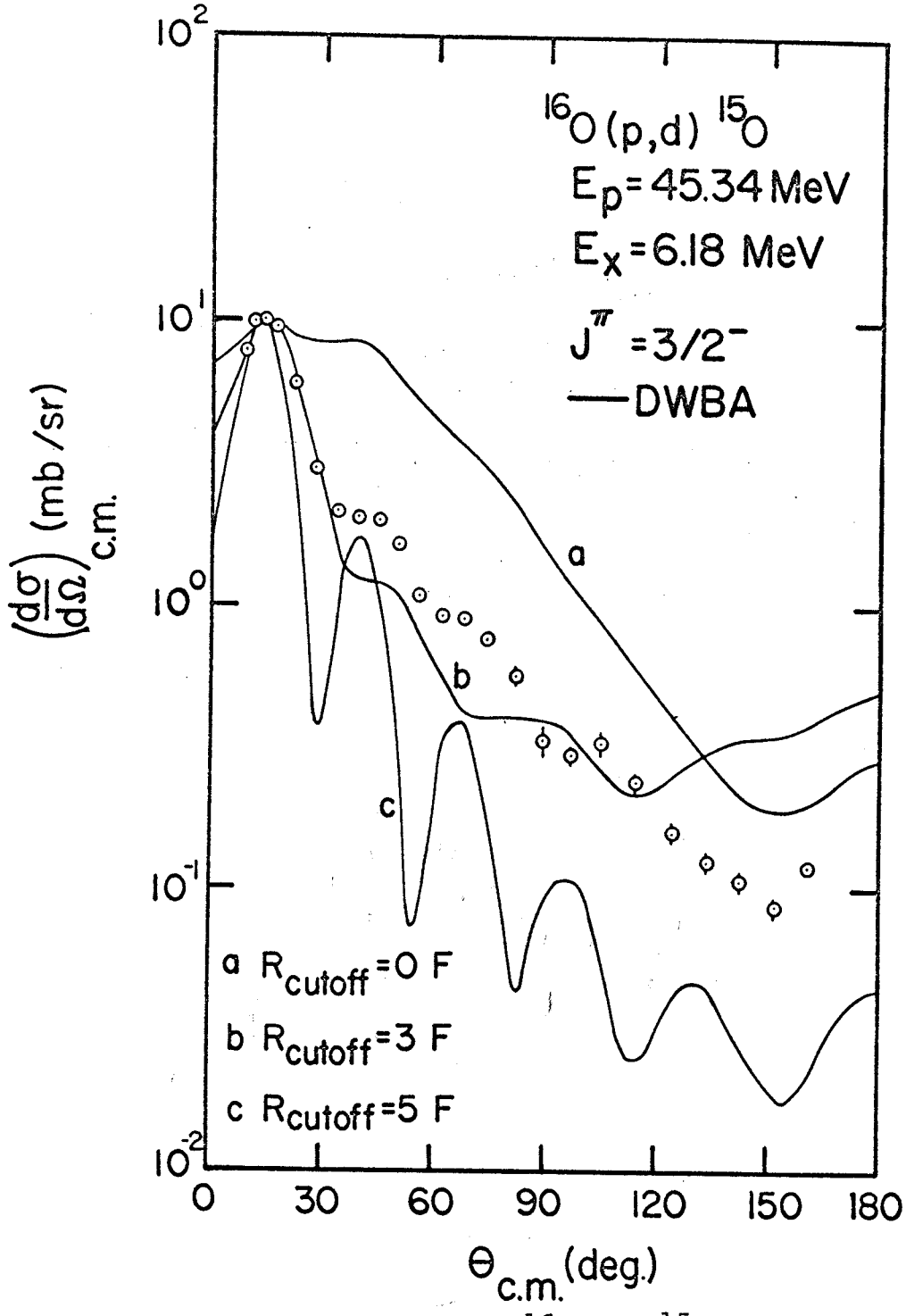

Figure VI-4. DWBA fits to the $^{16}O(p,d)^{15}O$, E_p=45.34 MeV, E_x=6.18 MeV, J^π=3/2⁻ angular distribution for different values of the lower radial integration cutoff. All curves have been normalized to the first maximum of the experimental angular distribution.

The shapes of the angular distributions were essentially unaltered, but σ_{peak} for the ground state rose from its value of 2.68 mb/sr for r_{on} = 1.12 F to 4.35 mb/sr for r_{on} = 1.35 F. This represents a lowering of the ground state spectroscopic factor, the value being 1.51 for r_{on}= 1.25 F. This value of the spectroscopic factor is reasonable, but that for the 6.18 MeV, $3/2^-$ level seems much too small since the ratio of the $1p_{3/2}$ to the $1p_{1/2}$ spectroscopic factors is essentially unchanged by the change in r_{on}. Owing to the lack of significant improvement in the shape and magnitude of the angular distributions with a higher value of r_{on}, the value of r_{on} was kept at 1.12 F for the subsequent calculations.

It was noted in Chapter II that the inclusion of finite-range and non-locality effects in the DWBA calculations tends to reduce the effect of the nuclear interior. Since this is also the effect of a lower integration cutoff, a set of calculations including these effects was made. The code FANLFR2* was used to obtain the bound state form factor which was then used by JULIE in the DWBA calculation. Since the shape of the angular distribution was little improved from that calculated using the zero-range

---

*Oak Ridge computer code FANLFR2, written by J.K. Dickens.

approximation and R_{cutoff} = 0 F, and a value of 3.0 was obtained for the ground state spectroscopic factor, the use of finite-range and non-locality was abandoned.

Having decided to use a lower integration cutoff with the normal deuteron optical model parameters, calculations were performed for the 0.0 MeV, $1/2^-$ and 6.18 MeV, $3/2^-$ levels for incident proton energies of 25.52, 31.82, 38.62, and 45.34 MeV. The optical parameters used were those which described elastic scattering at the appropriate energy. This means that the deuteron parameters used for the 0.0 MeV level were different from those for the 6.18 MeV level. The method used in choosing the four proton energies is illustrated in Fig. VI-5. For an incident proton energy E_p (e.g., 25.52 MeV) the deuterons leaving ^{15}O in the 0.0 MeV, $1/2^-$ state have the same energy in the center-of-mass frame as those leaving ^{15}O in the 6.18 MeV, $3/2^-$ state when the incident proton energy is E_p' (e.g., 31.82 MeV). Thus, deuteron parameters used in the DWBA calculation for the 6.18 MeV level for 45.34 MeV incident protons are the same as those for the 0.0 MeV calculation for 38.62 MeV incident protons.

The results of these calculations are presented in Figs. VI-3--VI-4, VI-6--VI-8, and in Tables VI-1 and VI-2. The shapes are reasonable for the higher energies, but are

BASIS FOR SELECTION OF INCIDENT PROTON ENERGIES

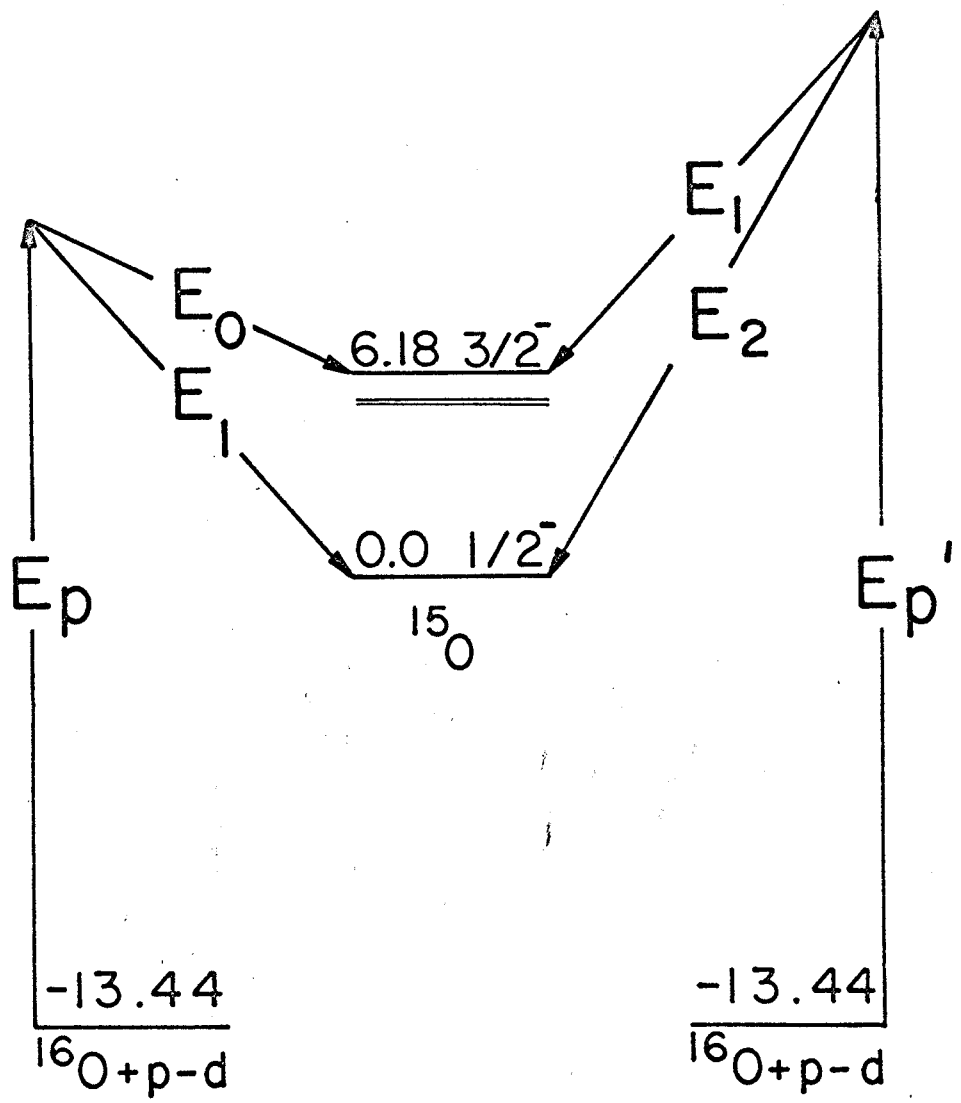

Figure VI-5. Basis for the selection of incident proton energies for the $^{16}O(p,d)^{15}O$ experiments.

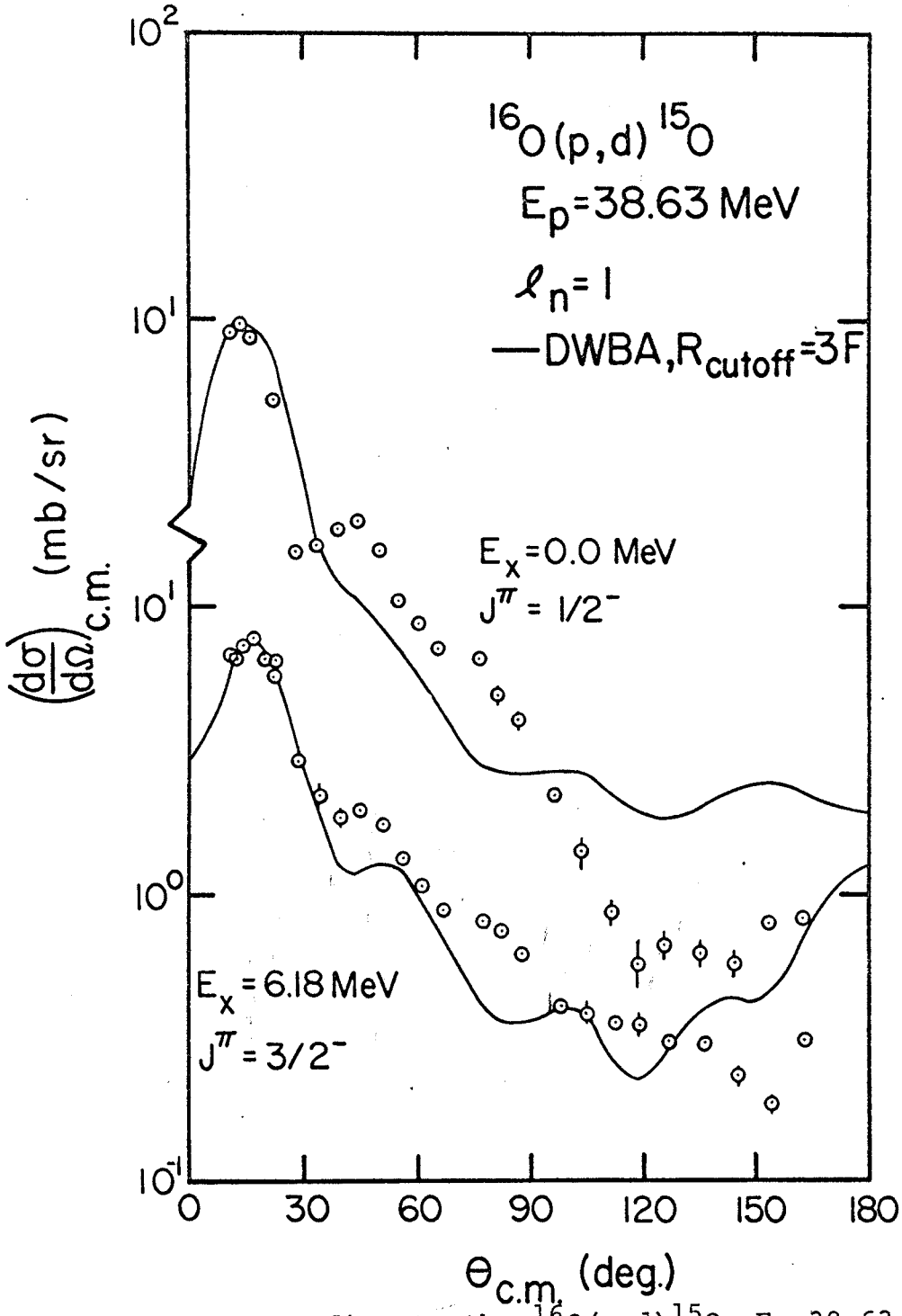

Figure VI-6. DWBA fits to the $^{16}O(p,d)^{15}O$, E_p=38.63 MeV, E_x=0.0 and 6.18 MeV angular distributions.

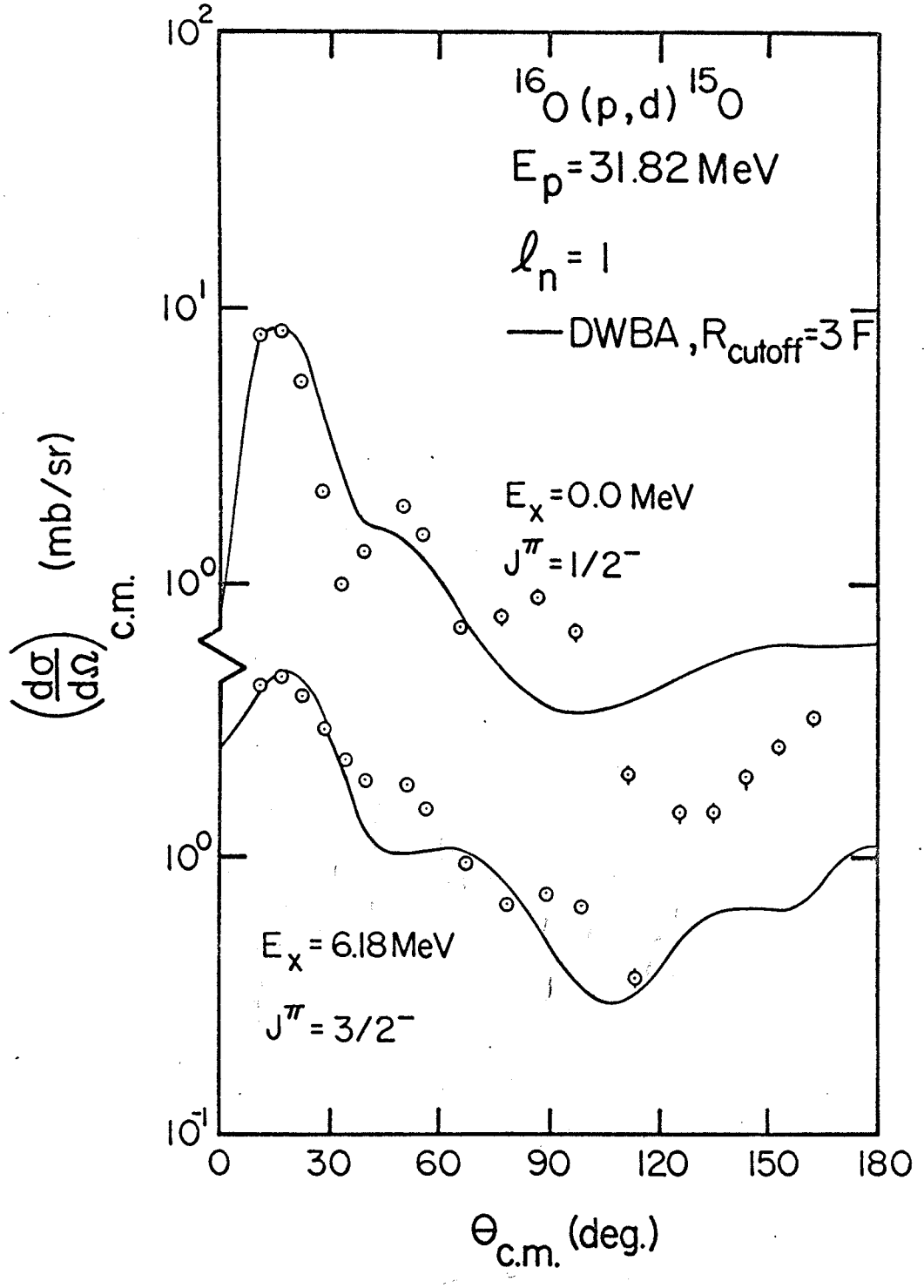

Figure VI-7. DWBA fits to the $^{16}O(p,d)^{15}O$, E_p=31.82 MeV, E_x=0.0 and 6.18 MeV angular distributions.

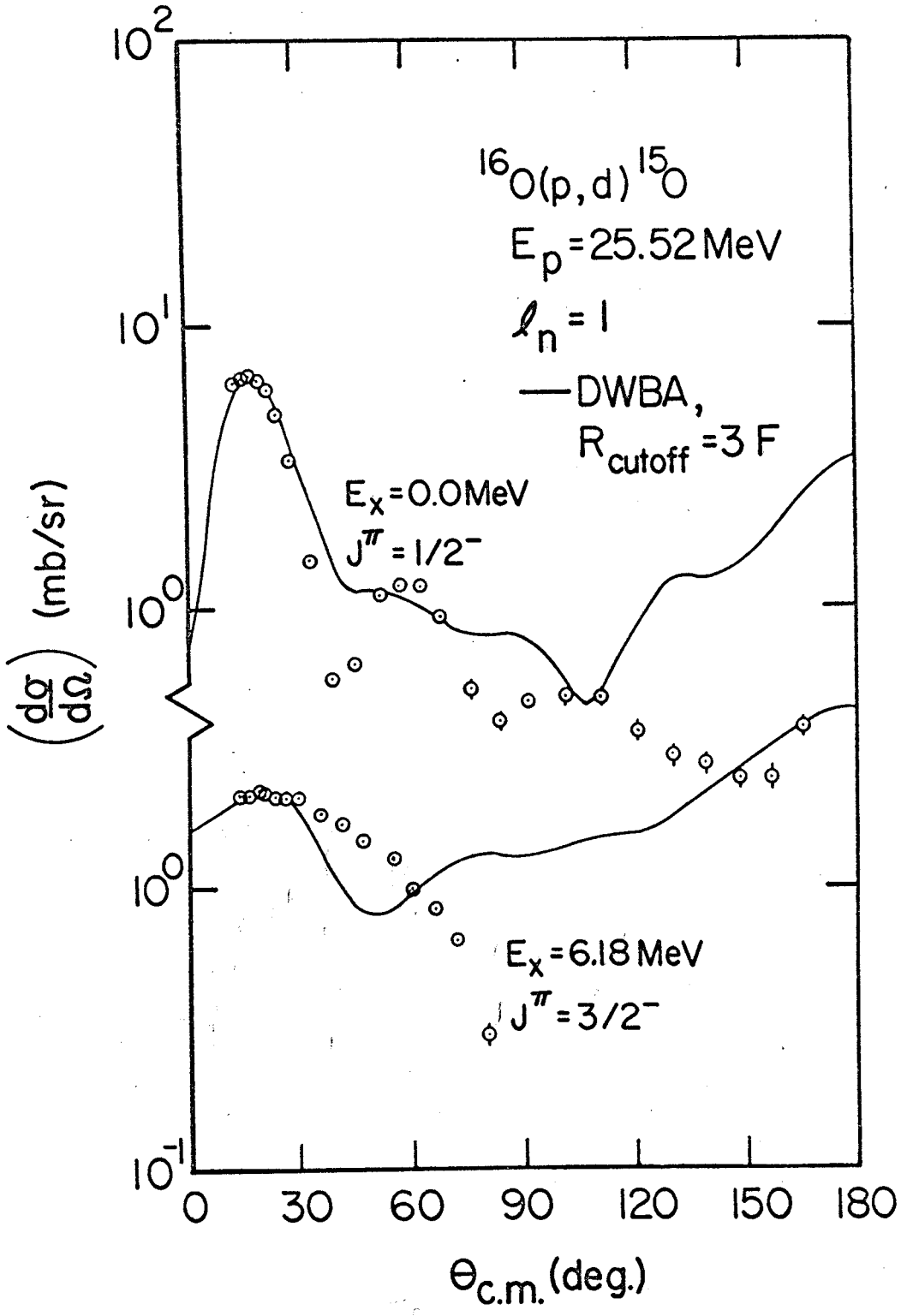

Figure VI-8. DWBA fits to the $^{16}O(p,d)^{15}O$, E_p=25.52 MeV, E_x=0.0 and 6.18 MeV angular distributions.

significantly worse for the 25.52 MeV data. The rather low deuteron energies for this latter case made the assumption of a direct reaction questionable. Spectroscopic factors and ratios of spectroscopic factors for the 0.0 and 6.18 MeV levels are given in Tables VI-1 and VI-2, where the errors reflect only the errors in the values of σ_{exp}. The extracted spectroscopic factor for the ground state is constant for the two higher bombarding energies, but it increases for lower values of the incident proton energy. The spectroscopic factor for the 6.18 MeV level rises as the energy of the incident protons decreases from 45 MeV. Table VI-2 shows that the ratios of the spectroscopic factors for these levels is reasonably constant for incident proton energies greater than 30 MeV. The ratios given in the last column are based upon use of the proton energy scheme shown in Fig. VI-5 to reduce any Q-dependent effects. Only the ratios for the 45.34 MeV data remain unchanged. These data indicate that if reliable spectroscopic factors are to be extracted from the (p,d) reaction on light nuclei, the incident proton energy must be sufficient to produce deuterons having an energy greater than 22 MeV in the center-of-mass frame. Relative spectroscopic factors appear to be reliable even for lower incident proton energies or, conversely, for higher excitation energies.

Table VI-1. Experimental spectroscopic factors for the 0.0 and the 6.18 MeV levels of ^{15}O from the $^{16}O(p,d)^{15}O$ reaction induced by 25.52-45.34 MeV protons.

E_x (MeV)	J^π	E (MeV)	σ_{exp} (mb/sr)	σ_{DWBA} (mb/sr)	S
0.0	$1/2^-$	25.52	6.8±0.5	0.94	3.2±0.2
		31.82	8.5±0.6	1.66	2.3±0.2
		38.63	9.7±0.5	2.38	1.8±0.1
		45.34	11.0±0.8	2.68	1.8±0.1
6.18	$3/2^-$	25.52	2.2±0.2	0.12	8.1±0.7
		31.82	4.5±0.5	0.57	3.5±0.4
		38.63	7.6±0.6	1.14	3.0±0.3
		45.34	10.0±0.7	1.72	2.6±0.2

Table VI-2. Ratios of experimental spectroscopic factors for the 0.0 and 6.18 MeV levels of ^{15}O from the $^{16}O(p,d)^{15}O$ reaction induced by 25.52-45.34 MeV protons.

E_p^+ (MeV)	E_p^- (MeV)	$S_{3/2}(E_p^+)/S_{1/2}(E_p^+)$	$S_{3/2}(E_p^+)/S_{1/2}(E_p^-)$
25.52	---	2.53±0.25	---
31.82	25.52	1.54±0.15	1.09±0.11
38.63	31.82	1.63±0.16	1.30±0.13
45.34	38.63	1.41±0.14	1.41±0.14

It is interesting to note the similarity of the ratio of spectroscopic factors for the 6.18 MeV, $3/2^-$ and 0.0 MeV, $1/2^-$ transitions from the 45.34 MeV data to the ratio of the peak cross sections of these levels from the 100 MeV data.

It is possible to obtain better agreement between the DWBA calculations and the shapes of the experimental angular distributions. Chant et al. (Ch 67) freely adjusted the deuteron optical model parameters to obtain the best fit to the ground state angular distribution from their 30.3 MeV $^{16}O(p,d)^{15}O$ data. The imaginary well depth was increased by a factor of approximately 3, with changes of 5-20% being made in the other parameters. The fit was very good for the ground state angular distribution below 78° in the center-of-mass frame, where the data ended, but the 6.18 MeV fit was not as good. They did not calculate spectroscopic factors, so the quality of the fits could not be judged by that criterion. However, the calculations of the present work showed that an increase of the imaginary well depth led to spectroscopic factors which were much too large. Thus, the value of such a fit is questionable.

A study similar to that of the present work has been made by Hiebert et al. (Hi 67) for proton pickup from ^{16}O.

The $^{16}O(d,^3He)^{15}N$ reaction was employed with an incident deuteron energy of 34.4 MeV. Satisfactory fits to the data were obtained using standard optical model potentials. They found that the local finite-range form of the DWBA theory gave the most reliable spectroscopic factors. These values were 2.14 for the 0.0 MeV, $1/2^-$ level of ^{15}N and 3.72 for the 6.33 MeV, $3/2^-$ level. These are not in good agreement with the present values for neutron pickup from ^{16}O presented in Table VI-1, and probably reflect more the uncertainty in the extraction of spectroscopic factors than a dissimilarity of the proton and neutron configurations of the ^{16}O ground state.

VI.A.2. Spectroscopic Factors for Other Levels, and the Ground State of ^{16}O

Using the criteria established in the previous section, DWBA calculations were performed for other levels in the 45.34 MeV data. The results are similar to those for the strong levels shown in the previous sections. Spectroscopic factors for these levels are given in Table VI-3. Again, the errors quoted reflect only the errors in the experimental value of the σ_{peak}. An estimate of the spectroscopic factors for the 5.188 and 5.240 MeV levels was obtained by adding together $2s_{1/2}$ and $1d_{5/2}$ DWBA angular

Table VI-3. Peak cross sections and spectroscopic factors for the levels observed in ^{15}O. The average cross section over the indicated angular range is given for weak levels having angular distributions showing no characteristic maximum. The uncertainties quoted in the spectroscopic factors represent only the uncertainties in σ_{peak}.

E_x (MeV)	J^π	σ_{peak} (mb/sr)	θ_{peak} (deg)	S
0.0	$1/2^-$	11.0 ± 0.8	12 ± 1	1.8 ± 0.1
5.188	$1/2^+$			0.02 ± 0.01
5.240	$5/2^+$			0.11 ± 0.01
6.180	$3/2^-$	10.0 ± 0.7	15 ± 1	2.6 ± 0.2
6.789	$3/2^+$	0.08 ± 0.03	20 ± 2	0.02 ± 0.01
6.857	(3/2,5/2)	0.08 ± 0.03	20 ± 2	0.02 ± 0.01
7.284	$(9/2^+,7/2^+)$	0.12 ± 0.02	45 ± 3	0.03 ± 0.01
7.550	$1/2^+$	0.08 ± 0.03	30 ± 3	
8.283	$3/2^+$	0.05 ± 0.02	24 ± 3	0.01 ± 0.005
8.915	$3/2^+$			
8.980	$3/2^-$	0.08 ± 0.04	21 ± 5	0.04 ± 0.02
9.49	$5/2^-$			
9.53	$1/2^+$	0.57 ± 0.05*	15 ± 1	
9.60	$3/2^-$	0.40 ± 0.07**	15 ± 1	0.18 ± 0.03
9.66	$(7/2,9/2)^-$			
10.28		0.06 ± 0.02	10- - 46	
10.46	$(3/2^-,1/2^-)$	0.58 ± 0.06	15 ± 1	0.28 ± 0.03
10.94		0.08 ± 0.03	10- - 46	
11.02		0.06 ± 0.02	18- - 46	
11.70		0.06 ± 0.02	24- - 46	
12.30		0.12 ± 0.05	24 ± 3	
13.79		0.12 ± 0.05	9- - 46	

*This number represents the combination of the four peaks between 9.49 and 9.66 MeV.

**This number represents the estimated contribution of the 9.60 MeV level alone.

distributions in varying combinations. The results are shown in Fig. VI-9. A combination of $1d_{5/2}$ and $2s_{1/2}$ in the ratio 10 to 1 appears to give the best overall fit. The spectroscopic factor for the 7.284 MeV, $7/2^+$ level assumes that its excitation is due only to a direct process. It thus represents an upper limit.

It is interesting to determine the total 1p strength seen in the $^{16}O(p,d)^{15}O$ reaction at 45.34 MeV. By summing the spectroscopic factors for all of the $1/2^-$ and $3/2^-$ levels listed in Table VI-3, we get

$$\sum S(1p_{1/2}) = 1.80, \quad \sum S(1p_{3/2}) = 3.10,$$

hence

$$\sum S(1p) = 4.90.$$

The relatively low value for the total $1p_{3/2}$ strength indicates the possibility of higher $3/2^-$ levels, as predicted by Bertsch (Be 68). The $3/2^-$ levels at 9.60 and 10.46 MeV might comprise the $3/2^-$ level predicted by Brown and Shukla (Br 67) to be between 10 and 11 MeV. If it were at 10 MeV, they predict it would have a spectroscopic factor 3% of that of the 6.18 MeV level. Experimentally, the ratio is 18%. An estimate of the 2s-1d admixtures in the ground state of ^{16}O is

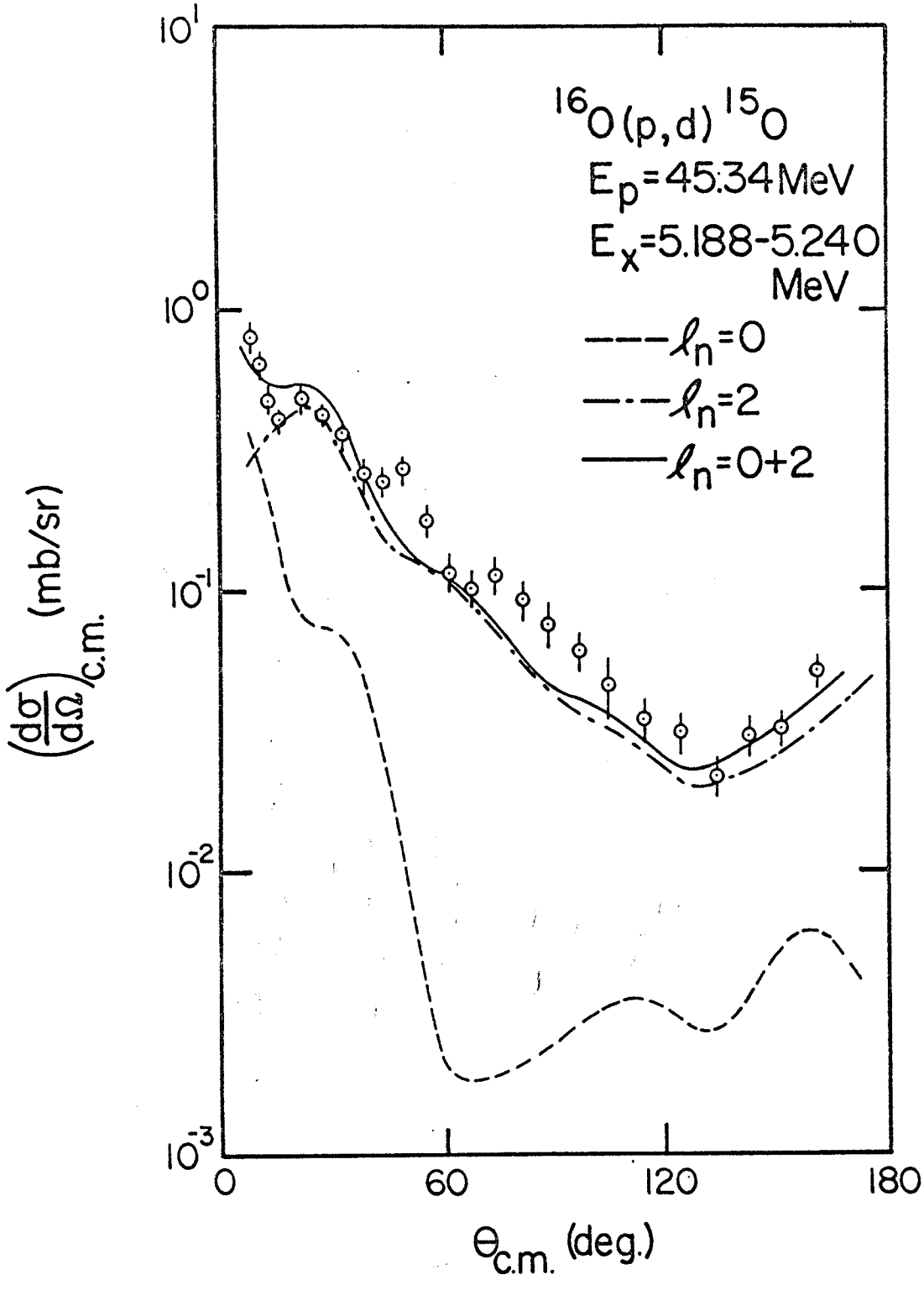

Figure VI-9. DWBA fit to the $^{16}O(p,d)^{15}O$, E_p=45.34 MeV, E_x=5.188-5.240 MeV (doublet) angular distribution. The ℓ_n=0 and ℓ_n=2 angular distributions are added in the ratio 1:10 to produce the solid curve.

contained in the spectroscopic factors for the $1/2^+$, $5/2^+$, and $3/2^+$ levels.

$$\sum S(2s_{1/2}) = \sim 0.02, \quad \sum S(1d_{5/2}) = 0.15, \quad \sum S(1d_{3/2}) = 0.04.$$

The present results can also be compared to those calculated from the ^{16}O ground state wave function of Brown and Green (Br 66a). This wave function has the form

$$|^{16}O \text{ g.s.}> = 0.874\,|0p\text{-}0h> + 0.469\,|2p\text{-}2h> + 0.130\,|4p\text{-}4h>,$$

where p is for particles and h is for holes. In the 2p-2h and 4p-4h admixtures one can assume that on the average half of the particles and holes are neutrons, and half protons. Thus, the 0p-0h portion represents six 1p neutrons, and the 2p-2h and 4p-4h portions represent five and four 1p neutrons, respectively. One would then expect the summed 1p spectroscopic factor to be

$$\sum S(1p) = 6(0.874)^2 + 5(0.469)^2 + 4(0.130)^2 = 5.75$$

and

$$\sum S(\text{other}) = 0(0.874)^2 + 1(0.469)^2 + 2(0.130)^2 = 0.25.$$

The sum of the experimental 2s-1d spectroscopic factors agrees well with this prediction. It appears, then, that as much as 15% of the 1p strength could be in levels above 10.46 MeV.

VI.B. $^{15}N(p,d)^{14}N$

VI.B.1. DWBA Calculations and Experimental Spectroscopic Factors

The DWBA calculations for the $^{15}N(p,d)^{14}N$ reactions were made in the same manner as those for $^{16}O(p,d)^{15}O$. A lower integration cutoff of 3F was used, which represented a peak in the σ_{peak} vs R_{cutoff} curve. The parameters of the bound state well were the same also. The optical model parameters were discussed in Chapter IV.

The shapes of the calculated angular distributions agreed with the data to approximately the same degree as those for ^{16}O. Those for some of the ℓ_n=1 levels are shown in Figs. VI-10 and VI-11. The 0^-, 1^-, 2^-, and 3^- levels represent 2s-1d admixtures in the ^{15}N ground states. DWBA calculations for one of these levels are shown in Fig. VI-12. The experimental spectroscopic factors extracted for the levels are given in Table VI-4. Again, the errors quoted reflect only the experimental error. The decision as to whether a 1^+ level was formed by $1p_{1/2}$ or $1p_{3/2}$ pickup was made on the basis of shape of the angular distribution (J-dependence) and on the predictions of Cohen and Kurath (Co 67), to be discussed in the next section. The amount of 2s-1d admixture in

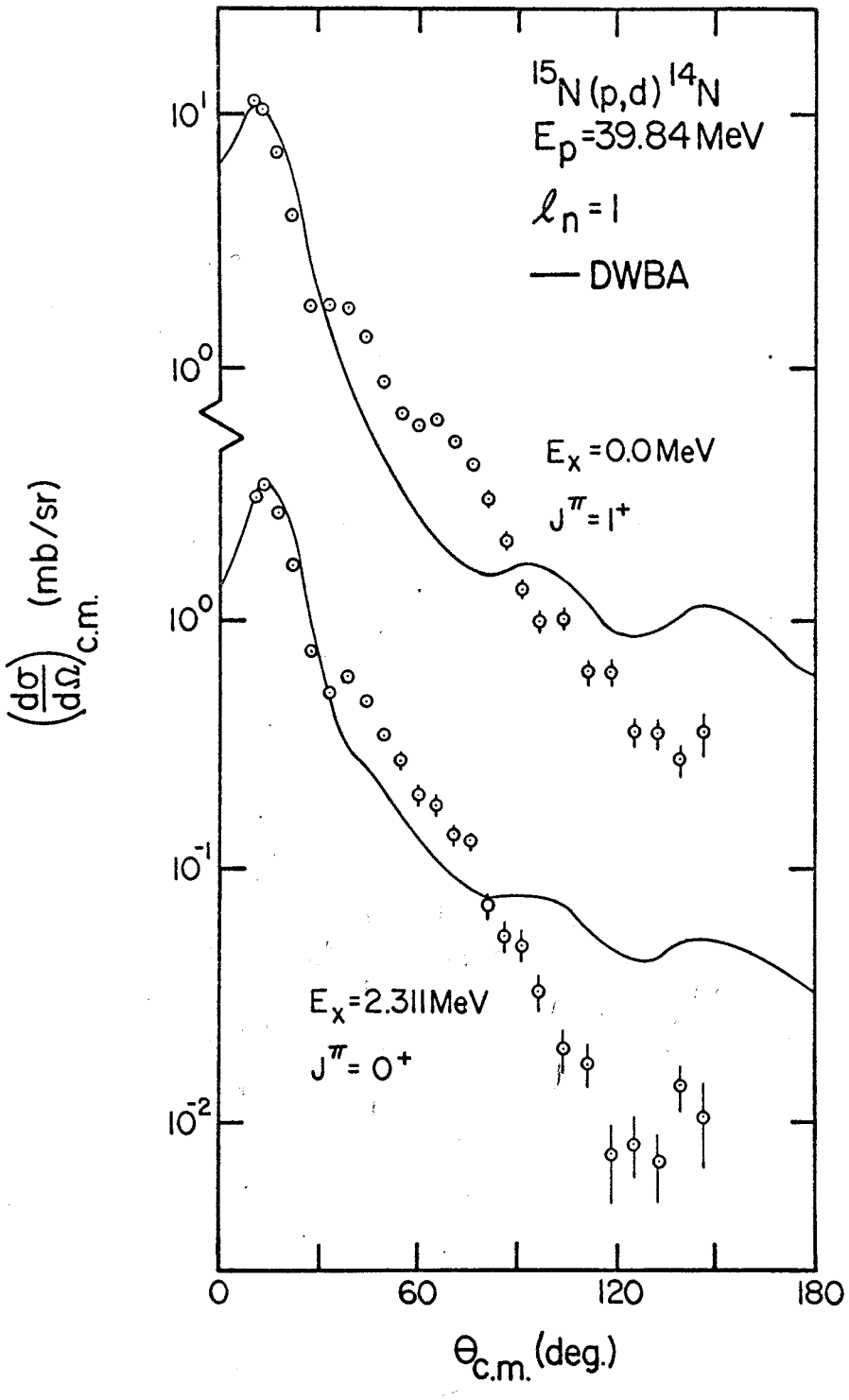

Figure VI-10. DWBA fits to the $^{15}N(p,d)^{14}N$, E_p=39.84 MeV, E_x=0.0 and 2.311 MeV angular distributions, assuming $1p_{1/2}$ neutron transfer.

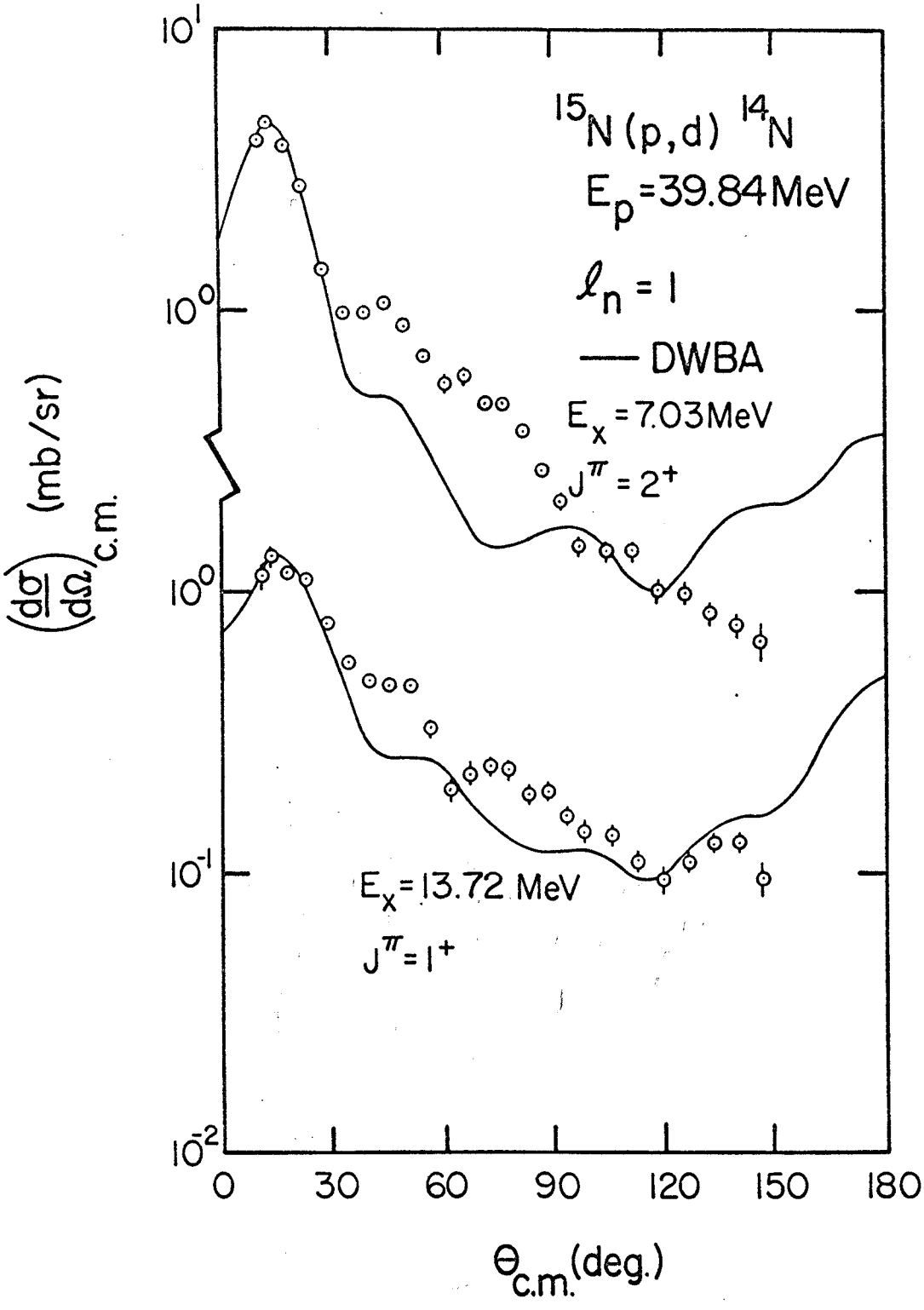

Figure VI-11. DWBA fits to the $^{15}N(p,d)^{14}N$, E_p=39.84 MeV, E_x=7.03 and 13.72 MeV angular distributions, assuming $1p_{3/2}$ neutron transfer.

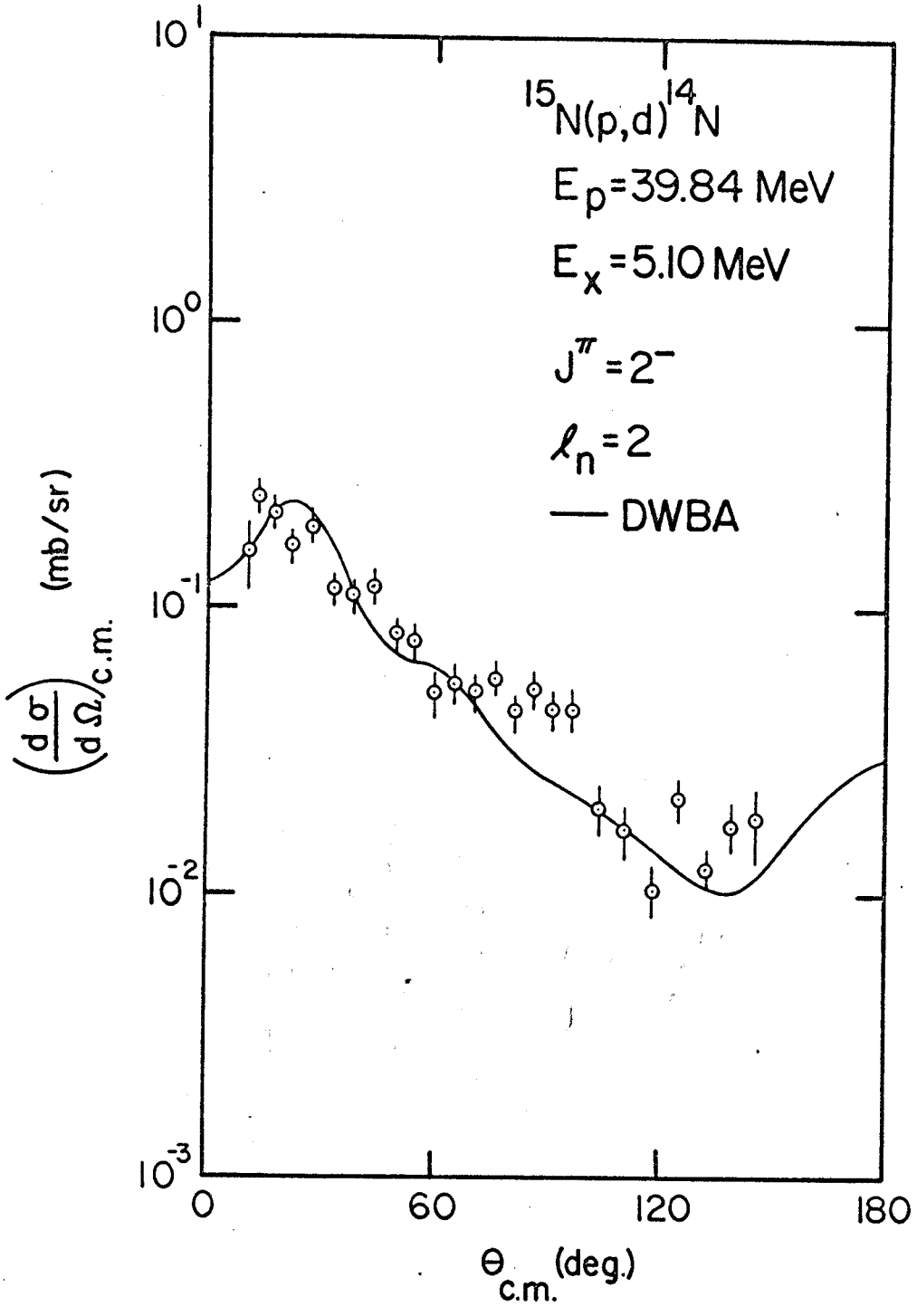

Figure VI-12. DWBA fit to the $^{15}N(p,d)^{14}N$, E_p=39.84 MeV, E_x=5.10 MeV angular distribution, assuming $1d_{5/2}$ neutron transfer.

Table VI-4. Peak cross sections and spectroscopic factors for the levels observed in ^{14}N. The average cross section over the indicated angular range is given for weak levels having angular distributions showing no characteristic maximum. The uncertainties quoted in the spectroscopic factors represent only the uncertainties in σ_{peak}.

E_x (MeV)	J^π	T	σ_{peak} (mb/sr)	θ_{peak} (deg)	S
0.0	1^+	0	11.1 ± 0.8	12 ± 1	1.27 ± 0.09
2.311	0^+	1	3.4 ± 0.2	14 ± 1	0.50 ± 0.03
3.945	1^+	0	3.3 ± 0.4	14 ± 1	0.60 ± 0.07
4.91	$(0)^-$	0	0.06 ± 0.02	12- -15	
5.10	2^-	0	0.22 ± 0.06	18 ± 2	0.06 ± 0.02
5.69	1^-	0	0.12 ± 0.03	12- -15	
5.83	3^-	0	0.15 ± 0.05	21 ± 3	0.04 ± 0.01
6.21	1^+	0	0.15 ± 0.04	15 ± 2	0.03 ± 0.01
6.44	3^+	0	0.01 ± 0.006	14- -34	
6.70			<0.01		
7.03	2^+	0	4.7 ± 0.3	15 ± 1	1.02 ± 0.07
7.40			0.02 ± 0.01	18 ± 3	
7.60			<0.01		
7.97	2^-	0	0.05 ± 0.02	15 ± 2	
8.06	1^-	1	0.06 ± 0.03	12- -15	
8.63	0^+	1	0.02 ± 0.01	21 ± 2	
8.91	3^-	(1)	0.04 ± 0.02	12- -29	
8.963	(5^+)	0			
8.98	2^+	0	0.05 ± 0.02	21 ± 2	
9.17	2^+	1	1.7 ± 0.2	15 ± 1	0.49 ± 0.06
9.388	$(2^-,3^-)$	0	0.12 ± 0.05	30 ± 3	0.05 ± 0.02
9.508	2^-	1	0.06 ± 0.02	9- -18	
9.71	1^+	0	<0.01	9- -45	
10.09	2^+	0	0.10 ± 0.03	16 ± 2	0.03 ± 0.01
10.43	2^+	1	1.16 ± 0.15	16 ± 1	0.39 ± 0.05
10.85	(4^+)	0	<0.01		
11.06	1^+	0	0.09 ± 0.03	16 ± 2	0.04 ± 0.01
11.23	3^-	1			
11.29	2^-	0	0.05 ± 0.03	15 ± 3	0.02 ± 0.01
11.39	(1^+)	0	0.02 ± 0.01	14- -24	

Table VI-4. (continued)

E_x (MeV)	J^π	T	σ_{peak} (mb/sr)	θ_{peak} (deg)	S
11.51	3^+		0.03 ± 0.01	30 ± 3	
11.66			0.05 ± 0.03	12 ± 3	
11.74	1^+	]			
11.80	(2^+)	]	0.03 ± 0.02	12- -40	
12.21	(3^-)	]			
12.29		]	0.01 ± 0.01	14- -25	
12.52			0.32 ± 0.05	24 ± 3	
12.61	3^+		0.06 ± 0.03	11- -23	
12.80	4^+	]			
12.83	4^-	]	0.07 ± 0.03	11- -30	
13.17	$(0^-,1^-)$	]			
13.23		]	0.15 ± 0.05	12- -15	
13.72	1^+	1	1.38 ± 0.1	15 ± 1	0.81 ± 0.06

the ^{15}N ground state appears to be similar to that in the ^{16}O ground state.

VI.B.2. Comparison to the Intermediate Coupling Theory

Comparisons of the experimental data to the intermediate coupling predictions of Cohen and Kurath are made in this section. This model and the method of computing spectroscopic factors from the coefficients of fractional parentage deduced from it were discussed in Chapter II. These predictions are given in Table VI-5; they show six strong levels below 12.0 MeV, with three weak levels lying quite a bit higher. Included in Table VI-5 are the spectroscopic factors expected in the jj-coupling limit. Pickup of a $1p_{1/2}$ neutron leads to states having configuration (a) in Fig. V-14, whereas $1p_{3/2}$ pickup leads to states having configuration (c). For a given configuration the predicted spectroscopic factor for 1p pickup leading to a state of angular momentum J is given by

$$S_{1j}(J_i) = n_{1j}(2J_i + 1)/\sum_k (2J_k + 1),$$

where n_{1j} is the number of $1p_j$ neutrons in the ground state configuration of ^{15}N. The summation is over all states J_k of a given configuration. The jj-coupling and intermediate coupling descriptions are very similar.

Table VI-5. Intermediate coupling predictions of coefficients of fractional parentage and spectroscopic factors for 1p neutron pickup from ^{15}N. Also included are the spectroscopic factors predicted in jj-coupling.

E(calc.) (MeV)	(J^π,T)	nℓj	CFP	$\sum_j CFP^2$	S	S_{jj}
0.0	$(1^+,0)$	$1p_{3/2}$	0.0542			
		$1p_{1/2}$	-0.3601	0.1326	1.459	1.500
2.690	$(0^+,1)$	$1p_{1/2}$	0.3376	0.1140	0.418	0.500
3.616	$(1^+,0)$	$1p_{3/2}$	0.2434			
		$1p_{1/2}$	0.0642	0.0633	0.696	0.750
6.991	$(2^+,0)$	$1p_{3/2}$	-0.3371	0.1136	1.250	1.250
9.524	$(2^+,1)$	$1p_{3/2}$	-0.5704	0.3255	1.192	1.250
11.783	$(1^+,1)$	$1p_{3/2}$	-0.4523			
		$1p_{1/2}$	0.0000	0.2046	0.750	0.750
15.238	$(1^+,0)$	$1p_{3/2}$	-0.0776			
		$1p_{1/2}$	-0.0505	0.0086	0.095	0.000
16.323	$(0^+,1)$	$1p_{1/2}$	0.1497	0.0224	0.082	0.000
17.879	$(2^+,1)$	$1p_{3/2}$	-0.1246	0.0155	0.057	0.000

A graphical comparison of the theoretical and experimental results is given in Fig. VI-13, where the lengths of the lines are proportional to the spectroscopic factors. The extensions of the theoretical lines represent the jj-coupling predictions. Seven strong levels were observed in the present experiment, all of which have angular distributions characteristic of ℓ_n=1 pickup, whereas the Cohen and Kurath calculations predict only six levels. It appears that the 1p strength in the 2^+, T=1 level predicted to be at 9.524 MeV is shared by the 2^+, T=1 level at 9.17 MeV and the 2^+, T=1 level at 10.43 MeV (Wa 60, Ka 61). The mixing of these levels is also supported by the values of the M1 transition strengths of the (9.17 MeV→0.0 MeV) and (10.43 MeV→0.0 MeV)transitions. Warburton and Pinkston (Wa 60) indicate that a single 2^+, T=1 level having a $(1s)^4(1p)^{10}$ configuration is allowed in the 10 MeV region (the one predicted by both jj-coupling and intermediate coupling). A 2^+, T=1 level having a $(1s)^4(1p)^8(1s)(1d)$ configuration is expected in the same region. The predictions for the relative M1 strengths for ground state transitions from these levels are ∿12 and 0, respectively. Since the observed M1 strengths for the 9.17 MeV and 10.43 MeV ground state transitions are 4.1 and 5.5, respectively, Warburton and Pinkston suggest that these two

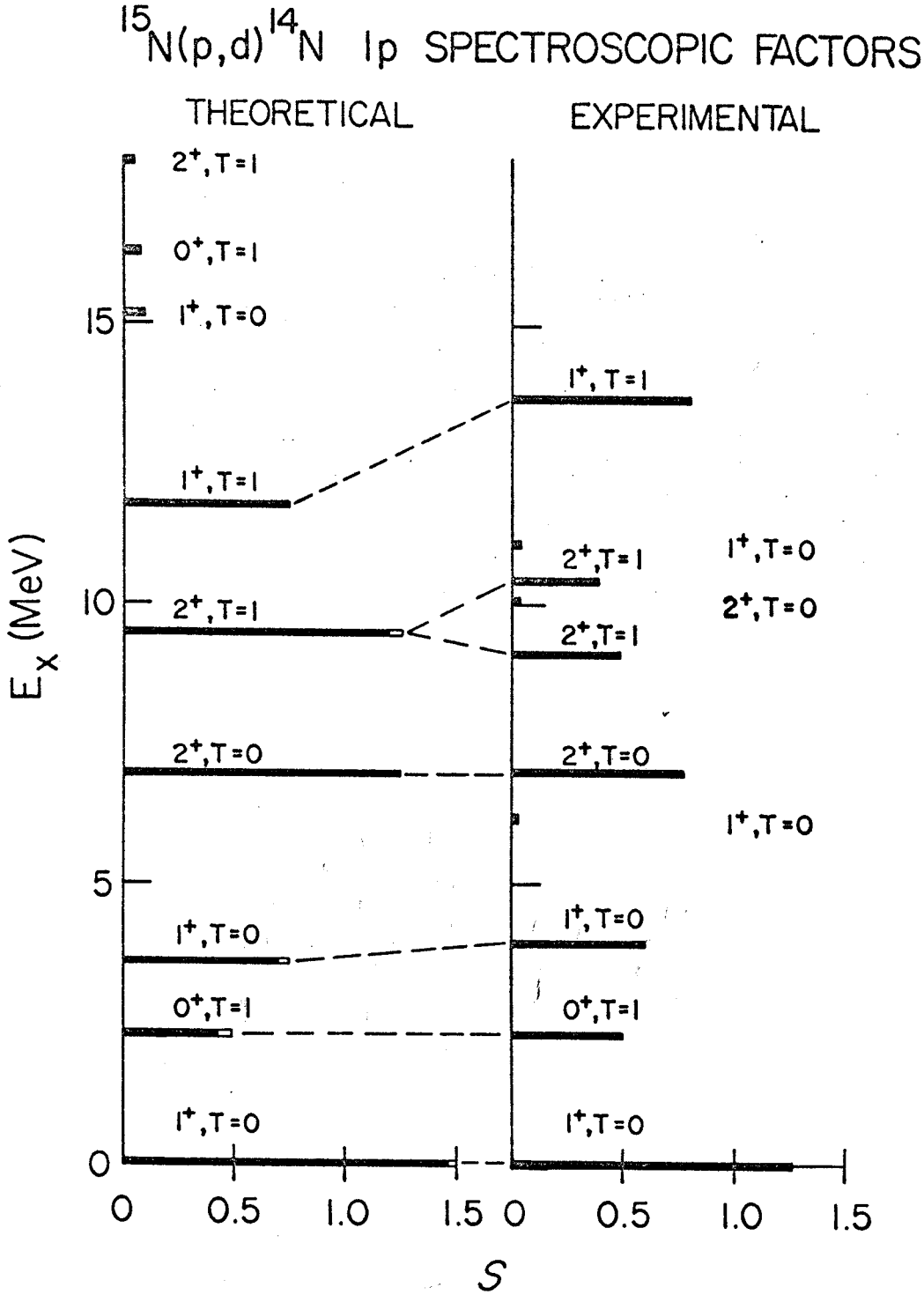

Figure VI-13. Theoretical and experimental ℓ_n=1 spectroscopic factors for the $^{15}N(p,d)^{14}N$ reaction. The solid theoretical bars are the intermediate coupling predictions of Cohen and Kurath (Co 67). Where different, the jj-coupling predictions for the six strong levels are represented by the open extensions of the bars.

levels are mixtures of the two configurations. The ratio of the $(1s)^4(1p)^{10}$ components of the two levels is given by the ratio of the M1 strengths, and can be obtained from the present work as the ratio of the 1p spectroscopic factors for these levels. The ratios are

$$[(1s)^4(1p)^{10}, (9.17 \text{ MeV})]/[(1s)^4(1p)^{10}, (10.43 \text{ MeV})] = 0.75$$

from the M1 strengths, and

$$[(1s)^4(1p)^{10}, (9.17 \text{ MeV})]/[(1s)^4(1p)^{10}, (10.43 \text{ MeV})] = 1.25 \pm 0.15$$

from the spectroscopic factors. Thus, both the work of Warburton and Pinkston and the present work suggest strong mixing of the two levels, but disagree somewhat about the division of 1p strength between them. The sum of the spectroscopic factors for the 9.17 and 10.43 MeV levels is slightly less than that predicted for the 9.524 MeV level, but the overall agreement is good. These data thus support the 2^+, T=1 assignments for the 9.17 and 10.43 MeV levels.

This leaves the predicted 1^+, T=1 level to correspond to the previously unassigned broad level observed at 13.72 MeV. The T=1 assignment for this level is consistent with the $^{12}C(\alpha,d)^{14}N$ data shown by Zafiratos et al. (Za 67), where no level of appreciable strength was observed in the 13.7

MeV region. The several weakly excited ℓ_n=1 levels observed in the present experiment probably result from small admixtures of the wavefunctions of the strong levels having the same J^π and T. No levels of measurable strength were observed above 13.72 MeV. The three weak levels predicted by Cohen and Kurath probably appear at much higher excitation energies and may be mixed with other levels. The strongest of these levels would be expected to have a peak cross section of only 50 μb/sr, and since the levels are well above the particle threshold and therefore expected to be broad, there would be little hope for being able to separate them from the background. The good overall agreement of the Cohen and Kurath intermediate coupling predictions and the experimental spectroscopic factors is further evidence for the validity of this model for 1p shell nuclei.

CHAPTER VII

SUMMARY AND CONCLUSIONS

This work has provided valuable information about the use of DWBA calculations in the extraction of spectroscopic factors for the (p,d) reaction on light nuclei. While it is not possible to provide a definite guide for performing meaningful calculations, the effects of variations of certain parameters of the calculation can be pointed out. The most immediately obvious problem, the inability of a straightforward DWBA calculation to reproduce the shape of the angular distribution, was treated by the use of a lower integration cutoff, rather than by changing the deuteron imaginary well depth, which resulted in too-large values of the extracted spectroscopic factors. The 3 F cutoff used was a maximum in the σ_{peak} vs R_{cutoff} curve and is close to the value of $1.2A^{1/3}$ for ^{16}O and ^{15}O. In addition to improving the shape of the distribution, the value of the spectroscopic factor became more reasonable.

The radius parameter of the bound state well (r_{on}) offers a special problem. This study indicates that the

value of the calculated peak cross section, and hence the spectroscopic factor, is a strong function of r_{on}. One should be aware of this problem in any attempt to extract absolute spectroscopic factors; however, relative spectroscopic factors appear to depend much less strongly on r_{on}. In the present work a value of r_{on} equal to the real proton well radius gave reasonable spectroscopic factors.

It also was found that the energy dependence of the peak ℓ_n=1 cross sections for the two strongly excited levels of ^{15}O was not reproduced for a deuteron energy in the center-of-mass frame of less than 22 MeV. Thus, if a (p,d) reaction on a light nucleus is to be performed at a single energy, the proton energy should be as high as practicable. In the ^{16}O experiment some of the difficulties with the 25 MeV data could be due to the resonance structure observed by Cameron et al. (Ca 68) in the p-^{16}O system below 30 MeV. The relative spectroscopic factors showed much less energy dependence than the absolute spectroscopic factors. The use of a method to eliminate some of the Q-dependence in the relative spectroscopic factors did not result in any significant improvement and indicates that the problems involved are probably not in the deuteron channel. It may instead be that the high penetrability of the proton is not well-accounted-for in the DWBA calculation.

The spectroscopic factors extracted from the 45.34 MeV $^{16}O(p,d)^{15}O$ data indicate that at least 30% of the $1p_{3/2}$ strength is missing from the 6.18 MeV, $3/2^-$ level, which disagrees with previous work (Ba 64, Wa 65a). Approximately 12% of this missing strength is contained in the 9.60 MeV, $3/2^-$ and 10.46 MeV ($3/2^-$, $1/2^-$) levels, the latter assignment being made on the basis of the shape of the angular distribution. The 8.98 MeV, $3/2^-$ level contains less than 1% of the $1p_{3/2}$ strength. The remaining strength may reside in many highly fragmented states in the 20 MeV region of excitation (Be 68). Small 2s-1d admixtures and a possible $1g_{7/2}$ admixture were observed in the ground state of ^{16}O.

The spectroscopic factors from the $^{15}N(p,d)^{14}N$ data were found to agree very well with the intermediate coupling calculations of Cohen and Kurath. The 2^+, T=1 levels at 9.17 and 10.43 MeV both appear to contain large mixtures of the $(1s)^4(1p)^{10}$ configuration. The intermediate coupling predictions have been used to assign values of $J^\pi=1^+$ and T=1 to the 13.72 MeV level. The high degree of agreement between the experimental data and the theoretical predictions in the case of $^{15}N(p,d)^{14}N$ strikes an encouraging note about the present state of our understanding of nuclear structure.

APPENDIX A

TABULATION OF $^{16}O(p,p)^{16}O$ AND $^{16}O(p,d)^{15}O$ DIFFERENTIAL CROSS SECTIONS

The following pages contain listings of the laboratory and center-of-mass differential cross sections with the corresponding statistical and total errors for the elastic scattering of protons from ^{16}O and for the levels of ^{15}O strongly excited in the $^{16}O(p,d)^{15}O$ reaction for various proton energies between 21.27 and 45.34 MeV. A discussion of the estimated errors is found in Chapter III (Section III.E.). The values of the cross sections are to be read as

$$2.139E+03 \equiv 2.139 \times 10^{3}.$$

16O(P,P)16O EP = 25.46 MEV EX = 0.000 MEV

LAB ANGLE (DEG)	LAB CROSS SECTION (MB/SR)	C.M. ANGLE (DEG)	C.M. CROSS SECTION (MB/SR)	STAT. ERROR (PERCENT)	TOT. ERROR (PERCENT)
10.0	2.130E+03	11.6	1.891E+03	0.3	3.4
11.1	1.486E+03	15.0	1.316E+03	0.3	3.2
12.0	1.013E+03	20.2	8.906E+02	0.5	3.1
21.1	6.479E+02	25.6	5.869E+02	0.3	3.0
23.1	3.401E+02	30.9	3.228E+02	0.4	3.0
34.1	1.760E+02	36.2	1.587E+02	0.9	3.1
39.0	7.494E+01	41.3	6.800E+01	1.5	3.3
44.0	3.238E+01	46.6	2.957E+01	1.7	3.4
49.0	2.365E+01	51.7	2.170E+01	2.2	3.6
53.9	1.755E+01	56.9	2.560E+01	1.5	3.2
58.8	2.903E+01	62.0	3.001E+01	1.4	3.2
63.8	2.999E+01	66.1	2.834E+01	1.7	3.4
68.8	2.132E+01	67.3	2.074E+01	1.4	3.2
68.8	2.750E+01	72.5	2.639E+01	1.7	3.4
73.8	1.277E+01	77.5	1.213E+01	2.2	3.6
78.8	1.430E+01	82.5	1.406E+01	2.5	3.8
83.8	7.631E+00	87.6	8.539E+00	3.0	4.2
88.8	5.135E+00	92.5	5.132E+00	3.2	4.4
93.8	3.909E+00	97.6	3.938E+00	4.4	5.4
98.8	2.941E+00	102.7	2.991E+00	4.7	5.6
103.8	1.953E+00	107.5	1.640E+00	5.8	6.7
108.8	1.134E+00	112.5	1.248E+00	5.8	7.7
113.8	7.155E-01	117.2	8.645E-01	7.7	8.8
118.7	6.816E-01	121.9	6.949E-01	7.9	9.0
123.7	6.131E-01	127.7	6.621E-01	7.5	8.6
128.7	1.591E-01	132.5	1.048E+00	5.7	6.7
133.7	1.407E+00	142.1	1.657E+00	4.7	5.7
143.7	1.474E+00	149.7	1.873E+00	4.7	5.7
153.8	1.562E+00	157.3	1.764E+00	4.6	5.6
163.8	1.136E+00	164.5	1.291E+00	4.3	5.5

16O(P,P)16O EP = 32.37 MEV EX = 0.000 MEV

LAB ANGLE (DEG)	LAB CROSS SECTION (MB/SR)	C.M. ANGLE (DEG)	C.M. CROSS SECTION (MB/SR)	STAT. ERROR (PERCENT)	TOT. ERROR (PERCENT)
1.•1	1.•58E+03	10.•6	1.637E+03	0.2	3.5
1.•1	1.•67E+03	16.1	1.122E+03	0.4	3.2
2.•1	•.•2E+02	21.4	7.844E+02	0.4	3.0
2.•1	•.13E+02	26.7	4.584E+02	0.4	3.0
2.•2	1.•2E+02	26.3	4.638E+02	0.4	3.0
3.•1	2.•3E+02	32.0	2.326E+02	0.5	3.0
3.•2	1.•4E+02	37.3	9.999E+01	0.7	3.0
4.•1	4.•3E+01	42.6	4.299E+01	1.3	3.2
4.•1	•.•2E+01	47.7	2.460E+01	1.3	3.2
5.•0	2.•1E+01	52.9	2.307E+01	1.5	3.3
5.•0	2.•3E+01	58.0	2.354E+01	1.5	3.3
5.•0	2.•1E+01	63.0	2.514E+01	1.5	3.2
5.•0	•.•2E+01	68.1	2.277E+01	1.6	3.3
6.•0	•.•3E+01	68.4	1.046E+01	1.8	3.4
7.•0	1.•6E+01	73.5	1.402E+01	2.0	3.5
7.•0	1.•4E+01	78.6	9.602E+00	2.0	3.5
8.•0	•.•0E+00	84.7	5.198E+00	2.8	4.1
8.•0	•.•4E+00	90.6	3.423E+00	3.3	4.4
9.•0	•.•7E+00	96.7	2.075E+00	4.3	5.3
10.•0	1.•4E+00	103.7	1.484E+00	5.1	6.0
10.•0	1.•3E+00	110.6	1.049E+00	5.2	6.2
11.•0	•.•3E-01	117.3	7.330E-01	6.1	7.0
12.•0	•.•2E-01	124.0	4.279E-01	6.2	7.0
12.•0	3.•1E-01	130.7	3.038E-01	6.5	7.4
13.•0	4.•4E-01	137.4	5.331E-01	5.4	6.3
14.•0	•.•4E-01	144.1	7.277E-01	4.8	5.7
14.•0	7.•2E-01	150.7	7.990E-01	4.4	5.4
15.•0	•.•3E-01	157.4	7.495E-01	4.0	5.0
16.•0	4.•2E-01	164.0	4.689E-01	4.3	5.4
17.•0	1.•5E-01	170.6	2.225E-01	4.3	6.1

160(P,P)160 EP = 35.20 MEV EX = 0.000 MEV

LAB ANGLE (DEG)	LAB CROSS SECTION (MB/SR)	C.M. ANGLE (DEG)	C.M. CROSS SECTION (MB/SR)	STAT. ERROR (PERCENT)	TOT. ERROR (PERCENT)
12.3	1.665E+03	11.0	1.471E+03	0.5	3.5
16.4	1.208E+03	16.4	1.067E+03	0.5	3.2
21.3	8.476E+02	21.6	7.629E+02	0.4	3.0
26.4	4.498E+02	27.0	4.013E+02	0.4	3.0
31.3	2.111E+02	32.2	1.893E+02	0.5	3.0
36.4	8.578E+01	37.6	7.735E+01	0.8	3.0
41.4	3.431E+01	42.8	3.098E+01	1.1	3.1
46.4	2.384E+01	48.1	2.182E+01	1.5	3.3
51.3	2.294E+01	53.2	2.119E+01	1.6	3.3
56.6	2.389E+01	59.6	2.213E+01	1.0	3.1
61.2	2.299E+01	64.3	2.135E+01	1.6	3.3
65.2	1.977E+01	68.4	1.858E+01	1.5	3.3
69.2	1.509E+01	73.6	1.429E+01	2.4	3.7
76.2	9.995E+00	78.7	9.490E+00	2.6	3.9
79.2	6.056E+00	84.8	5.773E+00	2.9	4.1
81.2	3.288E+00	94.9	3.230E+00	3.1	4.3
87.1	2.064E+00	90.8	2.059E+00	3.2	4.3
93.2	1.503E+00	96.9	1.518E+00	3.6	4.6
98.3	1.230E+00	103.0	1.259E+00	3.2	4.3
104.2	9.131E-01	108.8	9.471E-01	4.2	5.2
110.1	4.777E-01	115.6	5.030E-01	4.7	5.7
116.0	2.472E-01	122.3	2.641E-01	5.4	6.3
122.5	1.644E-01	125.6	1.778E-01	6.7	7.7
126.0	1.793E-01	130.0	1.940E-01	6.2	7.0
130.6	2.252E-01	132.4	2.452E-01	6.0	6.9
136.0	3.081E-01	135.7	3.378E-01	4.9	5.8
142.0	4.552E-01	142.4	5.047E-01	4.8	5.7
147.0	5.290E-01	148.0	5.922E-01	3.7	4.3
154.0	4.707E-01	155.6	5.314E-01	3.7	4.3
161.2	3.251E-01	162.4	3.692E-01	3.7	4.8
166.1	2.336E-01	167.0	2.661E-01	4.1	5.3
171.2	1.418E-01	171.8	1.620E-01	4.2	5.8

160(P,P)160 EP = 38.43 MEV EX = 0.000 MEV

LAB ANGLE (D_2O)	LAB CROSS SECTION (MB/SR)	C.M. ANGLE (DEG)	C.M. CROSS SECTION (MB/SR)	STAT. ERROR (PERCENT)	TOT. ERROR (PERCENT)
[illegible]	1.570E+03	10.2	1.386E+03	0.4	3.6
14.6	1.277E+03	15.5	1.123E+03	0.3	3.2
19.6	8.554E+02	20.9	7.592E+02	0.6	3.1
24.6	4.761E+02	26.2	4.243E+02	0.4	3.0
29.6	2.119E+02	31.5	1.898E+02	0.6	3.0
34.6	8.428E+01	36.7	7.592E+01	1.1	3.1
39.6	3.380E+01	42.0	3.069E+01	1.2	3.2
44.6	2.104E+01	47.2	2.005E+01	1.6	3.3
49.5	2.458E+01	52.3	1.892E+01	2.0	3.5
54.4	1.888E+01	57.4	1.814E+01	1.8	3.4
59.4	1.554E+01	62.6	1.458E+01	2.0	3.5
64.5	1.114E+01	67.9	1.056E+01	2.6	3.9
69.5	6.309E+00	73.0	6.513E+00	2.8	4.1
74.5	4.021E+00	78.1	3.892E+00	3.1	4.3
81.5	2.26+E+00	84.2	2.221E+00	4.5	5.4
86.5	1.479E+00	90.2	1.489E+00	5.0	6.0
94.5	1.181E+00	96.2	1.191E+00	5.0	5.9
99.5	9.259E-01	103.2	9.506E-01	5.1	5.9
109.5	5.456E-01	110.1	6.093E-01	6.1	7.1
119.4	2.456E-01	116.8	3.016E-01	6.6	7.2
129.3	1.217E-01	122.5	1.303E-01	9.7	10.1
134.3	1.054E-01	130.3	1.146E-01	9.6	10.0
139.3	1.133E-01	137.0	2.014E-01	9.6	10.0
144.3	2.265E-01	143.6	3.294E-01	7.3	8.0
149.3	3.324E-01	150.3	3.730E-01	6.4	7.2
154.4	3.293E-01	157.0	3.722E-01	5.8	6.6
164.4	2.374E-01	163.6	2.585E-01	5.2	6.2

16O(P,P)16O EP = 45.13 MEV EX = 0.000 MEV

LAB ANGLE (DEG)	LAB CROSS SECTION (MB/SR)	C.M. ANGLE (DEG)	C.M. CROSS SECTION (MB/SR)	STAT. ERROR (PERCENT)	TOT. ERROR (PERCENT)
10.0	1.438E+03	10.7	1.269E+03	0.4	3.5
15.0	1.141E+03	16.0	1.009E+03	0.5	3.2
20.0	6.954E+02	21.3	6.169E+02	0.6	3.1
25.0	3.452E+02	26.6	3.075E+02	0.7	3.0
30.0	1.401E+02	31.9	1.254E+02	1.6	3.3
35.0	4.989E+01	37.2	4.495E+01	1.5	3.3
40.0	2.052E+01	42.4	1.861E+01	1.9	3.5
45.0	1.678E+01	47.7	1.534E+01	2.3	3.7
49.9	1.534E+01	52.8	1.414E+01	2.2	3.7
54.8	1.285E+01	57.9	1.194E+01	2.5	3.8
59.8	9.169E+00	63.1	8.605E+00	2.6	3.9
64.9	5.261E+00	68.3	4.989E+00	3.2	4.4
69.9	2.948E+00	73.4	2.825E+00	3.7	4.7
74.9	1.586E+00	78.5	1.537E+00	4.6	5.5
79.9	1.171E+00	83.6	1.147E+00	5.8	6.5
85.8	1.002E+00	89.6	9.944E-01	16.3	16.5
92.9	5.638E-01	96.7	5.689E-01	8.1	8.7
99.9	3.953E-01	103.6	4.053E-01	8.0	8.6
106.9	1.725E-01	110.5	1.797E-01	9.7	10.3
113.8	5.772E-02	117.2	6.103E-02	10.4	11.2
120.7	2.586E-02	123.9	2.773E-02	13.2	14.5
127.7	5.147E-02	130.7	5.595E-02	10.1	10.7
134.7	9.598E-02	137.4	1.056E-01	8.5	9.1
141.7	1.164E-01	144.0	1.295E-01	7.6	8.1
148.7	1.122E-01	150.7	1.260E-01	6.7	7.4
155.8	1.344E-01	157.3	1.521E-01	6.8	7.6
162.8	9.517E-02	163.9	1.083E-01	8.2	9.1

169(P,D)150 EP = 21.27 MEV EX = 0.000 MEV

LAB ANGLE (DEG)	LAB CROSS SECTION (MB/SR)	C.M. ANGLE (DEG)	C.M. CROSS SECTION (MB/SR)	STAT. ERROR (PERCENT)	TOT. ERROR (PERCENT)
10.5	2.463E+00	12.2	1.833E+00	5.1	8.5
15.1	2.834E+00	17.5	2.121E+00	2.1	3.9
17.7	2.814E+00	20.5	2.114E+00	2.1	3.7
20.0	2.758E+00	23.2	2.080E+00	1.9	3.6
25.0	1.988E+00	28.9	1.514E+00	2.6	4.0
30.0	1.314E+00	34.6	1.013E+00	3.2	4.3
35.1	9.775E-01	40.4	7.648E-01	4.1	5.0
40.1	9.080E-01	46.1	7.220E-01	4.3	5.1
50.0	1.084E+00	57.1	8.950E-01	6.0	6.7
59.9	8.583E-01	68.0	7.405E-01	8.0	8.5

16O(P,D)15O EP = 25.52 MEV EX = 0.000 MEV

LAB ANGLE (DEG)	LAB CROSS SECTION (MB/SR)	C.M. ANGLE (DEG)	C.M. CROSS SECTION (MB/SR)	STAT. ERROR (PERCENT)	TOT. ERROR (PERCENT)
12.0	8.130E+00	13.7	6.290E+00	2.0	3.9
14.0	8.390E+00	15.9	6.504E+00	2.1	3.8
16.0	8.726E+00	18.2	6.780E+00	1.9	3.6
18.0	8.252E+00	20.5	6.429E+00	1.8	3.5
20.0	7.645E+00	22.7	5.974E+00	2.0	3.6
22.0	6.227E+00	25.0	4.882E+00	2.0	3.6
25.0	4.347E+00	28.4	3.427E+00	4.8	5.6
30.0	1.846E+00	34.0	1.471E+00	4.8	5.6
35.0	6.870E-01	39.6	5.542E-01	4.9	5.7
40.0	7.656E-01	45.2	6.264E-01	3.8	4.8
46.6	1.316E+00	52.4	1.100E+00	3.3	4.3
51.4	1.428E+00	57.7	1.214E+00	3.1	4.2
56.3	1.365E+00	63.0	1.183E+00	3.2	4.3
61.3	1.039E+00	68.4	9.179E-01	3.7	4.6
68.9	5.606E-01	76.4	5.120E-01	5.7	6.4
76.5	4.171E-01	84.3	3.946E-01	6.3	6.9
83.9	4.708E-01	91.9	4.615E-01	5.0	5.8
93.8	4.641E-01	101.8	4.776E-01	6.5	7.1
103.9	4.421E-01	111.7	4.782E-01	6.7	7.3
113.9	3.194E-01	121.3	3.623E-01	7.7	8.3
123.8	2.494E-01	130.5	2.957E-01	8.4	8.8
133.7	2.240E-01	139.5	2.762E-01	8.2	8.7
143.7	1.910E-01	148.5	2.437E-01	6.8	7.4
153.8	1.906E-01	157.3	2.499E-01	8.7	9.5
163.3	2.805E-01	165.6	3.745E-01	6.5	7.4

169(P,D)159 EP = 25.52 MEV EX = 6.180 MEV

LAB ANGLE (DEG)	LAB CROSS SECTION (MB/SR)	C.M. ANGLE (DEG)	C.M. CROSS SECTION (MB/SR)	STAT. ERROR (PERCENT)	TOT. ERROR (PERCENT)
12.0	3.142E+00	14.6	2.139E+00	3.3	4.7
14.0	3.151E+00	17.0	2.151E+00	3.5	4.7
16.0	3.271E+00	19.4	2.241E+00	3.2	4.5
18.0	3.180E+00	21.9	2.187E+00	2.9	4.2
20.0	3.080E+00	24.3	2.128E+00	3.1	4.3
22.0	3.012E+00	26.7	2.091E+00	3.0	4.2
25.0	2.994E+00	30.3	2.096E+00	5.8	6.5
30.0	2.612E+00	36.2	1.858E+00	4.1	5.0
35.0	2.330E+00	42.2	1.688E+00	2.7	3.9
40.0	1.997E+00	48.0	1.478E+00	2.3	3.7
46.6	1.683E+00	55.7	1.286E+00	2.9	4.1
51.4	1.273E+00	61.2	9.986E-01	3.3	4.3
56.3	1.042E+00	66.7	8.405E-01	3.7	4.7
61.3	7.855E-01	72.3	6.539E-01	4.3	5.2
66.9	3.455E-01	80.6	3.026E-01	7.3	7.8

$^{16}O(P,D)^{15}O$ EP = 31.82 MEV EX = 0.000 MEV

LAB ANGLE (DEG)	LAB CROSS SECTION (MB/SR)	C.M. ANGLE (DEG)	C.M. CROSS SECTION (MB/SR)	STAT. ERROR (PERCENT)	TOT. ERROR (PERCENT)
10.1	1.007E+01	11.4	7.972E+00	2.9	4.5
15.1	1.030E+01	17.0	8.193E+00	2.6	4.1
20.1	6.773E+00	22.6	5.422E+00	2.9	4.2
25.1	2.662E+00	28.2	2.148E+00	2.6	3.9
30.1	1.200E+00	33.7	9.773E-01	3.7	4.7
35.1	1.592E+00	39.2	1.312E+00	3.6	4.6
45.1	2.231E+00	50.2	1.889E+00	3.3	4.3
50.0	1.736E+00	55.5	1.493E+00	3.7	4.7
59.9	7.784E-01	66.1	6.925E-01	5.8	6.4
70.0	8.061E-01	76.8	7.459E-01	4.7	5.6
80.0	9.105E-01	87.1	8.786E-01	4.0	4.9
89.9	6.561E-01	97.1	6.611E-01	4.5	5.3
105.0	1.903E-01	112.0	2.049E-01	8.0	8.5
119.8	1.285E-01	126.1	1.472E-01	6.9	7.5
129.8	1.239E-01	135.3	1.473E-01	6.7	7.3
139.8	1.584E-01	144.4	1.946E-01	6.3	6.9
149.8	2.023E-01	153.4	2.552E-01	4.8	5.6
160.0	2.504E-01	162.5	3.222E-01	3.7	4.8

160(P,D)159 EP = 31.62 MEV EX = 6.180 MEV

LAB ANGLE (DEG)	LAB CROSS SECTION (MB/SR)	C.M. ANGLE (DEG)	C.M. CROSS SECTION (MB/SR)	STAT. ERROR (PERCENT)	TOT. ERROR (PERCENT)
10.1	5.610E+00	11.7	4.197E+00	3.9	5.3
15.1	6.003E+00	17.5	4.517E+00	3.4	4.7
20.1	5.166E+00	23.2	3.917E+00	3.4	4.6
25.1	3.800E+00	29.0	2.910E+00	2.2	3.7
30.1	2.905E+00	34.7	2.251E+00	2.4	3.8
35.1	2.441E+00	40.3	1.918E+00	2.9	4.1
45.1	2.238E+00	51.6	1.820E+00	3.3	4.4
50.0	1.793E+00	57.0	1.490E+00	3.7	4.6
59.9	1.101E+00	67.8	9.525E-01	4.9	5.8
70.0	7.462E-01	78.6	6.783E-01	4.9	5.8
80.0	7.673E-01	89.0	7.353E-01	4.5	5.4
89.9	6.574E-01	99.0	6.656E-01	4.6	5.5
105.0	3.336E-01	113.8	3.675E-01	6.1	6.8

169(P,D)158 EP = 38.63 MEV EX = 0.000 MEV

LAB ANGLE (DEG)	LAB CROSS SECTION (MB/SR)	C.M. ANGLE (DEG)	C.M. CROSS SECTION (MB/SR)	STAT. ERROR (PERCENT)	TOT. ERROR (PERCENT)
9.8	1.126E+01	11.0	9.039E+00	2.7	4.3
12.3	1.197E+01	13.7	9.627E+00	4.2	5.3
14.8	1.095E+01	16.5	8.821E+00	4.0	5.0
19.8	6.568E+00	22.1	5.324E+00	3.2	4.3
23.3	1.905E+00	28.2	1.557E+00	4.1	5.2
30.3	1.970E+00	33.7	1.625E+00	5.6	6.3
35.3	2.239E+00	39.2	1.867E+00	3.8	4.8
40.3	2.352E+00	44.7	1.985E+00	3.6	4.6
45.3	1.856E+00	50.1	1.587E+00	3.8	4.8
50.2	1.207E+00	55.4	1.048E+00	4.5	5.3
55.1	9.932E-01	60.7	8.752E-01	4.4	5.2
60.1	7.923E-01	66.0	7.102E-01	5.0	5.8
70.3	7.034E-01	76.7	6.544E-01	3.4	4.4
75.2	5.160E-01	81.7	4.901E-01	6.4	7.0
80.3	4.140E-01	87.0	4.007E-01	5.0	5.7
90.2	2.189E-01	97.0	2.207E-01	6.1	6.8
97.2	1.337E-01	103.9	1.388E-01	12.4	12.7
105.3	8.008E-02	111.8	8.591E-02	10.1	10.4
112.2	5.197E-02	118.5	5.731E-02	19.6	19.9
120.1	5.825E-02	126.0	6.619E-02	10.5	10.9
130.1	5.242E-02	135.3	6.168E-02	10.2	10.5
140.1	4.761E-02	144.4	5.774E-02	10.1	10.4
150.1	6.397E-02	153.5	7.951E-02	7.8	8.3
160.3	6.531E-02	162.6	8.269E-02	6.2	6.9

16O(P,D)15O EP = 38.63 MEV EX = 6.180 MEV

LAB ANGLE (DEG)	LAB CROSS SECTION (MB/SR)	C.M. ANGLE (DEG)	C.M. CROSS SECTION (MB/SR)	STAT. ERROR (PERCENT)	TOT. ERROR (PERCENT)
9.8	8.710E+00	11.1	6.760E+00	3.0	4.5
11.3	8.391E+00	12.8	6.513E+00	3.7	5.0
12.3	9.343E+00	14.0	7.259E+00	4.7	5.7
13.3	9.297E+00	15.1	7.230E+00	3.0	4.4
14.8	9.702E+00	16.8	7.558E+00	4.3	5.2
15.3	1.008E+01	17.4	7.853E+00	2.9	4.3
17.8	8.196E+00	20.2	6.409E+00	3.0	4.3
19.8	7.130E+00	22.5	5.591E+00	3.1	4.2
20.3	8.165E+00	23.0	6.408E+00	3.2	4.4
25.3	3.621E+00	28.7	2.866E+00	3.0	4.2
30.3	2.807E+00	34.3	2.246E+00	4.7	5.5
35.3	2.330E+00	39.9	1.887E+00	3.7	4.7
40.3	2.334E+00	45.4	1.918E+00	3.7	4.7
45.3	2.060E+00	50.9	1.719E+00	3.6	4.7
50.2	1.532E+00	56.3	1.300E+00	4.0	5.0
55.1	1.232E+00	61.6	1.064E+00	4.0	4.9
60.1	9.777E-01	67.0	8.616E-01	4.6	5.5
60.2	9.757E-01	67.1	8.602E-01	2.8	4.0
70.3	8.569E-01	77.8	7.887E-01	3.1	4.2
75.2	7.795E-01	82.9	7.336E-01	5.3	6.1
80.3	6.347E-01	88.1	6.117E-01	4.0	5.0
90.2	4.026E-01	98.1	4.070E-01	4.5	5.5
97.2	3.704E-01	105.1	3.873E-01	7.6	8.2
105.3	3.316E-01	112.9	3.606E-01	4.9	5.7
112.2	2.969E-01	119.5	3.334E-01	8.9	9.4
120.1	2.621E-01	126.9	3.050E-01	5.0	5.8
130.1	2.486E-01	136.1	3.013E-01	4.7	5.5
140.1	1.832E-01	145.2	2.302E-01	5.2	6.0
150.1	1.433E-01	154.0	1.854E-01	5.2	6.0
160.3	2.342E-01	163.0	3.095E-01	3.3	4.5

169(P,D)158 EP = 45.34 MEV EX = 0.000 MEV

LAB ANGLE (DEG)	LAB CROSS SECTION (MB/SR)	C.M. ANGLE (DEG)	C.M. CROSS SECTION (MB/SR)	STAT. ERROR (PERCENT)	TOT. ERROR (PERCENT)
8.2	1.250E+01	9.1	1.010E+01	1.6	4.1
10.1	1.448E+01	11.2	1.172E+01	1.9	3.9
12.6	1.317E+01	14.0	1.067E+01	1.6	3.6
15.1	1.096E+01	16.8	8.905E+00	1.4	3.4
20.1	5.675E+00	22.3	4.636E+00	1.6	3.4
25.1	2.826E+00	27.9	2.326E+00	3.4	4.5
30.1	2.244E+00	33.4	1.862E+00	3.4	4.4
35.1	2.206E+00	38.8	1.850E+00	4.5	5.3
40.2	2.021E+00	44.4	1.715E+00	3.2	4.3
45.1	1.416E+00	49.7	1.218E+00	4.3	5.1
50.1	9.338E-01	55.1	8.140E-01	5.8	6.4
55.9	8.055E-01	61.3	7.148E-01	6.0	6.6
61.9	6.630E-01	67.7	6.002E-01	6.8	7.3
68.0	5.166E-01	74.0	4.778E-01	7.6	8.1
75.0	3.344E-01	81.3	3.174E-01	8.7	9.1
82.0	1.155E-01	88.5	1.126E-01	27.3	27.5
89.9	9.963E-02	96.4	1.003E-01	13.7	14.0
95.0	8.099E-02	104.5	8.418E-02	20.4	20.6
108.0	3.453E-02	114.2	3.733E-02	14.1	14.4
118.0	2.970E-02	123.7	3.332E-02	15.2	15.5
127.8	1.446E-02	132.9	1.678E-02	20.4	20.6
137.8	1.765E-02	142.2	2.111E-02	17.4	17.6
147.8	1.935E-02	151.3	2.373E-02	14.4	14.7
158.0	2.004E-02	160.4	2.505E-02	11.4	11.8

16O(P,D)15O EP = 45.34 MEV EX = (5.188 - 5.240) MEV

LAB ANGLE (DEG)	LAB CROSS SECTION (MB/SR)	C.M. ANGLE (DEG)	C.M. CROSS SECTION (MB/SR)	STAT. ERROR (PERCENT)	TOT. ERROR (PERCENT)
6.2	1.023E+00	9.2	8.100E-01	7.0	10.2
10.1	8.021E-01	11.4	6.358E-01	9.2	11.5
12.6	6.062E-01	14.2	4.815E-01	8.3	10.2
15.1	5.062E-01	17.0	4.030E-01	8.0	10.5
20.1	6.096E-01	22.6	4.884E-01	5.2	6.4
25.1	5.218E-01	28.1	4.214E-01	8.2	8.8
30.1	4.472E-01	33.7	3.647E-01	7.6	8.2
35.1	3.267E-01	39.2	2.694E-01	11.9	12.3
40.2	2.828E-01	44.8	2.362E-01	8.8	9.6
45.1	3.176E-01	50.2	2.690E-01	9.3	10.0
50.1	2.072E-01	55.6	1.782E-01	12.4	12.8
55.9	1.314E-01	61.8	1.153E-01	14.7	15.0
61.9	1.125E-01	68.2	1.009E-01	16.4	16.7
68.0	1.217E-01	74.7	1.118E-01	15.6	15.9
75.0	9.304E-02	81.9	9.264E-02	16.8	17.5
82.0	7.667E-02	89.1	7.463E-02	32.9	33.0
89.9	6.016E-02	97.1	6.062E-02	17.7	17.9
98.0	4.387E-02	105.1	4.581E-02	27.7	27.9
106.0	3.177E-02	114.8	3.465E-02	15.1	15.5
118.0	2.763E-02	124.3	3.140E-02	15.8	16.1
127.8	1.867E-02	133.5	2.203E-02	18.0	18.2
137.8	2.460E-02	142.6	3.000E-02	15.1	15.5
147.8	2.540E-02	151.6	3.185E-02	12.8	13.2
158.0	3.957E-02	160.7	5.069E-02	8.1	8.7

16O(P,D)15O EP = 45.34 MEV EX = 6.180 MEV

LAB ANGLE (DEG)	LAB CROSS SECTION (MB/SR)	C.M. ANGLE (DEG)	C.M. CROSS SECTION (MB/SR)	STAT. ERROR (PERCENT)	TOT. ERROR (PERCENT)
8.2	9.757E+00	9.2	7.690E+00	1.9	4.3
10.1	1.247E+01	11.4	9.837E+00	2.0	4.0
12.6	1.267E+01	14.2	1.002E+01	1.6	3.6
15.1	1.196E+01	17.0	9.485E+00	1.4	3.4
20.1	7.534E+00	22.6	6.011E+00	1.4	3.3
25.1	3.739E+00	28.2	3.008E+00	3.0	4.3
30.1	2.621E+00	33.8	2.129E+00	3.1	4.3
35.1	2.452E+00	39.3	2.015E+00	4.3	5.2
40.2	2.380E+00	44.9	1.981E+00	2.9	4.1
45.1	1.918E+00	50.3	1.620E+00	3.7	4.7
50.1	1.255E+00	55.7	1.077E+00	5.1	5.9
55.9	1.054E+00	62.0	9.225E-01	5.2	6.0
61.9	9.945E-01	68.4	8.901E-01	5.6	6.3
68.0	8.253E-01	74.8	7.567E-01	6.0	6.6
75.0	5.983E-01	82.1	5.648E-01	6.6	7.2
82.0	3.384E-01	89.3	3.293E-01	16.3	16.6
89.9	2.914E-01	97.2	2.937E-01	8.1	8.6
98.0	3.138E-01	105.3	3.281E-01	10.5	10.9
108.0	2.155E-01	115.0	2.355E-01	5.7	6.4
118.0	1.381E-01	124.5	1.574E-01	7.2	7.8
127.8	1.054E-01	133.6	1.248E-01	7.8	8.4
137.8	8.663E-02	142.7	1.061E-01	8.1	8.8
147.8	6.814E-02	151.7	8.586E-02	8.0	8.7
158.0	9.310E-02	160.7	1.199E-01	5.3	6.1

160(P,D)150 EP = 45.34 MEV EX = (9.49 - 9.66) MEV

LAB ANGLE (DEG)	LAB CROSS SECTION (MB/SR)	C.M. ANGLE (DEG)	C.M. CROSS SECTION (MB/SR)	STAT. ERROR (PERCENT)	TOT. ERROR (PERCENT)
8.2	5.741E-01	9.3	4.443E-01	10.5	15.6
10.1	7.075E-01	11.5	5.482E-01	9.9	12.2
12.6	7.413E-01	14.3	5.756E-01	7.3	9.1
15.1	6.271E-01	17.2	4.883E-01	6.9	8.8
20.1	4.619E-01	22.8	3.621E-01	6.1	7.4
25.1	3.077E-01	28.6	2.434E-01	11.1	12.0
30.1	1.784E-01	34.1	1.426E-01	14.0	16.5
35.1	2.954E-01	39.7	2.390E-01	13.0	13.9
40.2	2.191E-01	45.3	1.798E-01	10.1	11.0
45.1	1.956E-01	50.7	1.630E-01	11.8	12.5
50.1	1.175E-01	56.2	9.962E-02	17.1	17.8
55.9	1.200E-01	62.5	1.039E-01	15.4	15.7
61.9	1.156E-01	68.9	1.026E-01	16.2	16.5
68.0	9.203E-02	75.4	8.383E-02	19.1	20.0
75.0	7.039E-02	82.7	6.618E-02	20.8	22.3
82.0	4.740E-02	89.9	4.600E-02	38.0	38.1
89.9	3.948E-02	97.8	3.985E-02	23.8	25.1
98.0	5.062E-02	105.9	5.315E-02	25.8	26.0
108.0	2.694E-02	115.6	2.968E-02	18.3	20.4
118.0	3.039E-02	125.0	3.505E-02	16.4	17.6

168(P,D)150 EP = 45.34 MEV EX = 10.460 MEV

LAB ANGLE (DEG)	LAB CROSS SECTION (MB/SR)	C.M. ANGLE (DEG)	C.M. CROSS SECTION (MB/SR)	STAT. ERROR (PERCENT)	TOT. ERROR (PERCENT)
8.2	5.485E-01	9.4	4.221E-01	10.8	16.2
10.1	5.879E-01	11.5	4.531E-01	10.7	13.0
12.6	7.758E-01	14.4	5.993E-01	7.3	9.4
15.1	7.033E-01	17.2	5.448E-01	6.5	8.4
20.1	5.560E-01	22.9	4.337E-01	5.5	6.6
25.1	4.214E-01	28.5	3.316E-01	9.3	10.1
30.1	3.166E-01	34.2	2.518E-01	9.9	11.4
35.1	2.596E-01	39.8	2.091E-01	14.0	14.9
40.2	2.768E-01	45.4	2.263E-01	9.2	10.5
45.1	1.855E-01	50.8	1.540E-01	12.8	14.0
50.1	1.515E-01	56.3	1.280E-01	15.4	16.5
55.9	1.428E-01	62.6	1.234E-01	15.5	16.8
61.9	8.516E-02	69.1	7.539E-02	18.9	19.1

APPENDIX B

TABULATION OF $^{15}N(p,p)^{15}N$ AND $^{15}N(p,d)^{14}N$ DIFFERENTIAL CROSS SECTIONS

The following pages contain listings of the laboratory and center-of-mass differential cross sections with the corresponding statistical and total errors for the elastic scattering of protons from ^{15}N and for the levels of ^{14}N strongly excited in the $^{15}N(p,d)^{14}N$ reaction for 39.84 MeV protons. A discussion of the estimated errors is found in Chapter III (Section III.E.). The values of the cross sections are to be read as

$$1.492E+03 \equiv 1.492 \times 10^{3}.$$

15N(P,P)15N EP = 39.84 MEV EX = 0.000 MEV

LAB ANGLE (DEG)	LAB CROSS SECTION (MB/SR)	C.M. ANGLE (DEG)	C.M. CROSS SECTION (MB/SR)	STAT. ERROR (PERCENT)	TOT. ERROR (PERCENT)
9.9	1.492E+03	10.6	1.306E+03	0.3	3.4
12.0	1.363E+03	12.8	1.199E+03	0.2	3.1
15.9	1.069E+03	17.0	9.389E+02	0.2	2.9
19.9	7.612E+02	21.3	6.705E+02	0.2	2.9
24.9	4.108E+02	26.6	3.634E+02	0.2	2.8
29.9	1.820E+02	31.9	1.619E+02	0.3	2.8
34.9	7.145E+01	37.2	6.397E+01	0.6	2.8
39.9	2.921E+01	42.5	2.634E+01	0.8	2.8
44.9	1.833E+01	47.7	1.667E+01	0.9	2.9
49.8	1.853E+01	52.9	1.699E+01	0.8	2.8
54.7	1.713E+01	58.0	1.586E+01	1.1	2.9
59.8	1.372E+01	63.3	1.282E+01	1.1	2.9
64.8	9.636E+00	68.4	9.107E+00	1.2	3.0
69.8	6.028E+00	73.6	5.761E+00	1.3	3.0
74.8	3.558E+00	78.7	3.439E+00	1.8	3.3
79.8	1.934E+00	83.7	1.892E+00	2.5	3.8
84.8	1.398E+00	88.8	1.384E+00	2.7	4.2
89.7	1.059E+00	93.7	1.061E+00	3.1	4.6
97.3	9.064E-01	101.3	9.251E-01	3.0	4.3
104.7	6.014E-01	108.6	6.248E-01	3.5	5.0
112.2	3.277E-01	115.9	3.465E-01	5.2	6.1
119.6	1.671E-01	123.1	1.796E-01	6.0	6.9
127.1	9.039E-02	130.3	9.865E-02	9.4	11.2
134.6	9.057E-02	137.4	1.002E-01	10.2	14.4
142.1	2.260E-01	144.5	2.533E-01	8.0	9.1

15N(P,D)14N EP = 39.84 MEV EX = 0.000 MEV

LAB ANGLE (DEG)	LAB CROSS SECTION (MB/SR)	C.M. ANGLE (DEG)	C.M. CROSS SECTION (MB/SR)	STAT. ERROR (PERCENT)	TOT. ERROR (PERCENT)
9.9	1.382E+01	11.0	1.116E+01	3.1	4.5
12.0	1.265E+01	13.4	1.024E+01	2.2	3.8
15.9	8.556E+00	17.7	6.947E+00	2.1	3.6
19.9	4.857E+00	22.1	3.962E+00	2.6	3.9
24.9	2.118E+00	27.7	1.740E+00	3.2	4.2
29.9	2.141E+00	33.2	1.775E+00	2.9	4.0
34.9	2.052E+00	38.7	1.719E+00	3.2	4.2
39.9	1.592E+00	44.1	1.349E+00	3.6	4.5
44.9	1.019E+00	49.5	8.747E-01	3.8	4.7
49.8	7.651E-01	54.8	6.658E-01	4.1	4.9
54.7	6.766E-01	60.1	5.977E-01	5.5	6.1
59.8	6.857E-01	65.5	6.159E-01	4.9	5.6
64.8	5.571E-01	70.7	5.091E-01	4.9	5.6
69.8	4.454E-01	76.0	4.144E-01	4.5	5.2
74.8	3.166E-01	81.1	3.002E-01	5.9	6.5
79.8	2.125E-01	86.3	2.054E-01	7.0	7.5
84.8	1.340E-01	91.3	1.322E-01	8.0	8.5
89.7	9.720E-02	96.3	9.774E-02	9.4	9.8
97.3	9.743E-02	103.8	1.010E-01	8.6	9.0
104.7	5.824E-02	111.0	6.218E-02	10.3	10.6
112.2	5.642E-02	118.3	6.201E-02	12.1	12.4
119.6	3.154E-02	125.3	3.563E-02	13.2	13.5
127.1	3.033E-02	132.3	3.515E-02	14.0	14.3
134.6	2.330E-02	139.3	2.765E-02	15.1	15.3
142.1	2.932E-02	146.1	3.552E-02	20.4	20.6

15N(P,D)14N EP = 39.84 MEV EX = 2.311 MEV

LAB ANGLE (DEG)	LAB CROSS SECTION (MB/SR)	C.M. ANGLE (DEG)	C.M. CROSS SECTION (MB/SR)	STAT. ERROR (PERCENT)	TOT. ERROR (PERCENT)
9.9	3.788E+00	11.1	3.034E+00	5.9	6.7
12.0	4.274E+00	13.4	3.428E+00	3.8	5.0
15.9	3.272E+00	17.8	2.634E+00	3.4	4.5
19.9	2.021E+00	22.2	1.635E+00	4.1	5.0
24.9	9.205E-01	27.8	7.504E-01	4.9	5.7
29.9	6.203E-01	33.3	5.103E-01	5.5	6.1
34.9	7.128E-01	38.8	5.927E-01	5.5	6.1
39.9	5.648E-01	44.3	4.753E-01	6.0	6.6
44.9	4.068E-01	49.7	3.470E-01	6.1	6.7
49.8	3.104E-01	55.0	2.686E-01	6.4	7.0
54.7	2.255E-01	60.3	1.982E-01	9.5	9.9
59.8	2.013E-01	65.7	1.800E-01	9.1	9.5
64.8	1.502E-01	71.0	1.368E-01	9.4	9.8
69.8	1.397E-01	76.2	1.296E-01	8.1	8.5
74.8	7.612E-02	81.4	7.204E-02	12.2	12.5
79.8	5.652E-02	86.5	5.458E-02	13.6	13.9
84.8	5.102E-02	91.6	5.029E-02	13.9	14.1
89.7	3.298E-02	96.5	3.318E-02	16.2	16.4
97.3	1.876E-02	104.1	1.949E-02	19.6	19.8
104.7	1.594E-02	111.3	1.707E-02	19.6	19.8
112.2	6.640E-03	118.5	7.330E-03	35.4	35.5
119.6	7.190E-03	125.5	8.170E-03	27.7	27.9
127.1	5.950E-03	132.5	6.940E-03	31.6	31.7
134.6	1.165E-02	139.5	1.393E-02	21.3	21.5
142.1	8.550E-03	146.3	1.045E-02	37.8	37.9

15N(P,D)14N EP = 39.84 MEV EX = 3.945 MEV

LAB ANGLE (DEG)	LAB CROSS SECTION (MB/SR)	C.M. ANGLE (DEG)	C.M. CROSS SECTION (MB/SR)	STAT. ERROR (PERCENT)	TOT. ERROR (PERCENT)
9.9	4.228E+00	11.1	3.364E+00	5.6	6.5
12.0	4.050E+00	13.5	3.227E+00	4.0	5.0
15.9	3.720E+00	17.8	2.976E+00	3.2	4.3
19.9	2.292E+00	22.3	1.842E+00	3.8	4.8
24.9	9.096E-01	27.9	7.369E-01	4.9	5.7
29.9	6.622E-01	33.4	5.416E-01	5.3	6.0
34.9	6.772E-01	38.9	5.599E-01	5.6	6.2
39.9	6.251E-01	44.4	5.234E-01	5.7	6.3
44.9	5.066E-01	49.9	4.301E-01	5.5	6.1
49.8	4.282E-01	55.2	3.689E-01	5.5	6.1
54.7	3.219E-01	60.5	2.819E-01	8.1	8.6
59.8	2.733E-01	65.9	2.436E-01	7.8	8.3
64.8	2.167E-01	71.2	1.968E-01	7.9	8.3
69.8	1.859E-01	76.4	1.722E-01	7.1	7.5
74.8	1.677E-01	81.6	1.585E-01	8.1	8.5
79.8	1.047E-01	86.7	1.010E-01	10.1	10.4
84.8	7.696E-02	91.8	7.585E-02	10.7	11.0
89.7	6.162E-02	96.8	6.202E-02	12.0	12.3
97.3	4.474E-02	104.3	4.654E-02	12.7	13.0
104.7	3.310E-02	111.5	3.554E-02	13.6	13.9
112.2	3.236E-02	118.7	3.584E-02	16.0	16.2
119.6	3.044E-02	125.7	3.472E-02	13.5	13.7
127.1	1.427E-02	132.7	1.674E-02	20.4	20.6
134.6	1.642E-02	139.6	1.975E-02	18.0	18.2
142.1	1.344E-02	146.4	1.653E-02	30.2	30.3

15N(P,D)14N EP = 39.84 MEV EX = 7.030 MEV

LAB ANGLE (DEG)	LAB CROSS SECTION (MB/SR)	C.M. ANGLE (DEG)	C.M. CROSS SECTION (MB/SR)	STAT. ERROR (PERCENT)	TOT. ERROR (PERCENT)
9.9	5.146E+00	11.2	4.035E+00	5.1	6.1
12.0	6.009E+00	13.6	4.720E+00	3.3	4.5
15.9	4.889E+00	18.0	3.856E+00	2.8	4.0
19.9	3.480E+00	22.5	2.759E+00	3.1	4.2
24.9	1.736E+00	28.1	1.388E+00	3.6	4.5
29.9	1.199E+00	33.7	9.680E-01	3.9	4.8
34.9	1.201E+00	39.2	9.813E-01	4.2	5.0
39.9	1.288E+00	44.7	1.067E+00	4.0	4.8
44.9	1.049E+00	50.2	8.813E-01	3.8	4.7
49.8	7.930E-01	55.6	6.769E-01	4.0	4.9
54.7	6.376E-01	60.9	5.537E-01	5.7	6.3
59.8	6.595E-01	66.3	5.837E-01	5.0	5.7
64.8	5.185E-01	71.6	4.681E-01	5.1	5.8
69.8	5.043E-01	76.9	4.648E-01	4.2	5.0
74.8	3.972E-01	82.1	3.740E-01	5.3	5.9
79.8	2.805E-01	87.2	2.701E-01	6.2	6.7
84.8	2.136E-01	92.3	2.104E-01	6.5	7.0
89.7	1.441E-01	97.2	1.451E-01	7.9	8.3
97.3	1.321E-01	104.8	1.378E-01	7.5	8.0
104.7	1.275E-01	112.0	1.376E-01	7.0	7.5
112.2	8.960E-02	119.2	1.000E-01	9.8	10.2
119.6	8.522E-02	126.1	9.817E-02	8.2	8.6
127.1	6.957E-02	133.1	8.257E-02	9.6	10.0
134.6	6.091E-02	140.0	7.428E-02	9.4	9.8
142.1	5.253E-02	146.7	6.561E-02	15.2	15.5

15N(P,D)14N EP = 39.84 MEV EX = 9.170 MEV

LAB ANGLE (DEG)	LAB CROSS SECTION (MB/SR)	C.M. ANGLE (DEG)	C.M. CROSS SECTION (MB/SR)	STAT. ERROR (PERCENT)	TOT. ERROR (PERCENT)
9.9	2.030E+00	11.3	1.573E+00	8.1	8.8
12.0	2.096E+00	13.6	1.627E+00	5.5	6.4
15.9	2.013E+00	18.1	1.569E+00	4.4	5.3
19.9	1.516E+00	22.6	1.188E+00	4.7	5.5
24.9	8.005E-01	28.2	6.329E-01	5.3	6.0
29.9	5.949E-01	33.9	4.753E-01	5.6	6.3
34.9	5.535E-01	39.4	4.476E-01	6.2	6.8
39.9	5.909E-01	45.0	4.847E-01	6.0	6.6
44.9	5.290E-01	50.5	4.406E-01	5.4	6.0
49.8	3.560E-01	55.9	3.015E-01	6.3	6.8
54.7	2.337E-01	61.2	2.016E-01	9.6	10.0
59.8	2.586E-01	66.7	2.275E-01	8.0	8.4
64.8	2.327E-01	72.0	2.090E-01	7.6	8.1
69.8	2.095E-01	77.2	1.924E-01	6.6	7.1
74.8	1.853E-01	82.5	1.741E-01	8.0	8.4
79.8	1.476E-01	87.6	1.419E-01	8.6	9.0
84.8	1.124E-01	92.7	1.107E-01	9.1	9.5
89.7	1.085E-01	97.6	1.094E-01	9.0	9.4
97.3	9.526E-02	105.2	9.968E-02	8.9	9.3
104.7	7.172E-02	112.4	7.778E-02	9.5	9.8
112.2	6.305E-02	119.5	7.084E-02	11.6	11.9
119.6	5.257E-02	126.5	6.106E-02	10.7	11.0
127.1	5.530E-02	133.4	6.628E-02	10.7	11.0
134.6	4.449E-02	140.2	5.487E-02	11.0	11.4
142.1	1.344E-02	147.0	1.700E-02	30.2	30.3

15N(P,D)14N EP = 39.84 MEV EX = 10.430 MEV

LAB ANGLE (DEG)	LAB CROSS SECTION (MB/SR)	C.M. ANGLE (DEG)	C.M. CROSS SECTION (MB/SR)	STAT. ERROR (PERCENT)	TOT. ERROR (PERCENT)
9.9	1.422E+00	11.3	1.093E+00	9.7	10.3
12.0	1.425E+00	13.7	1.097E+00	6.9	7.6
15.9	8.889E-01	18.1	6.875E-01	7.9	8.4
19.9	1.119E+00	22.7	8.707E-01	5.6	6.3
24.9	6.713E-01	28.3	5.273E-01	5.9	6.5
29.9	4.766E-01	34.0	3.781E-01	6.6	7.2
34.9	4.906E-01	39.6	3.941E-01	6.7	7.3
39.9	3.920E-01	45.2	3.195E-01	8.0	8.4
44.9	3.725E-01	50.7	3.085E-01	6.6	7.1
49.8	2.825E-01	56.1	2.380E-01	7.0	7.5
54.7	2.870E-01	61.4	2.464E-01	8.9	9.3
59.8	2.095E-01	66.9	1.836E-01	9.0	9.4
64.8	2.154E-01	72.2	1.929E-01	8.1	8.6
69.8	2.113E-01	77.5	1.936E-01	6.7	7.2
74.8	1.622E-01	82.7	1.520E-01	8.5	8.9
79.8	1.465E-01	87.9	1.407E-01	8.7	9.1
84.8	1.133E-01	93.0	1.115E-01	9.3	9.6
89.7	8.244E-02	97.9	8.318E-02	10.5	10.8
97.3	6.639E-02	105.4	6.961E-02	11.3	11.6
104.7	6.130E-02	112.6	6.669E-02	10.3	10.6
112.2	7.218E-02	119.8	8.144E-02	11.0	11.3
119.6	6.032E-02	126.7	7.044E-02	10.2	10.5
127.1	3.568E-02	133.6	4.305E-02	13.7	14.0
134.6	4.396E-02	140.4	5.464E-02	11.2	11.6

15N(P,D)14N EP = 39.84 MEV EX = 13.720 MEV

LAB ANGLE (DEG)	LAB CROSS SECTION (MB/SR)	C.M. ANGLE (DEG)	C.M. CROSS SECTION (MB/SR)	STAT. ERROR (PERCENT)	TOT. ERROR (PERCENT)
9.9	1.513E+00	11.5	1.134E+00	10.4	11.0
12.0	1.835E+00	13.9	1.378E+00	6.2	7.0
15.9	1.569E+00	18.4	1.184E+00	5.1	5.9
19.9	1.450E+00	23.0	1.101E+00	5.0	5.8
24.9	9.925E-01	28.7	7.610E-01	5.0	5.7
29.9	7.149E-01	34.4	5.547E-01	5.3	6.0
34.9	6.080E-01	40.1	4.783E-01	6.1	6.6
39.9	5.789E-01	45.7	4.627E-01	6.6	7.1
44.9	5.603E-01	51.3	4.557E-01	5.7	6.3
49.8	3.864E-01	56.7	3.203E-01	6.1	6.6
54.7	2.317E-01	62.1	1.960E-01	9.6	9.9
59.8	2.602E-01	67.6	2.252E-01	8.5	8.9
64.8	2.672E-01	73.0	2.368E-01	7.6	8.1
69.8	2.494E-01	78.3	2.266E-01	6.3	6.9
74.8	2.008E-01	83.5	1.872E-01	7.8	8.3
79.8	2.020E-01	88.7	1.934E-01	7.4	7.9
84.8	1.600E-01	93.8	1.574E-01	7.8	8.2
89.7	1.371E-01	98.8	1.386E-01	8.2	8.6
97.3	1.277E-01	106.3	1.347E-01	8.0	8.5
104.7	9.809E-02	113.5	1.078E-01	8.4	8.8
112.2	8.048E-02	120.6	9.209E-02	10.6	10.9
119.6	9.131E-02	127.5	1.085E-01	8.0	8.5
127.1	1.023E-01	134.3	1.261E-01	7.8	8.2
134.6	9.957E-02	141.0	1.268E-01	7.4	7.9
142.1	7.086E-02	147.6	9.292E-02	13.8	14.1

REFERENCES

At 67 R.A. Atneosen, private communication.

Au 63 N. Austern, in Fast Neutron Physics, Vol. II, ed. by J.B. Marion and J.L. Fowler (Interscience Publishers, New York, 1963).

Au 64 N. Austern, R.M. Drisko, E.C. Halbert, and G.R. Satchler, Phys. Rev. 133, B3 (1964).

Ba 64 D. Bachelier, M. Bernas, I. Brissand, C. Detraz, N.K. Ganguhy, and P. Radvangi, Compt. Rend. du Congr. Intern. de Physique Nuclèaire, II, 429 (1964).

Ba 65 R.C. Barrett, A.D. Hill, and P.E. Hodgson, Nucl. Phys. 62, 133 (1965).

Ba 62 R.H. Bassel, R.M. Drisko, and G.R. Satchler, Oak Ridge National Laboratory Report ORNL-3240 (unpublished, 1962).

Ba 66 R.H. Bassel, R.M. Drisko, and G.R. Satchler, "Oak Ridge National Laboratory Memorandum to the Users of the Code JULIE" (unpublished, 1966).

Be 68 G.F. Bertsch, private communication.

Be 68a W. Benenson, R. DeForest, W.P. Johnson, and E. Kashy (to be published in Nucl. Instr. Meth.).

Bl 66 H.G. Blosser and A.I. Galonsky, IEEE Trans. on Nuclear Science, NS-B, No. 4, 466 (1966).

Br 66a G.E. Brown and A.M. Green, Nucl. Phys. 75, 401 (1966).

Br 66b G.E. Brown and A.M. Green, Nucl. Phys. 85, 87 (1966).

Br 67 G.E. Brown and A.P. Shukla, Princeton University Report No. PUC-937-268 (unpublished, 1967).

Bu 51 S.T. Butler, Proc. Roy. Soc. (London), A208, 559 (1951).

Ca 67 J.M. Cameron, University of California at Los Angeles Technical Report No. P-80 (unpublished, 1967).

Ca 68 J.M. Cameron, J.R. Richardson, W.T.H. van Oers, and J.W. Verba, Phys. Rev. 167, 908 (1968).

Ch 67 N.W. Chant, P.S. Fisher, and D.K. Scott, Nucl. Phys. A99, 669 (1967).

Co 35 E.U. Condon and G.H. Shortley, The Theory of Atomic Spectra (Cambridge University Press, 1935).

Co 65 S. Cohen and D. Kurath, Nucl. Phys. 73, 1 (1965).

Co 66 A.A. Cowley, G. Heymann, R.L. Keizer, and M.J. Scott, Nucl. Phys. 86, 363 (1966).

Co 67 S. Cohen and D. Kurath, Nucl. Phys. A101, 1 (1967).

Du 66 B. Duelli, F. Hintenberger, G. Mairle, U. Schmidt-Rohr, P. Turek, and G. Wagner, Phys. Letters 23, 485 (1966).

Du 68 Y. Dupont and M. Chabre, Phys. Letters 26B, 362 (1968).

El 68 H.B. Eldridge, S.N. Bunker, J.M. Cameron, J.R. Richardson, and W.T.H. van Oers, Phys. Rev. 167, 915 (1968).

En 65 T. Engeland, Nucl. Phys. 72, 68 (1965).

Fa 67 J.A. Fannon, E.J. Burge, D.A. Smith, and N.K. Ganguly, Nucl. Phys. A97, 263 (1967).

Fe 37 E. Feenberg and E. Wigner, Phys. Rev. 51, 95 (1937).

Fi 67 W. Fitz, R. Jahr, and R. Santo, Nucl. Phys. A101, 449 (1967).

Fr 67 M.P. Fricke, E.E. Gross, B.J. Morton, and A. Zucker, Phys. Rev. 156, 1207 (1967).

Gl 65 See for example, C.M. Glashauser, Ph.D. Thesis, Princeton University (unpublished, 1965).

Ha 66 B.G. Harvey, J.R. Merriwether, and J. Mahoney, Phys. Rev. 146, 712 (1966).

Hi 67 J.C. Hiebert, E. Newnan, and R.H. Bassel, Phys. Rev. 154, 898 (1967).

Ho 66 P.E. Hodgson, Advn. Phys. 15, 329 (1966), quoted in Ref. Ch 67.

In 53 D.R. Inglis, Rev. Mod. Phys. 25, 390 (1953).

Jo 58 L.H. Johnston and D.A. Swenson, Phys. Rev. 111, 212 (1958).

Jo 63 H.P. Holly, Phys. Letters 5, 289 (1963).

Ka 61 E. Kashy, R.R. Perry, R.L. Steele, and J.R. Risser, Phys. Rev. 122, 884 (1961).

Ki 64 C.C. Kim, S.M. Bunch, D.W. Devins, and H.H. Forster, Nucl. Phys. 58, 32 (1964).

Kl 66 A.P. Klyucharev and Yu. I. Titov, Izv. Akad. Nauk. SSSR, Ser. Fiz., 30, 224 (1966).

Ko 67 R.L. Kozub, L.A. Kull, and E. Kashy, Nucl. Phys. A99, 540 (1967).

Ko 67a R.L. Kozub, Ph.D. Thesis, Michigan State University (unpublished, 1967).

Ku 52 D. Kurath, Phys. Rev. 88, 804 (1952).

Ku 56 D. Kurath, Phys. Rev. 101, 216 (1956).

Ku 57 D. Kurath, Phys. Rev. 106, 975 (1957).

Ku 67 L.A. Kull, Ph.D. Thesis, Michigan State University (unpublished, 1967).

La 62 T. Lauritzen and F. Ajzenberg-Selove, Nuclear Data Sheets, compiled by K. Way et al., Printing and Publishing Office, National Academy of Sciences, National Research Council, Washington 25, D.C. (1962).

La 67 M. Lambert and M. Durand, Phys. Letters 24B, 287 (1967).

Le 63 J.C. Legg, Phys. Rev. 129, 272 (1963).

Le 64 L.L. Lee, Jr., J.P. Schiffer, B. Zeidman, G.R. Satchler, R.M. Drisko, and R.H. Bassel, Phys. Rev. 136, B971 (1964).

Le 67 J.K.P. Lee, S.K. Mark, P.M. Portner, and R.B. Moore, Nucl. Phys. A106, 357 (1967).

Lo 66 J.S. Lopes, O. Häusser, H.J. Rose, A.R. Polletti, and M.F. Thomas, Nucl. Phys. 76, 223 (1966).

Ma 50 M. Mayer, Phys. Rev. 78, 16 (1950).

Ma 67 G.H. Mackenzie, E. Kashy, M.M. Gordon, and H.G. Blosser, IEEE Trans. on Nuclear Science, NS-14, No. 3, 450 (1967).

Ma 67 a N.F. Mangelson, University of California Lawrence Radiation Laboratory Report No. 17732 (unpublished, 1967).

Mi 63 G.L. Miller and V. Radeka, Proc. NAS Conf. on Instrument Techniques in Nuclear Pulse Analysis, Monterey, California, 1963.

Mo 56 H. Morinaga, Phys. Rev. 101, 254 (1956).

Ne 67 E. Newman, L.C. Becker, B.M. Preedom, and J.C. Hiebert, Nucl. Phys. A100, 225 (1967).

Ng 66 Dai-Ca Nguyen, J. Phys. Soc. Japan 21, 2462 (1966).

Pe 65 R.H. Pehl, E. Rivet, J. Cerny, and B.G. Harvey, Phys. Rev. 137, B114 (1965).

Ro 48 L. Rosenfeld, Nuclear Forces (North-Holland, Amsterdam, 1948).

Ro 65 H.J. Rose and J.S. Lopes, Phys. Letters 18, 130 (1965).

Sa 64 G.R. Satchler, Nucl. Phys. 55, 1 (1964).

Sh 67 G.G. Shute and R.E. Brown, University of Minnesota Linear Accelerator Laboratory Annual Progress Report 55 (1967).

Si 59 E.A. Silverstein, Nucl. Instr. Meth. 4, 53 (1959).

Si 67 R.H. Siemssen, Bull. Am. Phys. Soc. 12, 479 (1967).

Sn 67 J.L. Snelgrove and E. Kashy, Nucl. Instr. Meth. 52, 153 (1967).

Te 64 J. Testoni, S. Mayo, and P.E. Hodgson, Nucl. Phys. 50, 479 (1964).

To 61 W. Tobocman, Theory of Direct Nuclear Reactions (Oxford University Press, 1961).

Va 68 W.T.H. van Oers and J.M. Cameron, Bull. Am. Phys. Soc. 13, 883 (1968).

Vi 66 J.L. Vidal, R. Bouchet, C. Fayard, L. Feuvrais, M. Gaillard, P. Gaillard, M. Gouanere, M. Gusakow, G. H. Lamont, and J.R. Pizzi, J. Phys. (Paris), Coloq., No. 1, 128 (1966).

Wa 60 E.K. Warburton and W.T. Pinkston, Phys. Rev. 118, 733 (1960).

Wa 65 E.K. Warburton, J.W. Olness, and D.E. Alburger, Phys. Rev. 140, B1202 (1965).

Wa 65a K.K. Warburton, P.D. Parker, and P.F. Donovan, Phys. Letters 19, 397 (1965).

Wo 68 S.S.M. Wong (to be published).

Za 67 C.D. Zafiratos, J.S. Lilley, and F.W. Slee, Phys. Rev. 154, 887 (1967).